MILLIMETRE AND SUBMILLIMETRE CONTINUUM IMAGING STUDIES OF NEARBY ACTIVE GALAXIES

BY

LEROTHODI LEONARD LEEUW

Thesis

for

DOCTOR OF PHILOSOPHY

Centre for Astrophysics

UNIVERSITY OF CENTRAL LANCASHIRE

JUNE 2002

Abstract

The thesis presents millimetre (mm) and submm continuum imaging observations of the four, nearby active galaxies Cygnus A, NGC 4374, Centaurus A and M 82. These were undertaken using the Submillimetre Common-User Bolometer Array (SCUBA) on the James Clerk Maxwell Telescope in Hawaii. The study focused on the properties of the cool to cold dust ($\sim$ 80 to 10 K) and its associations with star formation and nuclear activity in the galaxies.

The observations of Cygnus A constrained the galaxy's cold dust temperature between 37 and 85 K, corresponding to dust masses between $1.0 \times 10^8 M_\odot$ and $1.4 \times 10^6 M_\odot$ respectively. Based on the dust spatial and mass limits, it is possible the heating of the cold dust in Cygnus A is dominated by high-energy nuclear activity or star formation. Detailed photometric observations of the core and two major hotspots (A and D) in Cygnus A showed that their mm to submm spectral indices extend smoothly to about 450μm (677 GHz), with no evidence of spectral steepening. The results allow tight determinations for model parameters of synchrotron electron lifetimes in these components.

In pilot survey observations of the elliptical galaxy NGC 4374, a mass upper-limit of $\sim 2 \times 10^7 M_\odot$ (i.e. comparable to the dust contents of luminous spiral galaxies) was placed on the diffuse dust that, if it exists, would affect colour and metallicity studies

of elliptical galaxies. Following the pilot observations, a strategy was devised to select a good sample of ellipticals in which to search for this low-level, very cold dust.

For the first time ever, the observations of Centaurus A delineated the galaxy's submm unresolved core, an inner-jet interacting with gas in the dust lane, and extended emission from multi-temperature cold dust at $\sim$ 40, 30 and 12 K. Also for the first time ever, a submm high surface brightness ringed, spiral structure of radii $\sim 90''$, that coincides with the regions of intense star formation and mid-infrared continuum, was revealed in the optical dust-lane, confirming predictions by a geometric warped disc model consisting of tilted rings. From the spatial associations in the galaxy, star formation seems to dominate at lease 50% of the heating of the cold dust, while the rest appears to be heated by diluted stellar radiation.

In M 82, the 850 μm continuum has been detected out to 1.5 kpc, at least 10% farther in radius than previous detections in this starburst galaxy. The overall submm morphology and nuclear spectral index distribution have a general north-south asymmetry similar to that of H_α and X-ray winds, supporting the association of the extended continuum with outflows of dust grains from the nucleus into the halo. The work of M 82 raises many interesting points about the origin and structure of the submm emission, however the results are displayed here still under investigation and therefore are rather *preliminary.*

In short, the submm continuum observations of Cygnus A, NGC 4374, Centaurus A and M 82 are presented in this thesis that constrain the physical properties of cold dust in these active galaxies and elucidate the associations of the dust with star formation, nuclear activity and stellar components in these galaxies in particular, and other similar galaxies in general.

Contents

List of Tables

List of Figures

Acknowledgements

The University of Central Lancashire (UCLan) is acknowledged for a fruitful Ph.D. program that was supported by a full-time university research studentship. The Joint Astronomy Centre (JAC) in Hawaii is also acknowledged for their hospitality and "aloha" during the acquisition and analysis of data for this Ph.D. research. Profs. E. Ian Robson (Director of the JAC), Gordon E. Bromage (Head of the Centre for Astrophysics, UCLan) and Mike C. Holmes (Head of Department of Physics, Astronomy and Mathematics, UCLan) arranged and supported the complicated logistics of a Ph.D. undertaken both in England and Hawaii by a South African national.

Prof. Robson is acknowledged as director of studies and for providing his Director's Discretionary Time that ensured extensive telescope-observing experience was gained and new data obtained for this thesis and invariably many other unrelated programs. His enthusiastic encouragement, whether given in person or 'beamed' by email or fax across one ocean or two, led to new results that were presented in several refereed scientific journals and at international conferences. His guidance allowed for the development of an independent research initiative that should yield further scientific advancements in the future. For the publications of work on NGC 4374 and Centaurus A, fruitful collaborations are acknowledged with the leading co-authors Drs. A. E. Sansom and

H.E. Matthews, respectively, as well as many others as noted in the relevant papers. The referees and scientific editors of the relevant publications are acknowledged for invaluable comments that improved the final quality of the published papers.

Drs. T. Jenness, R. Tilanus, M. J. Currie, D. S. Berry advised in the full exploitation of SURF and other Starlink Project software packages used in data analysis. Drs. G. Sandell, R. Ivison, W. Holland and E. Archibald gave needed guidance in the acquisition and exploitation of SCUBA data. Very useful scientific discussions were had with, among others, Drs. T. Hawarden, D. Hughes, A. Quillen, A. Eckart and J. Stevens. The JCMT Telescope System Specialists too assisted during many long nights up Mauna Kea.

Work at the JAC was very enjoyable, made especially so by the friendships forged with the support staff there and many Canadian co-op students who did their "work-studies" at the centre. Special mention goes to Erik Starman for good times away from work and to Aunties Donna, Marge and Anna for their "aloha". Also in Hilo, Hawaii, but outside the JAC, special mention goes to the crew at Cronies Bar and Grill, noting Shea, Layne and Ken for many eventful nights, and also friends at the Naniloa Paradise SPA for cool and relaxing hours.

Work at UCLan was also quite exciting. Special mention here goes to Bill, Cormac, Gabriel, Greg and Giulio for most memorable times at work and around Preston. Dr. A. Stirling provided lodging at a big discount when University funding ran out in the final stages of the Ph.D. The UCLan International Student Office (Maria and Diana) is thanked for assisting in arranging visa extensions and emergency funding during those crucial final months of the Ph.D. For numerous supporting letters and general assistance during the entire Ph.D., Mrs. Fiona Mair and her colleagues in the UCLan Academic Records are also acknowledged.

Due to illness that began midway through the program, the "writing-up" of work presented here took longer than the expected completion time for a Ph.D. at UCLan. Physicians in Hawaii, in particular Drs. Arakawa and Adee, and at the UCLan Health Services are acknowledged for trying in vain to treat this still undiagnosed but now improved ill-condition, that to much frustration causes pain when typing, thus hampering progress on work at the computer. Many thanks goes to Lynn G. and Mona G. for helping with typing some 40 pages (between them) of the thesis in the final "writing-up" stages.

The Ph.D. examiners are acknowledged for recommending pointed changes to the originally submitted manuscript, the incorporation of which have improved the quality of this thesis. Dr. T. V. Cawthorne is thanked for his role as second supervisor and for advice on many aspects of this Ph.D., in particular for his critical reading and patient discussion of the thesis leading to the incorporation of the examiners recommended changes.

Overall, the Ph.D. program was an enriching academic and memorable social experience. The Leeuw family are acknowledged for unwavering and visionary guidance on matters both in and outside school. Much gratitude goes to numerous, dear friends for their boundless love and encouragement. Once again UCLan and the JAC are thanked for providing the opportunity and support for this Ph.D.

Observations presented in this thesis extensively used the James Clerk Maxwell Telescope (JCMT), which is operated by the JAC on behalf of the United Kingdom Particle Physics and Astronomy Research Council, the Netherlands Organization for Scientific Research and the Canadian National Research Council. The data analysis was undertaken using the dedicated SCUBA data reduction software SURF, as well as KAPPA, GAIA, FIGARO and CONVERT software packages provided by the Starlink Project.

The Starlink Project is run by the Council for the Central Laboratory of the Research Councils on behalf of the Particle Physics and Astronomy Research Council of the United Kingdom. This research has made use of *Infrared Astronomy Satellite* (*IRAS*) data that were re-processed using HIRES and SCANPI routines at NASA/IPAC, which is operated by the Jet Propulsion Laboratory, Caltech, under contract to the National Aeronautics and Space Administration. Use was also made of data from ISOCAM, the infrared imager on the *Infrared Space Observatory* (*ISO*), which is a European Space Agency (ESA) project with instruments funded by ESA member states and with participation of ISAS and NASA. Dr. F. Mirabel is acknowledged for providing the reduced ISOCAM data. An optical waveband (395 and 540 nm) image courtesy of the Anglo-Australian Observatory was also used. This research has also made use of the NASA/IPAC Extragalactic Database (NED) which is operated by the Jet Propulsion Laboratory, California Institute of Technology, under contract with the National Aeronautics and Space Administration.

DEDICATION

To my late mother and father

to whom

I owe all my education and good life

Chapter 1

Introduction

1.1 The Revolution of Submm Astronomy with SCUBA

Until the mid-1990's, the only instruments available for the submillimetre (submm) waveband continuum astronomy were single-pixel, broadband photometers. With these, such as UKT14, which operated on the United Kingdom Infrared Telescope (UKIRT) and the James Clerk Maxwell Telescope (JCMT) from 1984 to 1988 and 1988 to 1996 respectively, mapping extended regions of the sky was very slow, and instrument sensitivity was detector-noise limited. The thesis project described here began in late 1997, during the final commissioning of the JCMT's new submillimetre continuum pixel-array, SCUBA (Holland et al., 1999).

SCUBA is the first large-scale submm array designed for submm astronomy. It is mounted on the world's largest submm telescope, which is well supported by scientific and technical staff, and has a dedicated suite of data reduction software making data analysis and hence publication of scientific results readily achievable. As recently reviewed by Robson (2001), SCUBA has opened up submm observational astronomy, one of the last

unexplored windows on the physical Universe. It has truly revolutionised at least two main areas of astrophysics: galaxy evolution in the early Universe (e.g. Smail et al., 1997; Barger et al., 1998; Hughes et al., 1998) and dust discs around main-sequence stars (Holland et al., 1998; Greaves et al., 1998), and dramatically extended large-scale survey programmes addressing star formation (e.g. Johnstone & Bally, 1999; Pierce-Price et al., 2000). In addition, it has made significant contributions to the study of galaxies in the nearby Universe, particularly in the investigation of the variability and nature of non-thermal radiation from compact extragalactic structures (e.g. Robson et al., 1998) and the properties and distribution of submm thermal re-radiation from cool dust in nearby galaxies (e.g. Alton et al., 1999; Israel et al., 1999; Leeuw et al., 2002), which is the focus of this thesis.

1.2 The Submm Galaxies Studied Here

The original thesis project was to investigate non-thermal and thermal emission from a small sample of nearby galaxies using SCUBA. In part, this was only partially successful due to observing and time constraints. Eventually, the thesis focuses on the cool to cold dust component of a smaller selection of galaxies, ie. Cygnus A, NGC 4374, Centaurus A and M 82, which all lie in the nearby Universe, within ≤ 200 Mpc of our galaxy.

The galaxies have active nuclei and other interesting properties, mostly discovered in wavelengths other than the submm. Cygnus A, NGC 4374 and Centaurus A have jets and lobes seen in the radio and X-ray wavelengths, while M 82 has starburst associated, large-scale outflows seen in emission-line and X-ray observations. The radio image of the jet and lobes in Cygnus A, courtesy of the National Radio Astronomy Observatory (NRAO), is shown in Figure 1.1, while the optical image of the dust lane in Centaurus A, courtesy

of the European Southern Observatory (ESO), seen obscuring the galactic stellar component, is shown in Figure 1.2. These galaxies were expected to emit submm thermal re-radiation from cool dust because they have dust lanes discovered in optical studies and generally emit copious far-infrared emission detected in *Infrared Astronomy Satellite* (*IRAS*) observations. They were also expected to emit some non-thermal submm radiation, most likely associated with their radio compact nuclei, but perhaps also their jets and lobes.

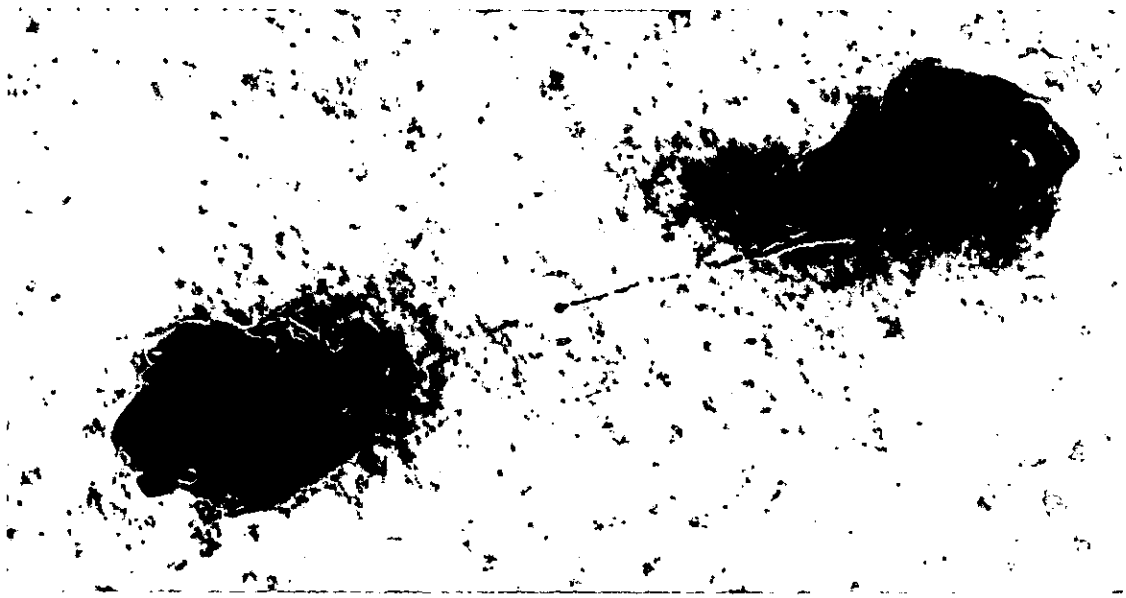

Figure 1.1: Cygnus A plumes, jet and hotspots as seen in the radio, courtesy of NRAO.

The goal with the current Cygnus A observations was to investigate suggestions that the origin of the *IRAS* excess emission in the galaxy was thermal radiation from cool dust (e.g. Salter et al., 1989). As the entire galaxy, including the radio lobes and the hotspots, fits on the instantaneous view of the SCUBA array, the hotspots' submm spectral energy distribution was also to be investigated. In NGC4374, which is an elliptical galaxy, the existence of lower level diffuse dust was explored following suggestions by Goudfrooij (1994) that *IRAS* fluxes did not account for all the dust mass estimated from optical

Figure 1.2: The dust lane in Centaurus A as seen in an optical image, courtesy of ESO.

extinction observations of this galaxy and other ellipticals.

The dusty nuclear regions of M 82 and Centaurus A were previously mapped in the submm regime with UKT14, respectively by Hughes et al. (1994) and Hawarden et al. (1993). The observations achieved understandably limited success, particularly in spatial extent, as this single-pixel predecessor of SCUBA, though excellent during its time, was relatively less sensitive and not efficient for mapping. The current imaging study was intended to extend the previous observations in spatial extent, sensitivity and in all the four wavelengths available with the SCUBA array. As these two galaxies are espe-

cially nearby, only about 3 Mpc away, they allow for high resolution imaging. Therefore, structure and physical properties of the emitting regions can be constrained.

Nearby galaxies were targeted for observation with the goal of exploiting the new submm imaging capabilities of SCUBA in making simultaneous, dual wavelength maps at moderate-to-high resolution. The dual wavelength observations, which can be obtained simultaneously at 850 and 450 μm or 750 and 350 μm, allow submm spectral index distribution maps to be computed, and the relatively high resolution allows structure of the emitting regions to be delineated. Therefore, the radiation mechanisms responsible for the emission structures could be distinguished and the physical characteristics of the mechanisms could be studied over extended spatial scales and in specific parts of the galaxies. For example, in the case of emission from dust re-radiation, the temperatures (or grain emissivity) and mass content of extended, discrete dust regions in the nearby galaxies could be determined. It is noted that galactic dust grains may be reasonably assumed to contain simply a fixed fraction, e.g. $\sim 50\%$, of the heavy metals in the interstellar medium (e.g. Edmunds & Eales, 1998; Edmunds, 2001), so studying the dust-mass content, especially at all temperatures, is an essential aspect of the investigation of galactic metallicity and the interstellar medium in general.

1.3 The Nature of Submm Continuum Emission

Millimetre and submm observations are essential for studies of thermal re-radiation from cool dust in astrophysical objects, as it is in the submm that the cold dust radiates strongest. Another thermal process that is potentially significant in the mm to submm regime is free-free or bremsstrahlung emission from ionised gas. This emission can be particularly important at the longer, mm wavelengths, especially in sources where the

bulk of the luminosity comes from regions of star formation (Kronberg et al., 1985). Non-thermal, synchrotron emission from extragalactic structures such as compact nuclei, jets and lobes, that are features of radio-loud active galaxies, also radiates in the mm to submm region. This is usually an extrapolation of the high frequency radio synchrotron spectrum which may be found to steepen in the submm. This steepening spectrum is a manifestation of ageing high energy synchrotron electrons, and submm observations can place crucial limits on the electron spectral energy distributions in this regime.

In this section, the thermal re-radiation from cool dust is presented first, as it is the dominant emission mechanism responsible for the submm continuum in the sources selected here. Following this, synchrotron and free-free mechanisms are presented in turn.

1.3.1 Thermal Re-radiation from Dust

Dust grains absorb ultraviolet through optical to infrared electromagnetic radiation. They are efficient absorbers at wavelengths less than or equal to their physical sizes but are transparent at longer wavelengths. The grains are heated to a temperature which is determined by the balance between the energy absorbed from the radiation field and their rate of radiation. In other words, heated by incident radiation, the grains attain thermal equilibrium and radiate effectively like greybodies. This radiation is given by the Planck function modified by the frequency dependent emissivity function of the grains and is written as $\epsilon(\nu) = \kappa(\nu)B(\nu)$, where $B(\nu)$ is the Planck function and $\kappa(\nu)$ is the emissivity of the grains (Longair, 1997).

To a good approximation, $\kappa(\nu) \propto \nu$ at wavelengths less than $100\,\mu$m and $\propto \nu^2$ at wavelengths longer than $100\,\mu$m (Hildebrand, 1983). The cool grains are heated to typically 30 to 100 K and radiate their peak emission at wavelengths of about 30 to $100\,\mu$m,

while the colder grains reach only 10 to 30 K and radiate their peak emission at 100 to 300 μm. Longward of the peak emission, the thermal spectrum is a good approximation of the Rayleigh-Jeans tail of the blackbody function. At these wavelengths, the dust is transparent. Therefore, the energy is radiated very efficiently, and the emission can be seen to great depths (Longair, 1997). This picture explains why galaxies selected for study here have not only dust lanes but also emit copious *IRAS*-detected, far-infrared emission. **The fact that the dust re-radiation is optically thin means that any resolved, detected dust emission could potentially reveal structure deep in the galaxy. Such structure, imaged extensively for the first time in the submm** (and in some cases for the first time in any waveband) **will be presented in this thesis.**

For a given dust temperature $T_{\rm dust}$, the flux density S_ν takes the form

$$S_\nu = \Omega \frac{2h\nu^3}{c^2} \frac{1}{\exp(\frac{h\nu}{kT_{\rm dust}}) - 1} [1 - \exp(-(\frac{\nu}{\nu_0})^\beta)], \qquad (1.1)$$

where Ω is the solid angle for the emitting region, ν_o the frequency at which the optical depth is unity and β the emissivity index of the grains. Extensive observations of molecular dust clouds have shown that β values range from 1 to 2. As an example, a thermal dust emission spectrum is shown in Figure 1.3, fit to the submm to infrared data of Arp 220. The figure illustrates that, as it turns out, Arp 220 is a remarkably good source to fit the thermal function given in equation 1.1. The fit indicates a temperature of 61 K and $\beta = 2$ with the optical depth being 1 at 180 μm and 0.26 at 350 μm(Emerson et al., 1984). As noted earlier, longward of the spectral turnover or peak, the flux density follows a Rayleigh-Jeans, power-law decline, $S_\nu \propto \nu^\alpha$, where $\alpha = \beta + 2$, while shortward of the peak, the flux follows the Wien, exponential fall.

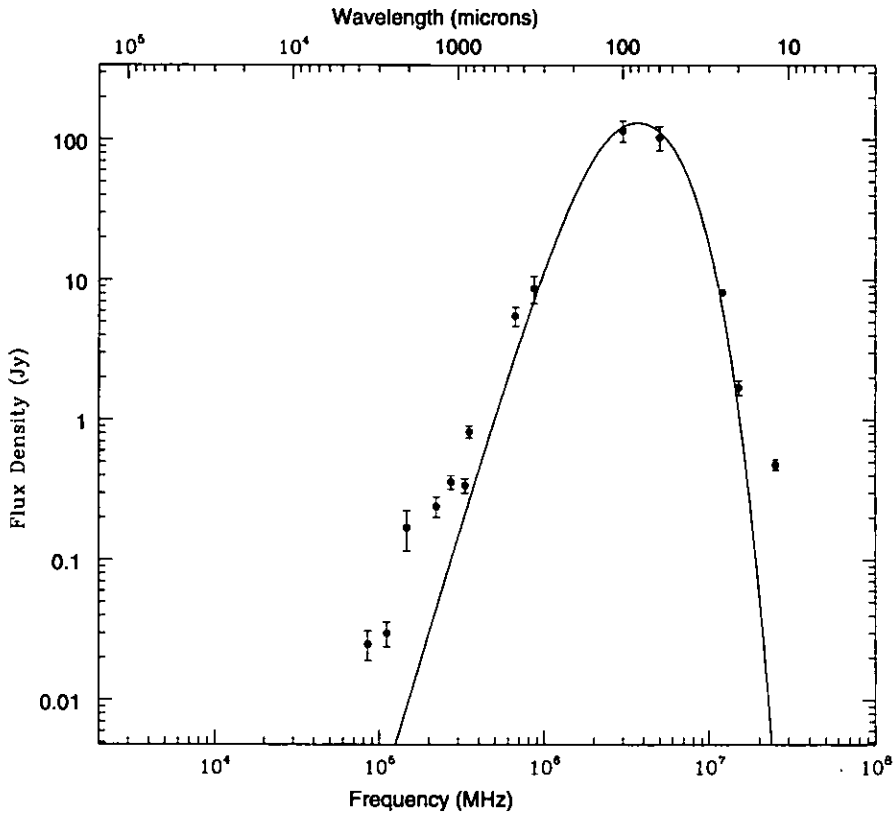

Figure 1.3: An illustrative thermal, 61 K dust emission spectrum fit to the submm-to-infrared data of Arp 220 (c.f. Emerson et al., 1984). The data are courtesy of NED, the NASA/IPAC Extragalactic Database.

When the distance to a source is known and the flux density, emissivity index, and temperature for the thermal emission from the source are determined, the mass of the emitting dust $M_{\rm d}$ can be derived. Using a simple relation adapted from Hildebrand (1983), the dust mass is written as

$$M_{\rm d} = \frac{S_\nu D^2}{k_{\rm d} B(\nu, T)}, \tag{1.2}$$

where S_ν is the measured flux, D the distance to the source, $B(\nu, T)$ the Planck function and $k_{\rm d} = 3Q_\nu/4a\rho$ the grain mass absorption coefficient with a and ρ being respectively

the grain radius and density.

Unfortunately, the advantage of using optically thin submm emission to determine the dust mass is offset by the increased uncertainty of the grain emission efficiency, Q_ν, and subsequently of k_d, as λ is increased from the far-IR to submm wavelengths (Draine, 1990). A different choice of k_d could result in an estimation of the dust mass that differs by a factor ~ 2 (c.f. Hughes et al., 1997). Based on Hildebrand (1983) and Draine (1990), the commonly accepted values of $k_\mathrm{d}^{450\,\mu\mathrm{m}} = 0.25\,\mathrm{m^2 kg^{-1}}$ and $k_\mathrm{d}^{60\,\mu\mathrm{m}} = 3.3\,\mathrm{m^2 kg^{-1}}$ are assumed in this thesis and the dust masses derived using equation 1.2.

1.3.2 Synchrotron Radiation from Relativistic Electrons

Synchrotron radiation refers to emission that results from the acceleration of relativistic electrons in a magnetic field. In the non-relativistic domain, the radiation from the electron, which is called cyclotron radiation, is a dipole in the rest frame, corresponding with the strength of the electric field as a function of angle with respect to the velocity vector of the electron. The non-relativistic magnetic force on the electron is $F = Bev$, where B is the magnetic field strength, e is the charge on the electron and v is the velocity of the electron. The orbital (centripetal) force on the spiralling electron is $F = m_\mathrm{e}v^2/r$, where m_e is the mass of the electron and r is the orbital radius. Equating the magnetic and orbital force, the *frequency* of the electron radiation is simply given by its gyration in the magnetic field, and is thus

$$\nu_\mathrm{g} = \frac{Be}{2\pi m_\mathrm{e}}. \tag{1.3}$$

In the relativistic domain, the radiation of the electron, now called synchrotron radiation, is more complex. Transformed by relativistic effects, the emission is highly peaked

in the forward direction of the velocity vector, giving a cone of radiation in the rest frame of the electron. The emitting, critical *frequency* of the spiralling, relativistic electron is

$$\nu_s = \gamma^2 \nu_g = \gamma^2 \frac{Be}{2\pi m_e}, \tag{1.4}$$

where γ is the relativistic gamma factor given by $\gamma = 1/\sqrt{1 - \nu^2/c^2}$ and υ_g is the non-relativistic gyro-frequency given in equation 1.3. As $E = \gamma m_e c^2$, the radiating frequency, $\nu_s \propto BE^2$. Following work by Pacholczyk (1970), the radiating electrons, averaged over all the pitch angles of the spiralling electrons, lose energy at a rate

$$\frac{dE}{dt} \propto B^2 E^2. \tag{1.5}$$

1.3.2.1 The synchrotron radiation of electrons with a power-law energy spectrum

Astrophysically, it is interesting to consider what happens when an *ensemble* of relativistic electrons radiates due to a magnetic field. It has been noted that the synchrotron radiation of the electrons of energy, E, is sharply peaked near the emitting, critical frequency, $\nu_s \approx \gamma^2 \nu_g$ (equation 1.4), and much narrower than the breadth of the electron spectrum. Therefore, the energy radiated in the critical frequency range ν to $\nu + d\nu$ is emitted by electrons with energies between E and $E + dE$. The energy radiated, $j(\nu)d\nu$, is then

$$j(\nu)d\nu = (-\frac{dE}{dt})N(E)dE, \tag{1.6}$$

where $N(E)dE$ refers to the number density of the electrons. By substituting the equa-

tions of the rate of energy loss (as in equation 1.5) and critical frequency, ν_s, of the radiating electrons, in the appropriate forms, the luminosity, $j(\nu)$, may be expressed in terms of the Doppler shift factor, magnetic field strength, particle (or electron) distribution power-law index, frequency, (respectively, κ, B, p, ν) and the fundamental constants:

$$j(\nu) = (\text{constants})\kappa B^{(p+1)/2}\nu^{(p-1)/2}. \tag{1.7}$$

1.3.2.2 Synchrotron self-absorption

According to the principle of detailed balance, to every emission process, there is a corresponding absorption process. For the mechanism in point, it is known as *synchrotron self-absorption.* Following Longair (1997), the physical arguments for the self-absorption are presented below. If a synchrotron source with a power-law spectrum of $S_\nu \propto \nu^\alpha$ has the same physical size at all frequencies, its brightness temperature is $T_\mathrm{b} = (\mathrm{c}^2/\nu^2 2\mathrm{k})(S_\nu/\Omega) \propto \nu^{(2+\alpha)}$, where S_ν is the flux density, $\alpha = (p-1)/2$ is the emission spectral index, p is the electron distribution power-law index and Ω is the solid angle the source subtends at the observer. Therefore, at low frequencies, the brightness temperature (T_b) of the radiation may approach the kinetic temperature (T_e) of the electrons, resulting in a self-absorption of the radiation.

It is noted that extensive observations of cosmic rays interacting with a weak magnetic field have shown that the synchrotron radiation spectrum is a power-law energy distribution of relativistic electrons. It is further noted that, a power-law spectrum is *not* a thermal equilibrium spectrum of a Maxwellian-electron distribution; this is the reason it is commonly known as a *non-thermal* spectrum. However, the spectrum can still be associated with a temperature for particles of a particular energy E, which is

peaked about the emitting, critical frequency $\nu_s \approx \gamma^2 \nu_g$, where $\gamma = E/m_e c^2 >> 1$ and $\nu_g = eB/2\pi m_e$ is the non-relativistic gyro-frequency. Furthermore, the temperature T_e can be associated with electrons of a given energy through the relation

$$\gamma m_e c^2 = 3kT_e. \tag{1.8}$$

Therefore, the effective temperature of the electrons becomes a function of energy; and, since $\gamma \approx (\nu/\nu_g)^{1/2}$, the effective temperature is

$$T_e \approx (\frac{m_e c^2}{3k})(\frac{\nu}{\nu_g})^{1/2}. \tag{1.9}$$

For a self-absorbed source, $T_b = T_e$, therefore in the Rayleigh-Jeans limit,

$$S_\nu = \frac{2kT\nu^2\Omega}{c^2}, \tag{1.10}$$

where Ω is the solid angle subtended by the source. Substituting the expression for temperature as in equation 1.9, the flux density is

$$S_\nu = \frac{2m_e\nu^{5/2}}{3\nu_g^{1/2}} \propto \nu^{5/2}. \tag{1.11}$$

In summary, the characteristic synchrotron spectrum has an optically thin component that rises with decreasing frequency and has a turnover frequency ν_o. It then falls in the self-absorbed region at $S_\nu \propto \nu^{5/2}$, with decreasing frequency. The self-absorbed component does not follow the standard Rayleigh-Jeans law because the effective kinetic temperature of the electrons varies with frequency (Longair, 1997). The typical spectrum of a self-absorbed radio source is shown in Figure 1.4.

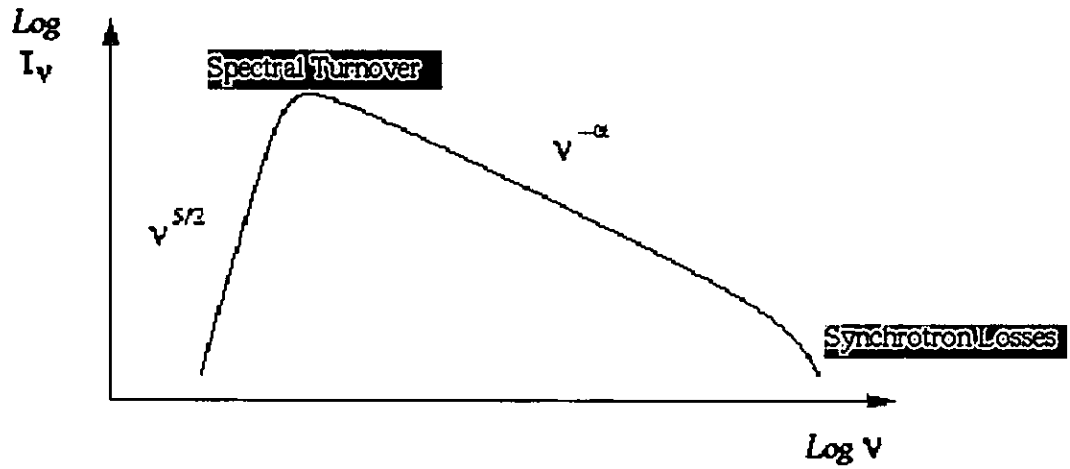

Figure 1.4: A typical self-absorbed synchrotron spectrum of a radio source.

It is noted that if the electron energy spectrum has power law index p, the synchrotron emission of these electrons has a spectral index $\alpha = (p-1)/2$ (see equation 1.7). This is very useful because a measurement of the spectral index from a synchrotron emitting source allows the determination of the power-law index of the electron energy distribution. Indeed, cosmic rays which permeate our galaxy and interact with weak magnetic field produce synchrotron radiation that is a power-law with spectral index $\alpha = -0.7$ ($S_\nu \propto \nu^\alpha$), as determined from radio observations. Observations of extended components of radio galaxies and compact radio-loud nuclei, seen in radio to submm wavelengths, also give synchrotron radio spectral index close to -0.7.

1.3.3 Free-free Radiation from Ionised Gas

Free-free or bremsstrahlung emission is radiation due to the acceleration of a charge in the Coulomb field of another charge. Astrophysically, the common occurrence of free-free radiation is the electron-ion thermal bremsstrahlung continuum emission of a fully ionised, hot gas in which the velocity distribution of the emitting electrons is Maxwellian

at a temperature T. In the mm to submm wavelength regime, thermal bremsstrahlung is commonly detected from diffuse regions of ionised hydrogen at $T \approx 10^4$ K, surrounding very hot O, B type stars in the H II regions. The submm fluxes fit a high-frequency extrapolation of the radio emission spectrum, which is generally the radiation of the H II regions resulting from an interaction of free electrons with positively charged hydrogen ions. The emission is continuous because free electrons can possess a large range of continuum energies; and, in electron-ion bremsstrahlung, the electrons are the primary radiators, since the relative accelerations are inversely proportional to the masses, and the charges are roughly equal, while the ions are relatively more massive (Longair, 1997).

A typical free-free spectrum extends from the optical to the radio, depending on density of the gas (in, say, the H II region). At the long-wavelengths, there is a turnover in the spectrum, which corresponds to the wavelength where, according to the principle of detailed balance or Kirchhoff's law, the effects of self-absorption of the radiation by the same process as the emission become dominant. In more compact astrophysical regions, self-absorption becomes important at higher frequencies. Indeed, in most compact H II regions found in the vicinity of regions of star-formation, a self-absorption bremsstrahlung spectrum can be evident even at the centimetre wavelengths.

The self-absorbed (optically thick) part of the free-free spectrum is given by $I_\nu = 2\mathrm{k}T\nu^2/\mathrm{c}^2$, where I_ν is the emitted intensity as a function of frequency ν. This follows the Rayleigh-Jeans approximation of the Planck function, as $\mathrm{h}\nu << \mathrm{k}T$ in this regime.

In the optically thin part, the spectrum is fairly flat, with a power-law spectral index, α ($I_\nu \propto \nu^\alpha$), of -0.1 up to frequencies $\mathrm{h}\nu \approx \mathrm{k}T$, above which there is an exponential cut-off. It is noted that the intensity of the radiation per unit bandwidth depends on the number density of the electrons, N_e^2, and inversely on the temperature, $T^{-1/2}$. Thus, the

total intensity along a line of sight is

$$I_\nu \propto \int N_e^2 T^{-1/2} \mathrm{d}l. \tag{1.12}$$

For AGN observations, particularly at the longer wavelengths in the mm to submm regime, free-free emission is only important in sources where the bulk of the luminosity comes from regions of star-formation. In the starburst galaxy M 82 for example, free-free emission dominates the 3 mm (90 GHz) fluxes (Kronberg et al., 1985). With the measurement of free-free flux at 3 mm, the flux of ionizing photons in a source can be determined from

$$\mathrm{L_c} \approx 4.75 \times 10^{54} \nu^{0.1} D S_\nu T^{-0.45} s^{-1}, \tag{1.13}$$

where L_c is the number of the continuum photons emitted per second, ν is the frequency in GHz, D is the distance to the source in Mpc and S_ν is the flux in Jy. Such a determination is expected to be more direct and reliable for determining the number of ionizing photons in a target source than other used methods (Gear, 1988).

It is noted in passing that at X-ray wavelengths, bremsstrahlung has been observed from diffuse, very hot intergalactic gas in rich clusters of galaxies and from shells of supernova remnants (Longair, 1997). It is further noted that free-free radiation might be important in ionised regions surrounding a hot central engine of an AGN, and could possibly provide the best explanation of the origin of the big blue bump seen in some quasar continuum emission (see e.g. Robson, 1996).

1.4 Summary of Thesis and Collaborations

This thesis project describes submillimetre continuum observations using SCUBA to undertake imaging at a number of submm wavelengths of a selection of nearby galaxies with interesting properties. Millimetre and submm photometry and imaging observations are used to study (1) the properties, content and structure of cool to cold dust (2) the energy distribution of synchrotron electrons and (3) the large-scale outflows in the selected, active galaxies Cygnus A, NGC 4374, Centaurus A and M 82.

All the work in the thesis was undertaken by myself under supervision from Prof. Ian Robson. Some collaborative observations of Cygnus A had been preliminarily obtained by Drs. Jason Stevens and Wayne Holland. The programme on NGC 4374 was a collaboration on diffusely distributed dust in *IRAS* selected elliptical galaxies. Dr. Anne Sansom (UCLan), who is the principal investigator for that programme, devised the simple dust/torus emission model fitted to the data for this object (see section 4.3.1). Preliminary observations of M 82 were done in collaboration with Dr. David Hughes, following up previous work with Ian Robson. Observations of Centaurus A are a combination of data sets obtained by myself and Ian Robson and those by Drs. Henry Matthews and Tim Hawarden. Observations have also been made of M87 as part of a programme by my second supervisor Dr. Tim Cawthorne (UCLan). This source will feature in a *post*-thesis study (Leeuw et al., in preparation), that is outside the scope of the work described here.

Chapter 2

Millimetre and Submillimetre Continuum Techniques

2.1 Preface

This chapter presents millimetre (mm) and submillimetre (submm) continuum observing techniques, with a special focus on the James Clerk Maxwell Telescope (JCMT)'s Submm Common-User Bolometer Array (SCUBA), the instrument with which most observations in this thesis were made. The chapter ends with a brief section discussing the reprocessing of Infrared Astronomy Satellite (*IRAS*) data using HIRES and SCANPI routines at NASA/IPAC. The HIRES reprocessed *IRAS* data have a higher resolution than earlier presentation of the *IRAS* observations and the far-infrared data (60 and 100 μm) in particular make an important complement to the SCUBA observations in this thesis. The SCANPI data are a co-addition of the *IRAS* raw survey data and provide better constraining flux estimates (or local upper limits) of the target sources, particularly for the confused or faint sources.

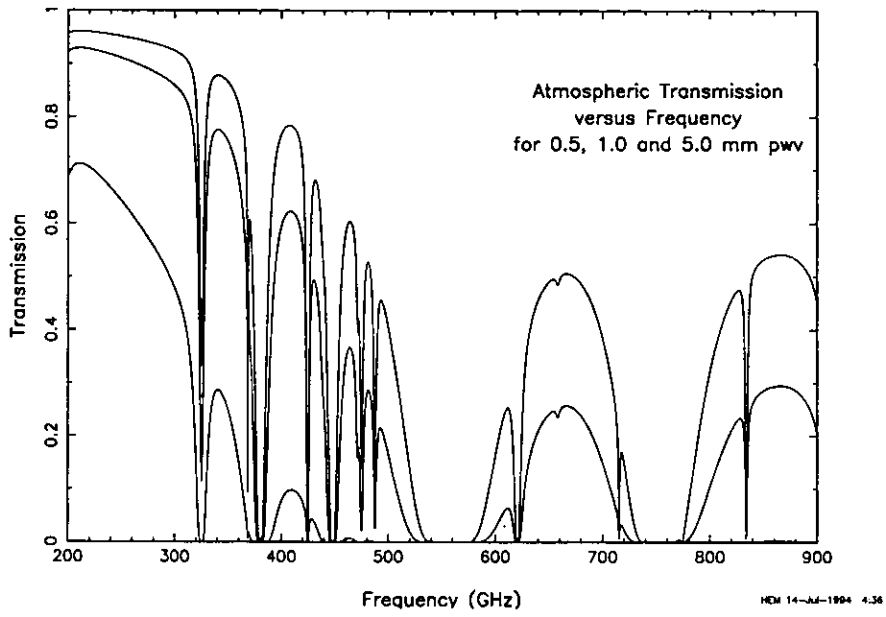

Figure 2.1: Atmospheric transmission calculated as a function of frequency in the submm window for three different water vapour pressures (1 mm pwv is 'good', 0.5 mm pwv 'exceptional', and 5 mm pwv is 'very poor'). Reproduced from the JCMT Guide 1998.

Millimetre and submm observations are strongly affected by precipitable water vapour (pwv) and, to a lesser extent, by other atmospheric constituents. The opacity of the atmosphere increases generally with frequency until observations from the ground are virtually impossible for $\lambda < 300\,\mu$m (Masson, 1994). The submm observations are restricted to semi-transparent windows between strong absorption lines of atmospheric water. Figure 2.1 and Table 2.1 respectively show such transmission windows and the calculated, representative values of the atmospheric transmission at the zenith above the high (4200m), dry site of Mauna Kea, Hawaii. The last two columns in Table 2.1 are respectively the atmospheric transmission for 0.5 mm pwv and the percentage of 'good' nights at a number of representative frequencies (chiefly those of CO transitions [JCMT User Guide 1998]).

Although submm observations are difficult, they have great astrophysical importance.

Table 2.1: Overview of JCMT and Mauna Kea Atmospheric Parameters

Frequency (GHz)	Wavelength (μm)	Aperture Efficiency†	Beamwidth (arcsec)	Atmos. trans.	Nights (%)
150	2000	0.66	28	0.97	90
230	1300	0.63	21	0.96	90
345	870	0.56	14	0.88	70
492	610	0.46	12	0.43	20
690	435	0.32	8	0.44	25
870	345	0.21	6	0.53	30

† Aperture efficiency calculated assuming the rms surface accuracy is 30μm

This has been recognised in recent years by the construction of several large telescopes (JCMT, CSO, IRAM and SEST), originally built based on the scientific case primarily for submm spectroscopy. The continuum observations, distinct from spectroscopy, in many respects came along as "add-ons", but with time gained more importance. This was especially true at the JCMT, where UKT14, the single-pixel bolometer that was the predecessor of SCUBA, came to be used for about 50% of telescope observing time. The trend continued with the building of new generation of array detectors (SCUBA, SHARC, MPIfR) that are dedicated to continuum observations in this wavelength regime. The JCMT is now a strongly continuum-focused facility. The new generation of array detectors, as some results presented in this thesis show, have made discoveries that highlight the importance of submm astronomical observations. Now there is a spur of investment in the next generation continuum detector arrays (SCUBA 2, SHARC II, Bolocam, MAMBO 2), as well as new submm ground and space telescopes (SMA, LMT, ALMA, Hershel, SIRTF), whose scientific cases emphasise continuum observations.

2.2 SCUBA on the JCMT

The JCMT is a 15-m antenna designed to observe in the mm and submm (2 mm to 350 μm). It is situated on Mauna Kea, Hawaii, a very dry site that is about 13800 feet

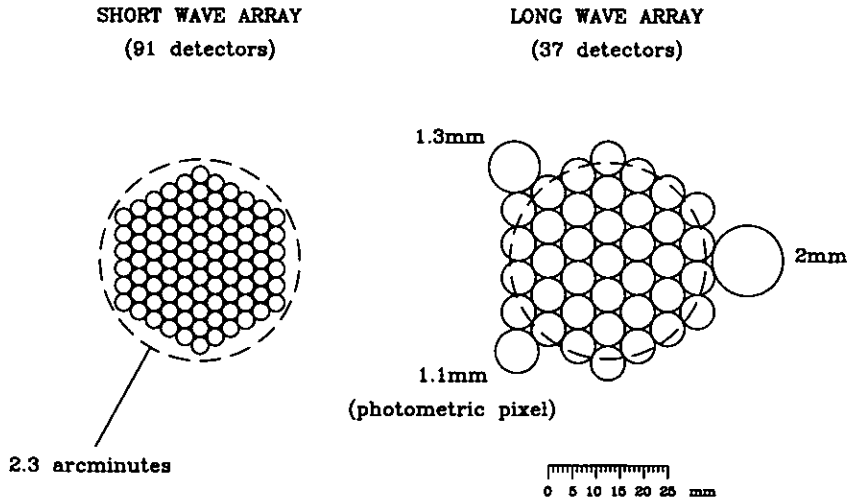

Figure 2.2: Pixel layout of the SCUBA arrays, reproduced from Holland et al. (1999).

(4200 m) above sea-level. Some essential properties of the site and atmosphere above the JCMT are highlighted in Figure 2.1 and Table 2.1.

SCUBA is a new-generation, versatile and powerful submm camera that operates at the Nasmyth focus of the JCMT (Holland et al., 1999). SCUBA has a 91 pixel short-wave (SW) array that is optimised to operate at 450 or 350 μm and a 37 pixel long-wave (LW) array that is optimised to operate at 850 or 750 μm (see Figure 2.2). Both arrays have a $2'.3$ instantaneous field-of-view, and the optics are designed such that with a suitable jiggle pattern of the secondary mirror of the telescope, fully sampled maps can be obtained simultaneously at 450 and 850 μm or 350 and 750 μm. As shown in Figure 2.2, SCUBA also has single element bolometers optimised to operate at 1100, 1350 and 2000 μm.

2.2.1 SCUBA Bolometers

In general, bolometer detectors have a large instantaneous bandwidth and therefore, are more sensitive than heterodyne receivers. This withstands the fact that, in practice,

the filter profile is often reduced to a relatively narrow bandwidth in order to reduce degradation in performance through background power loading of the cooled detector.

SCUBA bolometers are made of a thin film of bismuth mounted on sapphire. A small chip of neutron transmutation doped germanium is glued to the centre of the bolometer and measures tiny temperature changes due to incident photons on the bismuth-sapphire composite. Brass wires that govern thermal conductance make electrical connections leading out of the tightly packed 131-bolometer mounts that make-up the SCUBA array. The bolometers are cooled to operating temperature of 100 mK and were designed to achieve background limited performance under low sky-background. In practice the bolometers are limited by the background of the system (dominated by the optics box) rather than the sky. As the background is not variable, this has, in some ways, made the operation easier. The measured electrical noise equivalent power (NEP) of the bolometers varies by $\sim 20\%$ across the array.

2.2.2 SCUBA Filters

The SCUBA filters are designed to exploit the "windows" that are available for observing in the submm waveband (see Section 2.1 and Figure 2.1). The multi-layer, metal mesh interference filters are located in a nine-position filter-drum that is cooled to 4 K. They ensure that the SCUBA wavelength profiles match the selected observing windows, maximizing transmission of the source signal (typically to over 80%) and minimizing the contribution of extraneous sky emission to the target signal. The rotating filter-drum allows observations to be made simultaneously at 450 and 850 μm and also at 350 and 750 μm, or individually at 1100, 1350 and 2000 μm. To minimise the thermal load on the SCUBA detectors, optical and near-infrared radiation are blocked by an alkali-halide

filter, cooled to around 90 K and located on the outer radiation shield of the cryostat (Holland et al., 1999).

2.2.3 SCUBA Optics and Image Sampling

The submm input beam from an astronomical source is reflected from the primary to the secondary and tertiary mirrors of the JCMT. The beam is then relayed by these mirrors and sent through the SCUBA thermal-load blocking filter (which is cooled to about 90 K). An internal Gaussian-beam telescope then relays the beam via a dichroic beam splitter (partitioning it for the SW and LW arrays) through bandpass filters (which are cooled to about 4 K) and through feedhorns that feed individual SCUBA detectors (which are cooled to about 65 mK). In order to achieve optimal collecting efficiency, the entrance diameter of the feedhorns at the detectors is $2f\lambda$ (i.e. $2 \times$ the FWHM of the Airy pattern), where f is the focal ratio of the beam. Unfortunately, this is four times the required detector or pixel separation to achieve a fully sampled image. (The Nyquist sampling required to achieve a fully sampled image is $< f\lambda/2$). In other words, the image is significantly undersampled. Therefore, to obtain a fully sampled SCUBA image at *one* wavelength requires four offsets in the orthogonal directions. This is achieved by "jiggling" the secondary mirror over a 16-point pattern to fill in the gaps, as shown in Figure 2.3. However, the spatial resolution of the SCUBA arrays is the diffraction limit in the wavelength in question, being $7''$ at $450\,\mu$m, which is half the $14''$ resolution at $850\,\mu$m. Therefore, to obtain a diffraction limited map at both wavelengths simultaneously, a 64-point jiggle pattern is required.

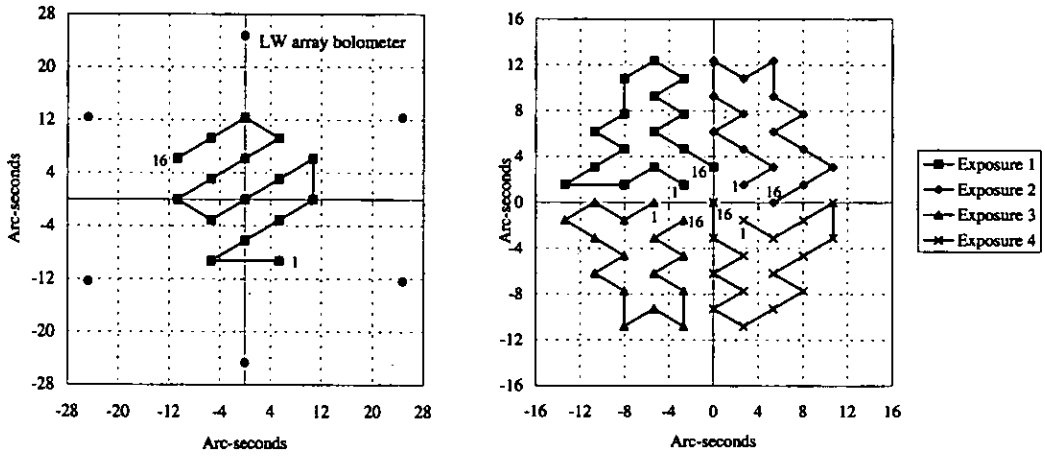

Figure 2.3: The jiggle pattern used to fully sample the SCUBA maps, reproduced from Holland et al. (1999).

2.2.4 SCUBA Observing Modes

As mentioned above, the **jiggle mapping** observations employ a 16-point jiggle pattern (see Figure 2.3) to fully sample *an individual* SW or LW array over a period of 32 s (1 integration). For fully sampled images with both arrays (e.g. at 450 and 850μm), a 64-point jiggle pattern with a 3″ offset between each position (see Figure 2.3) is performed over a period of 128 s (1 integration). Since the spacing of the SW bolometers is about half that of the LW, this ensures that the area between the LW array pixels is covered at the resolution required to fully-sample the SW array. Each integration is divided into 4 so that the telescope can be nodded between the signal and reference beam every 16 s. Using specific single bolometers (e.g. the central ones) of the LW and SW arrays and a simpler jiggle pattern, faster **photometric mode observations** can instead be obtained simultaneously at 450 and 850 μm, or 350 and 750 μm. The photometry mode observations employ a 9-point jiggle pattern in a 3 by 3 grid of 2″ spacing, taking 9 seconds on the signal and 9 seconds on the reference beams (1 integration). The 1350 and 2000 μm observations use the single photometry bolometers and also employ the 9-

point jiggle pattern. Averaging the source signal in an area slightly larger than the beam is intended to achieve the best photometry accuracy under good-to-moderate seeing; and, in case of the simultaneous observations with the LW and SW arrays, to also compensate for the small offset between the arrays.

Two additional observing modes, scan-mapping and polarimetry, are also available with SCUBA. The **scan-mapping mode** allows SCUBA to observe regions larger than the 2′.3 field-of-view of the camera, by rapidly scanning the array over the region to be mapped in a raster mode and adding the data. In the traditional rastering technique, chopping was done in one direction on the sky, resulting in a map that has the source signal convolved with the chop. Deconvolving the chop was problematic where the Fourier transform of the chop is low or near zero and thus introduced noise in the restored map. A new form of rastering follows a technique that was first described by Emerson (1995), and is locally called Emerson II, where maps of the same region are taken with several chop throws and directions. This ensures that the zeroes of one FT do not coincide with the zeroes of another and has been shown to improve the S/N over the traditional technique (Jenness et al., 1998).

For the **polarimetry** mode observations, SCUBA has a polarimeter attached (an additional photolithographic analyser along with a rotating half-wave plate to select one plane of polarization). The polarimeter has not been used in this thesis.

2.3 Millimetre and Submm Extinction Correction

As shown in Figure 2.1 and Table 2.1, the atmosphere strongly attenuates the submm signal and therefore, extinction correction is a dominant uncertainty in submm observations, especially at the short wavelengths, where the transmission is at best 50% at zenith.

Assuming a plane-parallel, homogeneous atmosphere, the extinction varies exponentially with the airmass, i.e.

$$I_{obs} = I_0 \times e^{-\tau_0 A}, \tag{2.1}$$

where I_{obs} is the observed signal, I_0 is the intrinsic signal that one would measure above the atmosphere, τ_0 is the optical depth at zenith and A is the airmass (the secant of the zenith distance).

The traditional method of determining extinction is by following a bright, known source, typically a planet, observing it at different airmasses (minimum 3) and making a least-squares fit to the above equation. The method, known as the secant method, is subject to major uncertainties because it assumes the sky is constant or homogeneous, which is seldom the case (Sandell, 1994). The atmospheric water vapour above the telescope is a function of time and position of the object in the sky. The secant method also suffers from the poor sky coverage available from bright sources, particularly planets; therefore, in general this method makes it very difficult to determine atmospheric extinction at the position of the target source (Duncan et al., 1990; Stevens & Robson, 1994).

A focal plane calibration system that involves performing *skydips*, such as recently employed at the JCMT with the arrival of SCUBA, can overcome the difficulty of determining atmospheric extinction at the position of the target source. It allows monitoring of the sky transmission of submm radiation *wherever* the antenna is pointing and *whenever* it is convenient for an observer to do so. Skydips with SCUBA measure the sky temperature over a range of elevations, typically between 15 and 80 degrees. At each elevation, a focal plane chopper wheel allows SCUBA to alternate between observing the

sky and ambient and liquid cooled loads. The temperatures of the ambient and cold loads are measured and adjusted to match the profiles of the SCUBA filters. Thus observations of the sky are calibrated. The zenith sky opacity is then estimated from fitting a model of both the atmosphere (assumed to be plane-parallel) and the data .

On Mauna Kea, a dedicated atmospheric transmission monitor, the Caltech Submillimeter Observatory (CSO) radiometer, performs such skydips regularly. The radiometer operates at 225 GHz (1.3 mm) and provides a record of the opacity (commonly referred to as $\tau_{\rm CSO}$) at all frequencies since the opacity at 225 GHz can be scaled to the opacity at other frequencies. Such scaling factors are determined from theoretical models and extrapolations from experimental data (e.g. Masson, 1994; Stevens & Robson, 1994). The opacity at a given wavelength (τ_λ) is

$$\tau_\lambda = k_\lambda \times (\tau_{\rm CSO} - B), \tag{2.2}$$

where k_λ is the scaling factor and B is the oxygen contribution to the τ_λ opacity (the rest of the contribution is from the PWV in the atmosphere). The uncertainties in the scaling factors are highest at the higher frequencies, again since the atmospheric extinction of the submm signal is strongest at these higher frequencies.

2.3.1 Calculating Sky Opacities with SCUBA

In order to make extinction corrections to the SCUBA data presented in this thesis, the zenith sky opacity, τ, was estimated using two common methods used for this purpose at the JCMT: (1) performing skydips with SCUBA and (2) extrapolating the τ at the SCUBA filters from the τ at 225 GHz ($\tau_{\rm CSO}$) measured by the CSO radiometer. The two

methods are described below, particularly as they relate to their relevance in this thesis.

Skydips with SCUBA

Theoretically, SCUBA skydips are preferred because they can give an estimate of the sky opacity wherever the telescope is pointed, and therefore at the local time and azimuth of the target source. Since the objective is to correct the data from the target source, this is important because the atmosphere water vapour is, as mentioned above, a function of time and position in the sky. In practice, the skydips have overheads and it is only reasonable to perform them about every 2 hours in an observing run, and quite often less frequently. Furthermore, in mediocre to poor weather, the skydip model has trouble fitting the data, particularly at the short wavelengths. From quite early on in this thesis project, the visual inspection and the resultant often-high χ^2 of the SCUBA skydip model showed that the fitting to the 450μm data was unreliable when $\tau_{\rm CSO} > 0.08$, and the fitting to the 350μm data was almost always untrustworthy, regardless of the weather. This was the case even after off-line reduction of the model fitting, often involving a removal of a couple of "bad" points in the data sets. This off-line reduction was necessary for all the estimation of τ_{450} and the τ at the long wavelength (i.e. 750 and 850μm) in bad weather.

Using $\tau_{\rm CSO}$ in SCUBA observations and data correction

Firstly, the $\tau_{\rm CSO}$ measurements were exploited as one of the key indicators in monitoring and forming a basis to make short-term forecasts of weather conditions on Mauna Kea. The high frequency 15 minute-intervals with which the measurements are made (when the CSO radiometer works) is important in this regard. This was useful for planning

submm observations before going up to and while working at the telescope.

The second exploitation of the τ_{CSO}, and perhaps the most crucial one, was in using it to extrapolate the τ at the SCUBA wavelengths. Doing this makes redundant the need to perform SCUBA skydips frequently, if at all, and therefore minimises the overheads associated with skydips. However, one disadvantage is that, unlike τ's derived directly with SCUBA, the CSO-derived τ's are most often not for the area of the sky where the JCMT is pointing and therefore not local to the SCUBA target source. The second disadvantage is that extrapolation to the SCUBA filters increases the uncertainty in the estimation of the needed τ. While nothing can be done about the former disadvantage, the latter can be made insignificant by deriving relations from correlations with minimal scatter. At the JCMT, these relations are derived empirically. Therefore, they have been periodically updated and improved as more data, especially since the commissioning of SCUBA, have been obtained (e.g. Archibald, Wagg, & Jenness, 2000 [1] [hereafter AWJ00]).

Table 2.2: Typical CSO relations used in this thesis project

τ_{850}	=	$4.3 \times (\tau_{CSO} - 0.007)$,
τ_{450}	=	$23.9 \times (\tau_{CSO} - 0.01)$,
τ_{450}	=	$6.5 \times (\tau_{850} - 0.03)$.

The typical relations used during the course of this Ph.D. are listed in Table 2.2. The latest relations for τ_{450}, τ_{850} and τ_{CSO} were derived by AWJ00 and are listed in Table 2.3. These have not been used in this thesis as they were derived after all the data reductions presented here were undertaken. With these recent relations is obtained an estimate of τ_{450} and τ_{850} that differs from the earlier estimates by no more than 10%. The

[1] This latest documentation is available at the Joint Astronomy Centre web site, http://www.jach.hawaii.edu

reason for the small discrepancy is because the estimate of the τ values in this thesis were calculated with special care. As described above, all the SCUBA skydips model fittings were checked off-line and only the τ estimates from good fits were used; otherwise, an extrapolation was made from the CSO-SCUBA τ relations, which though becoming more robust with time, have generally been reliable (AWJ00).

Table 2.3: New CSO relations derived for October 2000 by JCMT staff AWJ00

τ_{850}	=	$3.99 \times (\tau_{CSO} - 0.004)$
τ_{450}	=	$23.5 \times (\tau_{CSO} - 0.012)$
τ_{450}	=	$5.92 \times (\tau_{850} - 0.032)$

2.4 Sky-Noise Removal in the Millimetre and Submm

Besides attenuating the submm signal, the atmosphere (and immediate surroundings of the telescope) contribute thermal radiation that is always relatively higher than the target signal. The thermal emission from the sky manifests in two ways: (1) in a DC offset and (2) in temporal and spatial variations in the emissivity of the atmosphere on short time-scales, which degrades the available sensitivity, especially during long integrations and particularly at the higher frequencies.

The DC offset is removed by chopping and nodding. However, since the spatial and temporal variations of the sky emission are on scales comparable to the chop throws, the chopped beams travel through slightly different atmospheric paths and the sky-noise (i.e. the variations of the background thermal emission) is not removed completely. Reducing the chop throw has been shown to decrease the effects of sky-noise. On the JCMT, adopting a throw of 120″ instead of 30″ to 40″ can produce a degradation in S/N of up to a factor of 2 (Holland et al., 1999). On the other hand, to prevent beam cancellation,

a minimum of 3× beamsize is required. Also, in some cases, one is forced to adopt a large throw in order to ensure that the chopping is away from emission from an extended region or known neighbour of the target object.

Observing with the SCUBA array allows for the removal of sky-noise by subtracting emission from off-source bolometers that are viewing the 'blank-sky'. The residual sky-noise is removed off-line by using quiet (or 'blank-sky') SCUBA array bolometers in which there is no source emission. Usually the bolometers in the first ring (for LW) and second ring (for SW) from the centre are used to remove this sky emission. For the 1350 and 2000 μm photometry observations, residual sky emission is not removal as the observations use only a single bolometer.

2.5 Millimetre and Submm Flux Calibration

An ideal calibration source should be bright, compact and non-variable. Unfortunately such sources do not exist for submm observations. Planets are the best choice, but even here present problems due to their extended nature, variability and, in some cases, excess brightness. Primary submm calibration is taken from Mars (Wright, 1976) and Uranus (Orton, 1986; Griffin & Orton, 1993). When planets are not available, secondary calibration is done with (1) ultracompact HII regions in which most of the radiation is in the submm, (2) low-luminosity protostars that are cold and dust rich and (3) asymptotic giant branch stars that are surrounded by large dust-rich envelopes. None of these secondary calibrators fulfil all the criteria of an ideal calibrator (bright, compact and non-variable) but they are the best choices available for submm observations (Sandell, 1994).

2.5.1 Flux Calibration with SCUBA

Mars and Uranus are the primary submm calibrators and were used as top priority for calibrating data presented in this thesis. The SCUBA data were calibrated using instrumental gains that were determined from beam maps of either of the two planets nightly. Ideally, the calibration observations were made in the same observation mode and chop throw and chop waveform as the target observation. Planetary fluxes for each filter were obtained using the JCMT utility program FLUXES. On the nights when the planets were not available, e.g. during the January and February 1998 runs, the JCMT secondary calibrators CRL 618, CRL 2688 or IRC +10216 were used. Fluxes for the secondary calibrators were obtained from Sandell (1998), with occasional reference to Sandell (1994). The list of calibrators (primary or secondary) used for respective nights and observations are listed in tables in the relevant chapters. The instrumental 'gain', or, strictly, the flux conversion factor, is given by

$$C_\lambda = \frac{S_{\mathrm{astrophysical}}}{I_{\mathrm{instrumental}}}, \tag{2.3}$$

which is in Jansky (Jy)/Volts (V), and converts the output data from Volts, the instrumental signal measure, to Jansky, a very useful infrared to radio wavelength astrophysical flux density measure.

2.6 *IRAS* reprocessed Data

The reprocessing of *IRAS* data using HIRES or SCANPI[2] routines is undertaken at NASA/IPAC following email requests. The reprocessed data are available electronically by ftp in the form of several files of the target source maps, diagnostic maps, graphs and text. As with the SCUBA data presented here, the HIRES and SCANPI data were analysed using STARLINK programs after being converted to the required formats.

2.6.1 HIRES

HIRES is an iterative process that uses the Maximum Correlation Method (Aumann et al., 1990) to produce images with better resolution than that nominal for the *IRAS* data. In general, the process works very well, providing a powerful tool for studying morphology in the *IRAS* waveband observations and for separating confused sources.

The HIRES images produced for this thesis used the processing defaults of the IPAC data centre, as they were suitable for the target sources. Typically, the image size was $1 \times 1^{\circ}$ and the pixel size was $15''$. The algorithm produced maps at the 1st, 5th, 10th and 20th iterations. With the output maps, diagnostics imaging tools were produced, including surface brightness and beam maps.

The resolution achieved can be better than an arcminute, roughly a five-fold increase over the unenhanced resolution. This resolution varies from band to band and also from point to point within a single map. The band to band variation is due to the expected, inherent point spread differences between *IRAS* bands. Illustrative resolutions at 12, 25, 60 and 100μm after 1 and 20 iterations are shown in Table 2.4. The one reason for the

[2]The latest HIRES and SCANPI documentation, around which this section is based, is available at the NASA/IPAC web site, http://www.ipac.edu

variation within a map is signal-to-noise variation from source-to-source. This is not a concern in the current thesis because only one target source is analysed in each map.

Table 2.4: Illustrative HIRES Resolutions after 1 and 20 iterations

	12μm	25μm	60μm	100μm
1 iteration	$256 \times 66''$	$270 \times 64''$	$301 \times 121''$	$304 \times 284''$
20 iterations	$37 \times 23''$	$35 \times 23''$	$62 \times 41''$	$98 \times 80''$

Further consideration about HIRES images is the dynamic range, which is limited to 1:100 on small spatial scales. The fluxes measured on the intensity maps agree to the *IRAS* Point Source Catalog to within 20%. The flux stability over the course of iteration varies by 20%, and is only conserved when most of the resolvable structure has been resolved.

2.6.2 SCANPI

SCANPI co-adds *IRAS* scans that all passed within $\approx 1'.7$ of a target position. After retrieval, archival data are re-sampled to facilitate alignment. Then baselines are fitted and residual noise is computed for each scan. The scans are co-added in four ways: straight mean, noise-weighted mean, median and mean with noisy detectors half weighted. Among other things, the co-added scans are analysed to find the peak, determine if a signal exists and compute the integrated fluxes and the full width at quarter and half maximum. Flux estimation is expected to agree to within $\approx 1\sigma$ between the methods of co-addition. Though no single method is supposed to produce the best flux estimate, the median is said to be consistently the *good* estimator of the methods. The SCANPI data are not only useful for obtaining fluxes for point or slightly extended faint or confused sources, but can be useful for estimating local upper limits, and are handy for diagnosing source extent.

Chapter 3

Millimetre and Submillimetre Continuum Observations of the Core and Hotspots of Cygnus A

3.1 Introduction

Cygnus A is locally the most powerful Fanaroff-Riley (FR II) radio galaxy and therefore it is also the best studied in terms of spatial resolution. It has even had an entire workshop devoted to it and global properties of the object are well reviewed in these references (Carilli et al., 1998; Carilli & Barthel, 1996; Carilli & Harris, 1996). Cygnus A has featured prominently in the quest for the unification of powerful radio galaxies and quasars, being cast as the classical case of a quasar in the plane of the sky (Antonucci & Miller, 1985; Barthel, 1989). In terms of the synchrotron emission, at low radio frequencies the two giant lobes dominate the emission (Hargrave & Ryle, 1974), but at higher frequencies the hotspots, or working surfaces in the lobes, become more prominent along with the

galaxy core. The southern and northern hotspots are respectively 50″ and 70″ from the core. Using a Hubble constant of $75\,\mathrm{km\,s^{-1}\,Mpc^{-1}}$ and a redshift of $z = 0.0562$ (Stockton et al., 1994), Cygnus A lies at a distance of 227 Mpc.

Deep Very Large Array (VLA) images reveal the thin jet which transports energy from the AGN core to the radio lobes (Perley et al., 1984). Very Long Baseline Interferometer observations by Linfield (1985) and other authors, and most recently by Krichbaum et al. (1998), have extended this picture at sub-milliarcsecond resolution. The fact that the electron synchrotron lifetime in the hotspots is less than the light travel time from the central core (Hargrave & Ryle, 1974) means that electron re-acceleration must take place in the lobes, and the hotspots are believed to be the working surfaces at which this re-acceleration takes place. Indeed, the prominence of hotspots at the outer edges of the lobes is one of the identifying features of FR II radio sources (Fanaroff & Riley, 1974). The precise mechanism for the electron acceleration is uncertain and determination of the synchrotron spectral index is important as it can rule out some potential mechanisms.

For a steady injection model (Bell, 1978), a steepening of 0.5 in the index is expected at a certain frequency as the electrons lose energy more rapidly than is being supplied by the acceleration process. At some higher frequency, the electron spectrum will cut-off as the high energy electrons rapidly lose energy and become depleted; this produces the final turnover and steep downturn of the synchrotron emission. The emission from the hot-spots (denoted by A and D in the convention derived from VLA maps, where A is the north-west and D is the south-east hot-spot) has been well observed at a number of radio frequencies (Wright & Birkinshaw, 1984; Carilli et al., 1991; Salter et al., 1989; Eales et al., 1989). Both are found to have an excellent power-law spectral index with a coefficient of about -0.5 between 0.1 GHz to around a few GHz, steepening to an index

of -1.0 at higher frequencies. The break to the higher index occurs at around 10 GHz for both hotspots. The spectral break of 0.5 is indicative of the steady injection model with constant radiative losses.

The spectral shape of the core of Cygnus A is much less well determined than the hotspots. The general shape is of a power-law, which is self-absorbed below a few GHz, and above which it has an index of around -0.1, but with significant uncertainty (Salter et al., 1989; Eales et al., 1989).

This thesis presents high frequency (150 – 857 GHz) photometry of the hotspots A and D (there is no visible evidence for a separate component B at this spatial resolution) and the galaxy core. Single-pixel photometry data are given for frequencies of 150 and 222 GHz, and the first submm imaging photometry at frequencies of 353, 400, 667 and 857 GHz (corresponding to wavelengths of 2000, 1350, 850, 750, 450 and 350 μm respectively) are presented.

3.2 Observations

The imaging and photometry observations were made with SCUBA (see Chapter 2) on 1997 May 02, Sep 18, Oct 02 and 1998 Feb 14 and 16. Observations were made in the faster photometric mode only on 1998 Feb 14 in order to go deeper and reduce flux uncertainties, especially at 450 μm. For the imaging observations of Cygnus A, the 64-point jiggle mapping mode was employed. The telescope was pointed at the core of the optical galaxy using radio positions from Hargrave & Ryle (1974). The radio hotspots are about 65″ from the core, thereby nicely fitting within the instantaneous SCUBA field-of-view. For the photometry mode observation, the 9-point jiggle pattern mode was employed. In this mode, the telescope was pointed at the radio core position, and at

each hotspot using the positions from Salter et al. (1989).

The data were calibrated using instrumental gains that were determined from beam maps of Mars or Uranus nightly and in the same observation mode as the target observation. During the 1998 Feb runs, the planets were not available and the JCMT secondary calibrators CRL 618, CRL 2688 and IRC +10216 were used (see Chapter 2).

The results from the imaging and photometry observations are shown in Table 3.1. The uncertainties are a quadratic sum of the uncertainty arising from the measured signal-to-noise-ratio and a systematic calibration uncertainty, which varies from 10% at 850 μm and lower, to 27% at 450 μm.

In addition to SCUBA observations, *IRAS* data were reprocessed using HIRES and SCANPI routines at NASA's Infrared Processing and Analysis Center (IPAC). The re-reduced 12, 25 and 60μm data agree well with previous determinations (Fullmer & Londsdale, 1989; Knapp et al., 1990; Golombek et al., 1988). There is some disagreement about the 100 μm value; Golombek et al. (1988) indicated that the upper limit flux density was 1.8 Jy, however Fullmer & Londsdale (1989) gave a significantly different upper limit of 8.3 Jy. The reason for disagreement is because the published upper limits have been determined in different ways. Cygnus A has a low galactic latitude ($b = 6°$), and the 100μm flux is contaminated by cirrus (Low et al., 1984). From the HIRES images it is clear that the cirrus contamination is dominant and the true Cygnus A flux at 100 μm cannot be retrieved from *IRAS* data even with unusually high iterations of HIRES processing. Moreover, photometry on the HIRES images produced a 3σ upper limit of 5.1 Jy.

Table 3.1: SCUBA Fluxes of Cygnus A's Core and Hotspots.

	Flux density (Jy)									
UT Date	2.0 mm	$\sigma_{2.0}$	1.35 mm	$\sigma_{1.35}$	0.85 mm	$\sigma_{0.85}$	0.75 mm	$\sigma_{0.75}$	0.45 mm	$\sigma_{0.45}$
Core										
19980214					0.49	0.05			0.23	0.04
19980216	0.72	0.11	0.78	0.15						
19971002							0.51	0.05		
19970918	1.11	0.1	0.65	0.10	0.46	0.06				
19970502					0.53	0.05			0.34	0.06
NW Hotspot										
19980216	2.49	0.37	1.20	0.23						
19971002							0.67	0.06		
19970918	2.07	0.20	0.95	0.14	0.57	0.08				
19970502					0.68	0.06			0.23	0.06
SE Hotspot										
19980216	3.54	0.53	1.76	0.33						
19971002							0.81	0.08		
19970918	2.65	0.2	1.56	0.23	1.01	0.14				
19970502					0.95	0.05			0.43	0.07

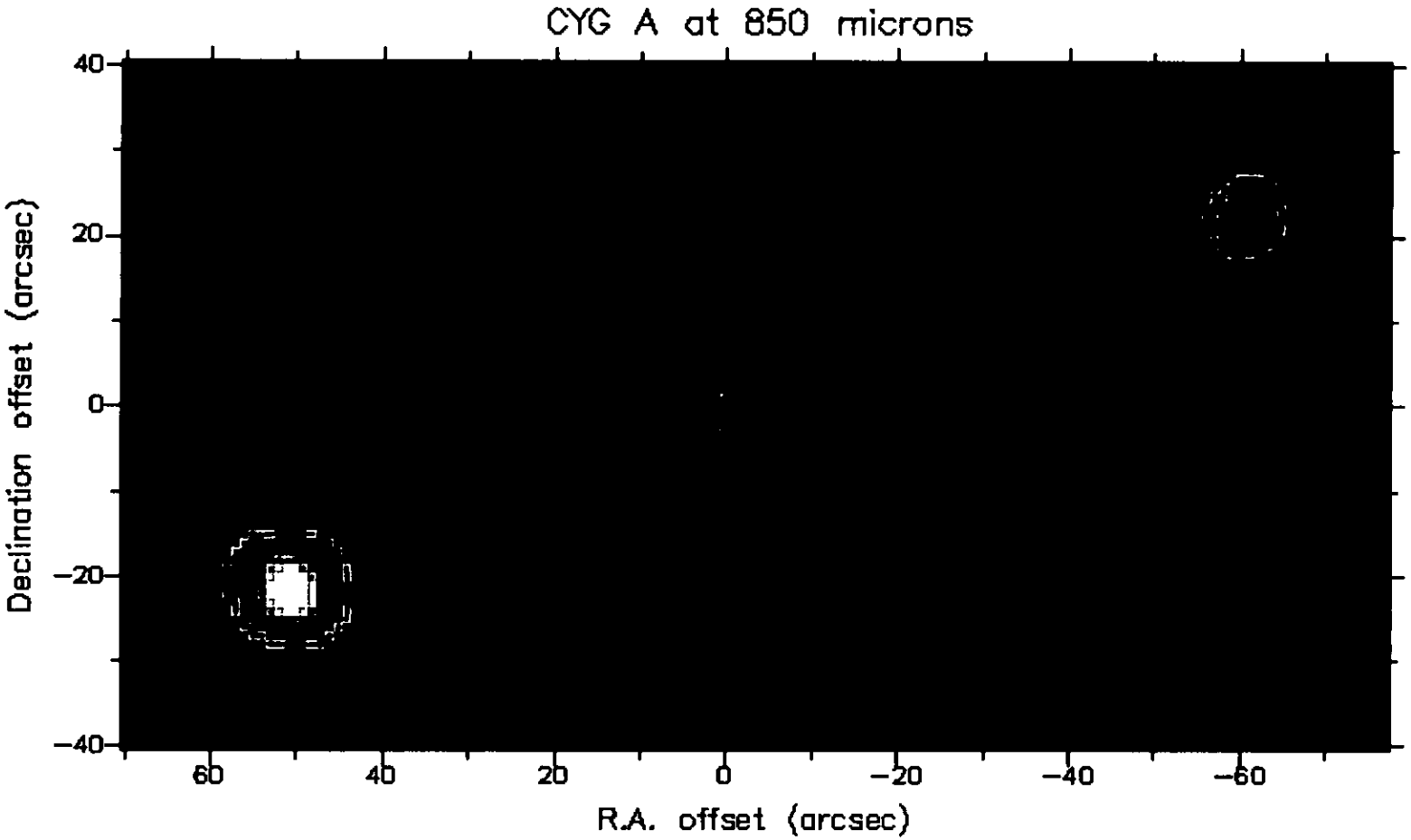

Figure 3.1: The hotspots and central core of Cygnus A at 850 μm.

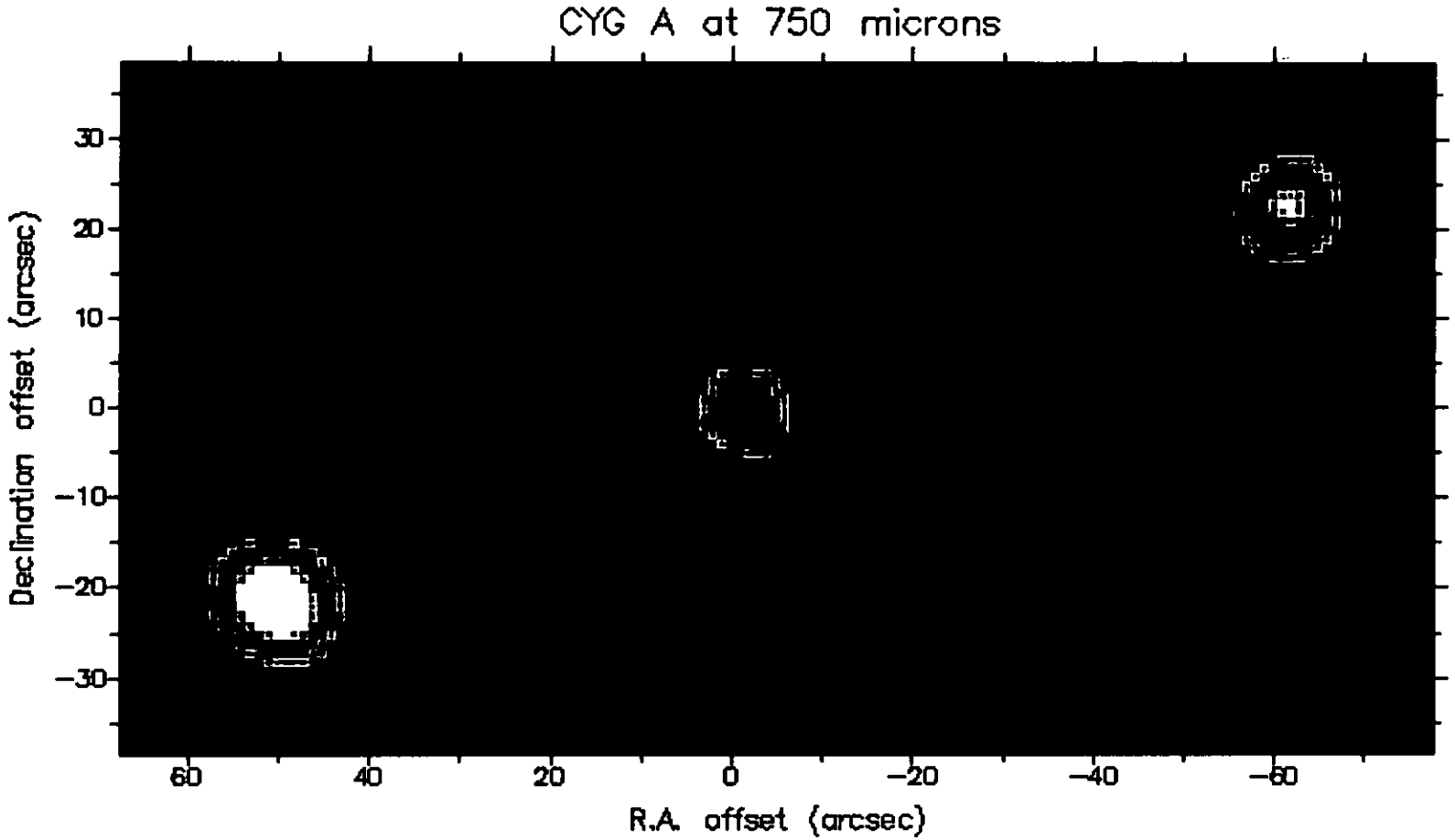

Figure 3.2: The hotspots and central core of Cygnus A at 750 μm.

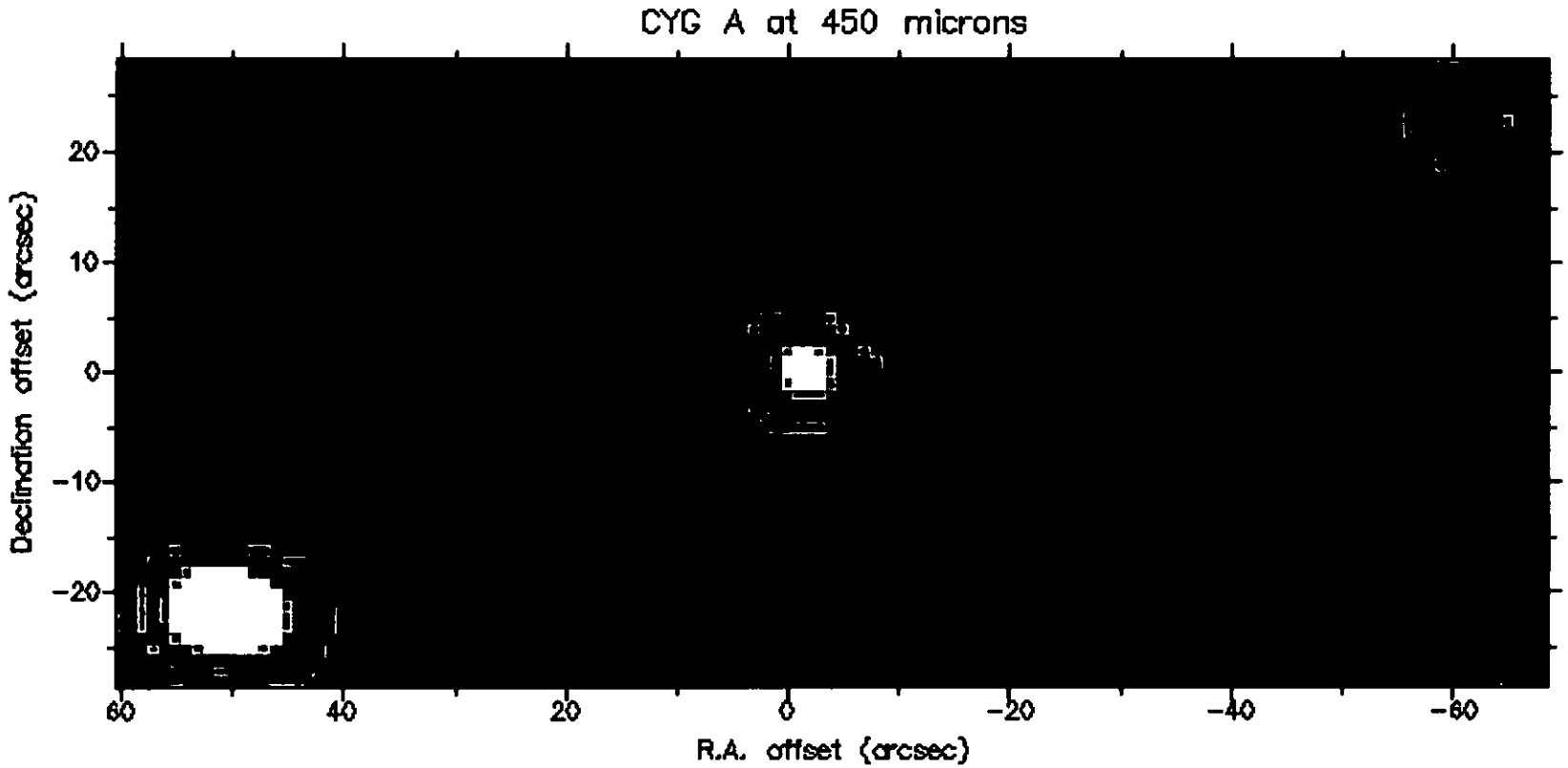

Figure 3.3: The hotspots and central core of Cygnus A at 450 μm.

3.3 Results and Discussion

The 850, 750, and 450 μm SCUBA images, respectively, in Figure 3.1, 3.2, and 3.2 clearly show the two hotspots and the central core of the galaxy. The rms uncertainties on the maps are 40, 50 and 85 mJy respectively. No detections were made at 350 μm and a 430 mJy rms was determined from the map (not shown).

3.3.1 The Hotspots

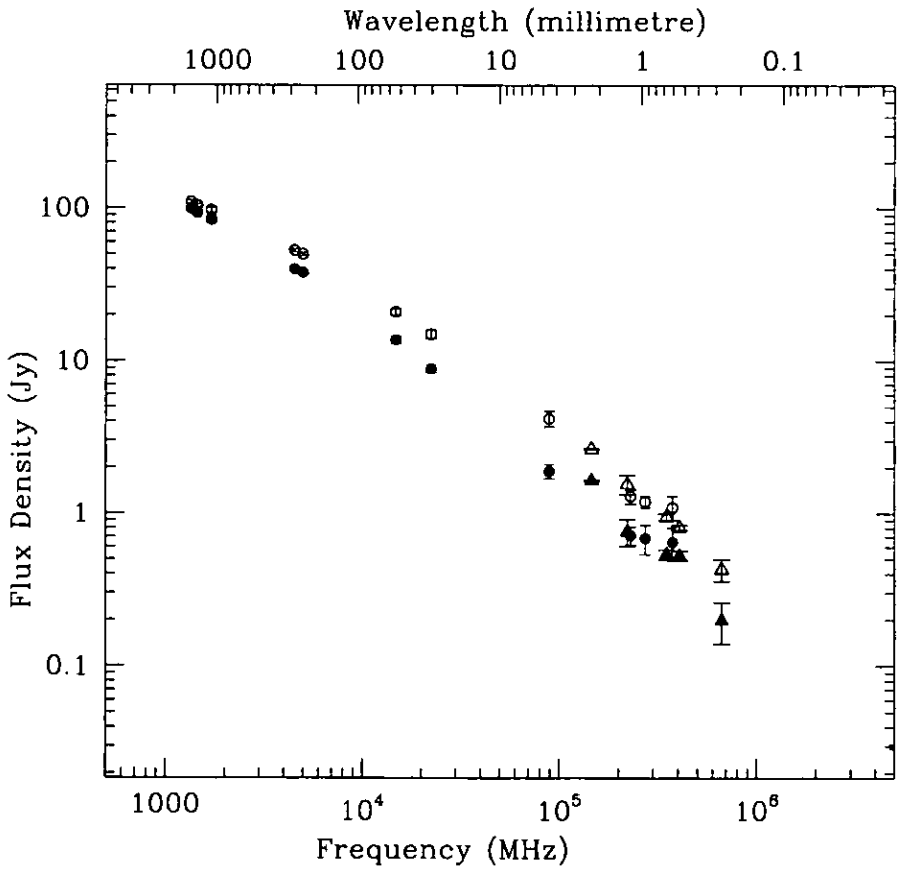

Figure 3.4: The spectral energy distribution of the hotspots A (open circles) and D (solid circles) in Cygnus A. The SCUBA data points are indicated by triangles.

The spectral energy distribution of the two hotspots is shown in Figure 3.4. The SCUBA data points are indicated by open (hotspot A) and solid (hotspot D) triangles; the other

data points are taken from Carilli et al. (1991) and they are indicated by open (hotspot A) and solid (hotspot D) circles. The points at 375 GHz (800 μm) are from Eales et al. (1989) and are also from the JCMT using the previous single-pixel continuum instrument, UKT14.

The well observed radio synchrotron spectrum is seen to continue smoothly into the submm region with no apparent spectral break. The spectral indices, α, determined from 146 to 667 GHz, are $\alpha = -1.04 \pm 0.01$ for hotspot A (NW) and $\alpha = -0.99 \pm 0.01$ for hot-spot D (SE). In all cases $S_\nu \propto \nu^\alpha$. There is no significant evidence for further spectral steepening due to a high energy cut-off in the electron distribution. The excellent determination of an index of close to -1.0 fits extremely well with the continuous injection of relativistic electrons in the hotspots (Carilli et al., 1998). The spectral index of the injected electrons of -0.5 gives support to the origin of the high energy electrons in a shock (Bell, 1978).

If an equipartition value for the magnetic field in the hotspots of 30 nT (Wright & Birkinshaw, 1984) is taken, the electrons radiating at 800 GHz have an energy of around 2×10^{10} eV and a synchrotron radiative lifetime of 6.6×10^3 years. For a single central source of the electron acceleration in each hotspot and an electron diffusion rate of the speed of light, the electrons responsible for the 800 GHz synchrotron radiation can, at most, travel a radial distance of 2 kpc. Interferometer measurements at 89 GHz (Wright & Birkinshaw, 1984) reveal that the hotspots are spatially resolved and are between 2 and 3 kpc in size. Therefore if the hotspots are the same size at 800 GHz, there is barely adequate time for the highest energy electrons to fill the volume even with a diffusion speed of order c. If the speed is substantially less than c, then multiple acceleration sources (shocks) are required in order to explain the observations. In fact, the spectral

index distribution determined from recent high-resolution VLA imaging observations at 30 GHz suggests that distributed particle acceleration occurs in the hot spots (Carilli et al., 1999). To test this hypothesis further requires better determination of the magnetic field and interferometer measurements at 800 GHz. These will be possible with the introduction of the Smithsonian Submillimeter Array (Moran, 1996), that is now under commissioning on Mauna Kea, Hawaii.

3.3.2 The Core Component

A power-law spectral index of $\alpha = -0.6 \pm 0.1$ has been determined between 146 and 677 GHz for the core. This is much steeper than $\alpha \approx -0.1$ determined by Wright & Birkinshaw (1984) and Salter et al. (1989) respectively between 10 and 89 GHz and 89 and 230 GHz. Indeed, given the quality of the data it is not clear whether a power law (rather than a smoothly curving function) is, in fact, the best fit to the data. On the other hand, in the unification scenario we suspect the radio-core of Cygnus A to be a severely misaligned jet and therefore the spectrum to be typical of an unboosted blazar jet spectrum. These have been observed in the mm to submm (Gear et al., 1984), so it is assumed that a power-law is the simplest interpretation. In this case there is tentative evidence for some steepening above 600 GHz, but the data are inadequate to determine whether this is the 0.5 break of a continuous injection model, or, whether it is the onset of depletion of high energy electrons. Further observations at the high frequency submm wavelengths are needed to answer this question.

The *IRAS* measurements clearly suggest thermal emission from dust in the central galaxy, although the temperature and hence mass of the emitting dust are very uncertain from the *IRAS* values alone. The new submm data points constrain the non-thermal con-

tribution to the *IRAS* and the new *ISO* fluxes. In particular the 667 GHz measurement constrains the temperature of emitting dust to within a factor of two.

3.3.3 Cold Dust in Cygnus A

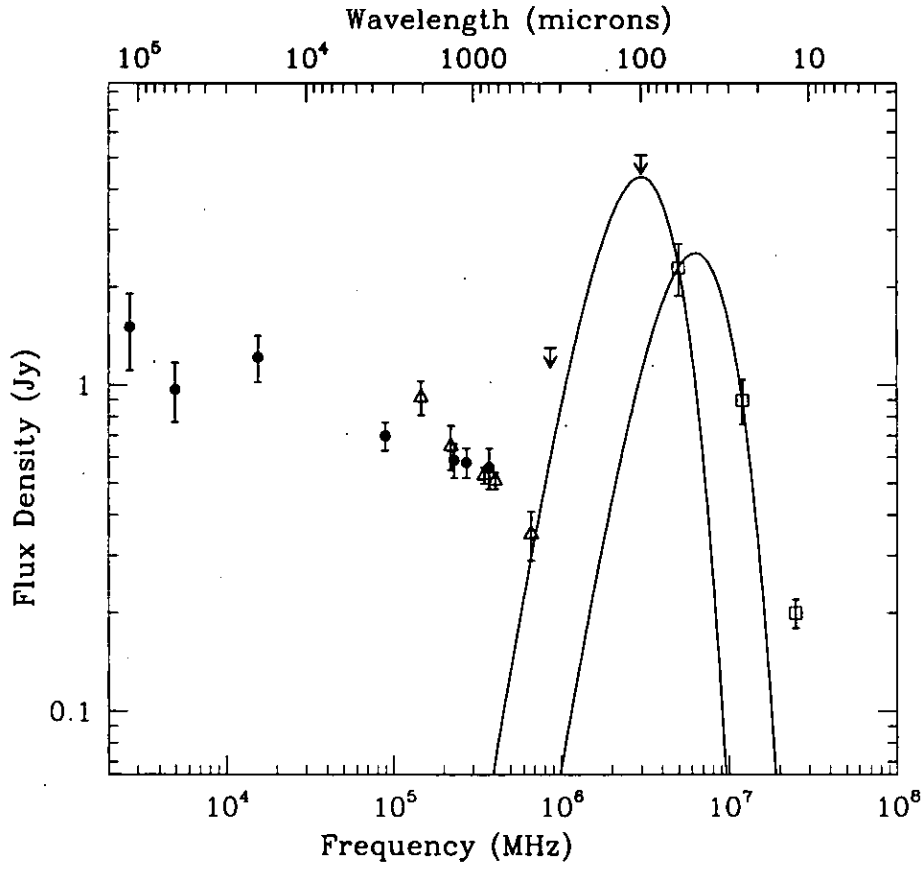

Figure 3.5: The spectral energy distribution of the central core in Cygnus A. The SCUBA data points are indicated by open triangles. The upper limits are both 3σ; the 350 μm is from SCUBA and the 100 μm is from reprocessed *IRAS* data. The two curves represent emission from greybodies with temperatures of 37 and 85 K with an emissivity index, β, of 1.3.

Assuming a reasonable value for the dust emissivity index, β, of 1.3, the maximum temperature that appears to fit the *IRAS* data is 85 K, while the lower temperature is constrained by the SCUBA measurement at 450μm to 37 K. Figure 3.5 shows both these temperatures. Changing β between 2.0 and 1.0 makes very little difference to the

derived temperatures. The mass of emitting dust $M_{\rm d}$ is derived as in Section 1.3.1. It is assumed that values of the grain mass absorption coefficient are $k_{\rm d}^{450\,\mu{\rm m}} = 0.25\,{\rm m^2 kg^{-1}}$ and $k_{\rm d}^{60\,\mu{\rm m}} = 3.3\,{\rm m^2 kg^{-1}}$ (c.f. Section 1.3.1), which yield dust masses of $1.0 \times 10^8 M_\odot$ for T = 37 K and $1.4 \times 10^6 M_\odot$ for T = 85 K.

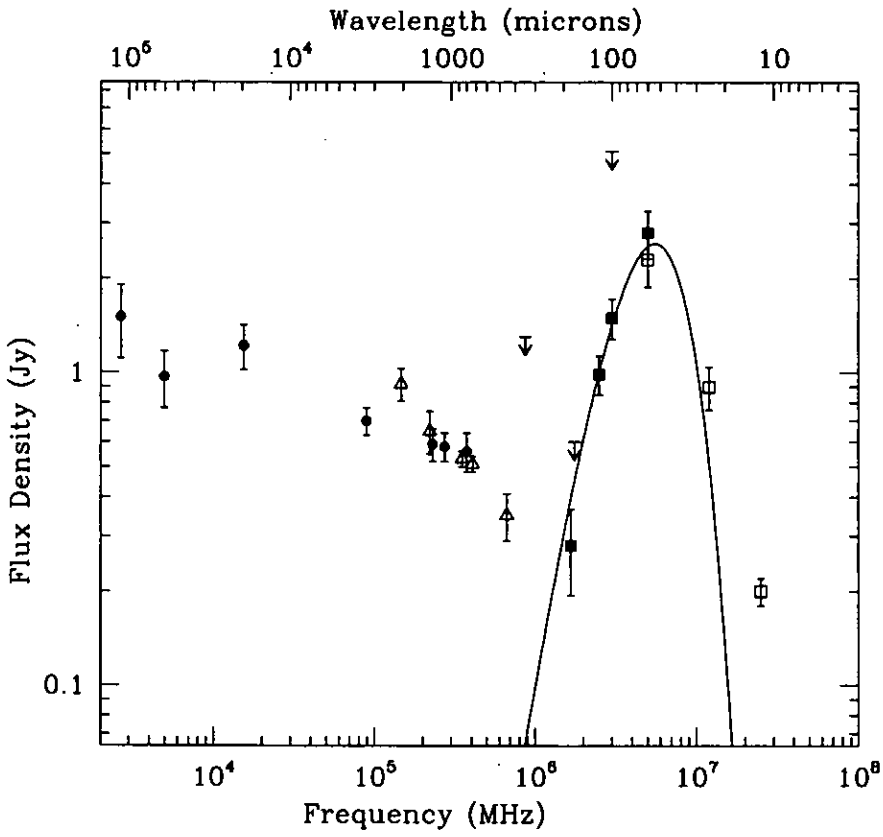

Figure 3.6: The spectral energy distribution of the central core in Cygnus A that includes recent *ISO* observations by Haas et al. (1998). The data points are as in Figure 3.5 plus the new *ISO* fluxes at 60, 120, 170 and 180 μm marked by solid squares. The upper limits are the 3σ determinations at 350, 170 and 100 μm from SCUBA, *ISO* and *IRAS* respectively.

Using recent *ISO* data at 60, 120, 170 and 180 μm (Haas et al., 1998), which sample the critical part of the spectrum, the dust temperature can be better-constrained. Consistent with the above results, the *IRAS* and *ISO* data are fit by a greybody function with the temperature of 70 K and emissivity index of 1.3, that is shown in Figure 3.6. Also

consistent with the above results, (Haas et al., 1998) fit a slightly cooler dust spectrum of temperature 52 K to their *ISO* data, yielding a dust mass of $5 \times 10^6 M_\odot$.

For the starburst galaxy M 82, Hughes et al. (1994) estimated the dust mass within the inner 1 kpc of the nucleus to be between $1.8 \times 10^6 M_\odot$ and $3.6 \times 10^6 M_\odot$ for T= 48 K and T= 30 K respectively. The minimum estimated 85 to 52 K dust masses in Cygnus A are remarkably close to this, and, though only a tantalising hint, suggests Cygnus A core properties are similar to those of classical nuclear starburst galaxies. However, the submm upper limit to the dust mass for Cygnus A is considerably higher than the dust mass in M 82, even when considering the mass contribution seen in the low brightness flux outside the inner 1kpc of the nucleus, which is measured to be about 30% of the nuclear mass (Alton et al., 1999). From these deep images of the extended dust emission in M 82 (c.f., Chapter 6 and Alton et al., 1999), it can safely be said that if M 82 were moved to the distance of Cygnus A, the emission would be unresolved in the SCUBA beams. The recently obtained deep SCUBA images of the star forming galaxy Arp 220 (at 76 Mpc) are also unresolved.

The upper limit for the dust mass in Cygnus A obtained from the submm data is comparable to the dust masses for Arp 220 and another star forming galaxy NGC 6240, which are $4.5 \times 10^7 M_\odot$ and $3.0 \times 10^7 M_\odot$ respectively (Klaas et al., 1997). The comparison is interesting because, from unusually luminous hot molecular gas emission (1.0×10^{34} W), Ward et al. (1991) likened the core of Cygnus A to Arp 220 and NGC 6240. At the same time, Ward et al. (1991) noted that the implied mass of the hot molecular gas led to a mass ratio upper limit of hot-cold H_2 that was not unusual in AGN. It is noted that while the lower and upper dust mass limits for Cygnus A are, respectively, comparable to the nuclear starburst galaxies M 82 and the extranuclear starburst galaxies Arp 220

and NGC 6240, the upper dust mass limit is also similar to the masses for the Radio Quiet Quasars IZw 1, Mrk 1014 and Mrk 376, which are $7.6 \times 10^7 M_\odot$, $6.3 \times 10^8 M_\odot$ and $5.8 \times 10^7 M_\odot$ respectively (Hughes et al., 1993).

3.4 Summary

Detailed photometric and imaging observations of the two hotspots and the radio core of Cygnus A have been made. The spectral index of the hotspots extends smoothly to about 450μm (677 GHz) with no evidence of spectral steepening. If the diffusion speed for the electrons responsible for this emission is about c, then a single particle acceleration mechanism can be responsible for the hotspot synchrotron emission. On the other hand, if the diffusion speed is significantly less than c, then multiple acceleration locations are probably required unless the magnetic field strength is significantly less than the equipartition value. Future observations using submm interferometers should narrow-down the parameter space in terms of the size of the emitting region.

The radio core has a much flatter spectral index, more indicative of a relativistic jet, and as such could be the standing shock at the entrance of the parsec-scale jet. There is some evidence for spectral steepening, perhaps suggesting that at these energies, the lifetime of the radiating particles is sufficiently short that there is inadequate replenishment available. There is no evidence for thermal emission from dust at the highest frequency of 667 GHz (450μm) and this, along with re-reduced *IRAS* data, restricts the temperature of the emitting dust to between 37 and 85 K, with corresponding dust masses of $1.0 \times 10^8 M_\odot$ and $1.4 \times 10^6 M_\odot$. These results are consistent with very recent and better-constrained dust temperature of 52 to 70 K and dust mass of about $5 \times 10^6 M_\odot$ (cf. Haas et al., 1998), obtained using new *ISO* data at 60 through 180 μm. The lower dust mass

limit of $\sim 10^6 M_\odot$ is comparable to the nuclear starburst galaxy M 82 and the upper limit to the extranuclear starburst galaxies Arp 220 and NGC 6240 as well as the Radio Quiet Quasars IZw 1, Mrk 1014 and Mrk 376. It is unclear whether the heating of warm dust in Cygnus A is dominated by the active star formation or galactic nucleus.

Chapter 4

SCUBA Observations of the Elliptical Galaxy NGC 4374

4.1 Introduction

The interstellar medium (ISM) in elliptical galaxies is not easily probed by optical observations; however, observations at a range of other wavelengths have revealed unexpected amounts of gas in these galaxies (e.g. Roberts et al., 1991). With the gas, it is also expected that dust will be present since red giant stars lose dust to the ISM. Small amounts of dust are seen in dust lanes and patches in ellipticals (Sparks et al., 1985; Goudfrooij et al., 1994). SCUBA provides an opportunity to test if there is cold (less than about 30 K), diffusely distributed dust present in elliptical galaxies as suggested from far-infrared observations and from *IRAS* observations for a sample of ellipticals by Goudfrooij & de Jong (1995). They estimated dust temperatures of 25 to 35 K and dust masses of $\sim 10^4$ to few $\times 10^6 M_\odot$, which indicated that dust masses derived from *IRAS* fluxes exceeded the dust masses estimated from optically identified dust lanes and

patches in many ellipticals, by typically an order of magnitude.

However, the *IRAS* data are limited for studying dust since *IRAS* gave little information about the spatial distribution of the dust in galaxies, so cannot be used to check directly if the dust is diffusely distributed or not. It can also be noted that many ellipticals contain haloes of hot gas at around 10^7 K with masses of a few $\times 10^9 M_\odot$ (Canizares et al., 1987). This X-ray emitting plasma is expected to destroy any dust grains through sputtering by hot gas particles in a short time ($< 10^7$ years (Draine & Salpeter, 1979)). So, for diffusely distributed dust to be present in a typical giant elliptical galaxy, the dust would have to be protected or shielded from the plasma in some way. SCUBA, being an imaging device, offers an opportunity to map out the distribution of any cool dust.

The giant elliptical NGC4374 was chosen from the sample of Goudfrooij & de Jong (1995) as a candidate in which to look for diffusely distributed dust because it has optical dust lanes in the central region ($< 10''$). The dust mass estimated from the dust lanes is $3.5 \times 10^4 M_\odot$ and the dust mass estimated from the infrared (*IRAS*) fluxes (at 60 and 100 μm) is $1.35 \times 10^5 M_\odot$ (for a dust temperature of 35 K), a factor of ~ 4 greater than from the optically identified dust (Goudfrooij & de Jong, 1995).[1] Since most of this dust is not seen in the optical dust lanes, Goudfrooij & de Jong (1995) suggest that it must be diffusely distributed throughout the galaxy. Such dust would affect the colours in galaxies. However, this effect could be difficult to disentangle from age and metallicity variations in the stellar population, which also produce colour changes (Worthey, 1994). Therefore, the presence of a few million solar masses of dust, distributed throughout a galaxy, could well have escaped optical detection. On the other hand, spatially resolved

[1]Note that there was a typographical error by Goudfrooij & de Jong (1995): the dust mass they estimated from the *IRAS* data should have read LogM_d=5.13 (not 5.3) (Goudfrooij - private communication). The correct dust mass is quoted here.

tometry at 2000, 1350, 850 and 450 μm can confirm the presence of diffusely distributed, cold dust in the giant elliptical galaxy NGC 4374. The SCUBA observations together with radio and infrared data from the literature are used to place tighter constraints on the spectral components, including the dust temperature and the size of the infrared emitting region.

4.2 Observations and Reductions

Imaging and photometric observations of NGC 4374 were obtained on 1997 September 3 as well as 1998 January 22, February 1, February 14 and 1999 March 19, with SCUBA (see Table 4.1). The imaging observations used the short wave array (SW) at 450 μm and the long wave array (LW) at 850 μm, with beam-widths of 8".5 and 14".5 (FWHM) respectively. The observations employed a 64-point jiggle pattern, fully sampling the 2'.3 field of view of both arrays. Similarly, the submm photometric observations were obtained by operating the central bolometers of the SW and LW arrays at 450 and 850μm simultaneously, employing a 9-point jiggle pattern in a 3 by 3 grid of 2". The 1350 and 2000 μm observations used the single photometry bolometers and also employed a 9-point jiggle pattern.

Standard SCUBA data reduction was undertaken (see Chapter 2). The fluxes were calibrated using instrumental gains that were determined from beam-maps of Mars or Uranus nightly and in the same observation mode as the target observation (see Table 4.1). Planetary fluxes for each filter were obtained using the JCMT utility program FLUXES. During the January and February 1998 runs, the planets were not available and the JCMT secondary calibrators CRL 2688 and IRC+10216 were used (Sandell, 1994, 1998). On nights when the $\tau_{\rm CSO} > 0.07$ (see above and Table 4.1), the atmosphere was

Table 4.1: Submillimetre fluxes (Janskys) for NGC 4374 from SCUBA

UT Date	2000 μm 146 GHz	1350 μm 221 GHz	850 μm 350 GHz	450 μm 677 GHz	850/450 μm 350/677 GHz Total Int. Time (s)	Obs Mode	τ_{CSO}	Calibrators
'990319	0.15 ± 0.02		0.18 ± 0.02	0.11 ± 0.02	2160	Phot	0.06	Mars
'980214	0.15 ± 0.02	0.15 ± 0.02	0.11 ± 0.02	< 0.15	1260	Phot	0.05	CRL2688
'980201			0.15 ± 0.02	< 0.12	2640	Map	0.05	IRC+10216
'980122		0.14 ± 0.02	0.13 ± 0.02	< 0.12	2340	Map	0.04	IRC+10216
'970703			0.16 ± 0.03		2220	Map	0.1	Uranus

opaque to 450μm emission and observations could be made only at longer wavelengths.

4.3 Results and Discussion

Figure 4.1 shows the 850 μm image of NGC 4374 together with the beam-width determined from observations of 3C 273, a standard point source for the JCMT, made in the same way and conditions as NGC 4374. The rms uncertainty on the map is less than 20 mJy/beam. The image of NGC 4374 has small northeastern and southwestern spurs that are not real features of the galaxy but a manifestation of the beam smearing as a result of chopping. These spurs are in the chop direction and are detected at a much lower level than the central emission. An examination of the point spread function of the NGC 4374 image yielded $\mathrm{FWHM_{minor-axis}} = 15''.0$ and $\mathrm{FWHM_{major-axis}} = 15''.7$. The result shows that the image of NGC 4374 is no more than $1''$ greater than the JCMT beam. This insignificant spatial extension is probably a result of a small pointing drift during the long observation ($\sim$ 1hr). Thus, NGC 4374 is not extended in the SCUBA 850μm image, which constrains the spatial origin of the observed emission to less than $15''$ (1.5 kpc for a distance of 20.74 Mpc) in diameter. It is worth noting that although the SCUBA beam is $\sim 15''$ at 850 μm, the arrays have a $2'.3$ field of view, and therefore, at the distance of NGC 4374, any diffuse emission to $\sim$ 13 kpc in extent is not detected,

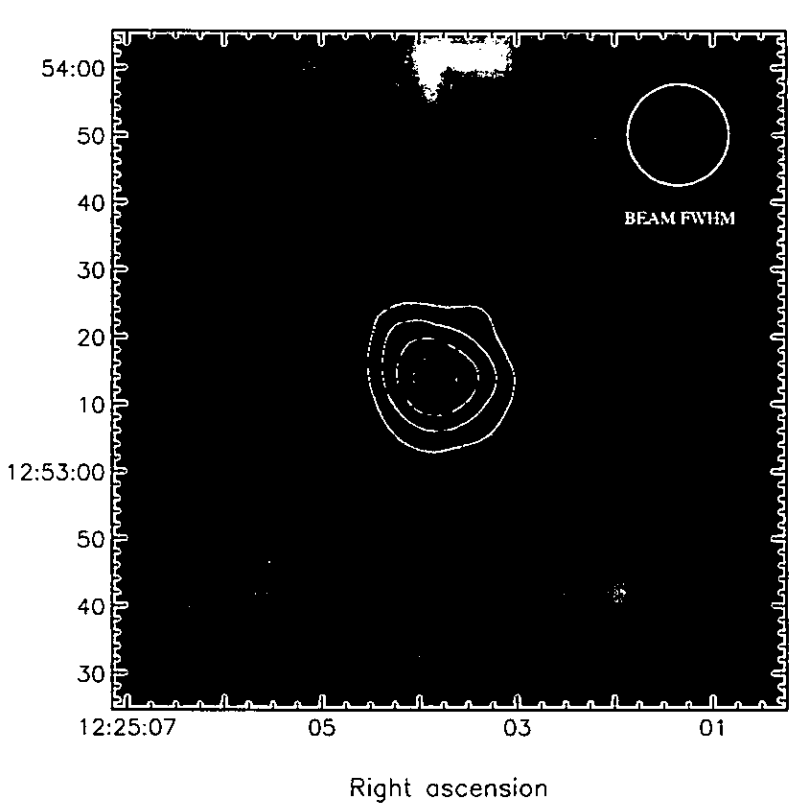

Figure 4.1: The SCUBA 850 μm image of NGC4374. The observation was made on 1998 February 1 when τ_{CSO} was ~ 0.05.

as the observations were made with the array pointed at the centre of the galaxy and were sensitive to the entire field of view of SCUBA. The 3σ upper limit on the 850 μm integrated flux within a region of about $2'$ diameter, just less than the SCUBA array, is ~ 0.6 Jy, giving the flux density upper-limits on the undetected low, level diffuse dust.

The results from the imaging and photometric observations are shown in Table 4.1. The uncertainties are a quadratic sum of the uncertainty arising from the measured signal-to-noise-ratio and a systematic calibration uncertainty, which varies from 10% at 850 μm and lower, to 27% at 450 μm. The 450 μm fluxes listed for the 1998 Feb 01 and 14 and Jan 22 runs are 3σ upper limits. The submillimetre flux variation over the four observing runs was within the uncertainties on the fluxes.

4.3.1 Decomposing the SED

Figure 4.2 shows the spectral energy distribution (SED) for NGC 4374, including data from radio (Jenkins et al., 1977) to infrared (*IRAS*) wavelengths. The infrared fluxes were obtained from NED (the NASA/IPAC Extragalactic Database) and have been interpreted as thermal emission from dust (Knapp & Patten, 1991; Goudfrooij, 1994). At longer radio wavelengths, the lobes dominate the integrated flux from NGC 4374 (by a factor of 8 at 5 GHz (Wrobel, 1991)) and give an excellent power-law of spectral index ($S_\nu \propto \nu^\alpha$) of $\alpha_{31\,\mathrm{GHz}}^{2.7\,\mathrm{GHz}} = -0.6 \pm 0.03$, as shown by the dotted line in Figure 4.2. This spectral index is consistent with the classification of NGC 4374 as a steep spectrum radio galaxy. The good fit suggests variability larger than the errors on the fluxes is uncommon for the synchrotron power-law of the radio emission.

The submm data points for fluxes within the SCUBA beam and previous submm measurements fall below an extrapolation of this steep radio power-law from the integrated flux. No sign of extended emission from the radio lobes is visible on any of the maps, and the 3σ upper limit on the 850 μm integrated flux within a region approximately the size of the lobes is ~ 0.6 Jy. This is much higher than the extrapolation of the radio power-law from the integrated fluxes, showing that the observations are insensitive to the radio lobes (Figure 4.1). As is shown later, this indicates that if the observed SCUBA 850 μm emission is non-thermal in nature, it is dominated by the compact core (or inner-jet).

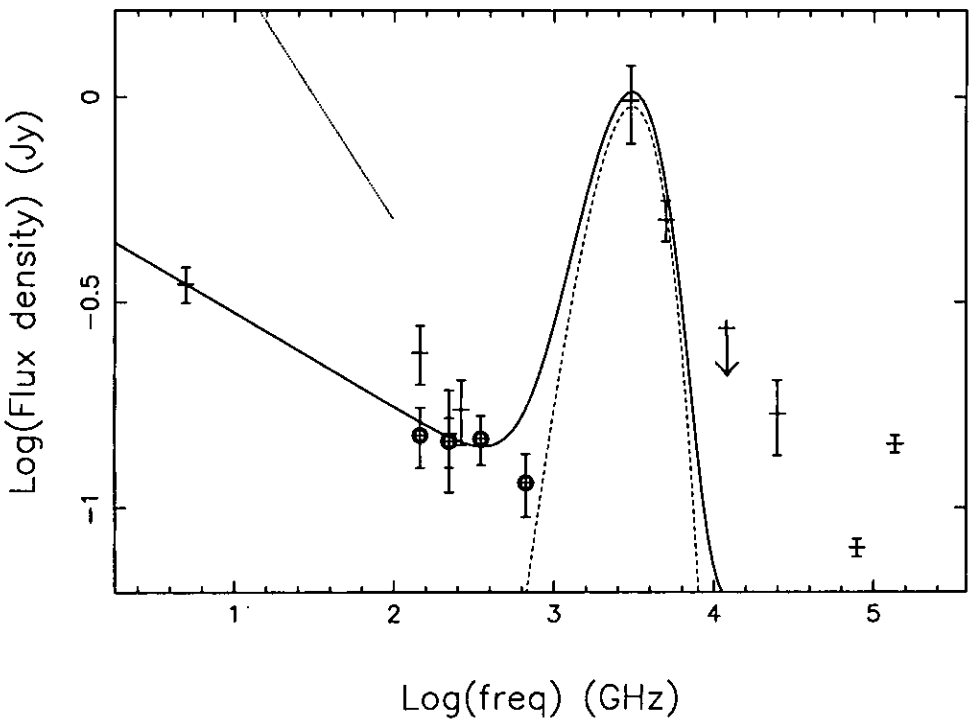

Figure 4.2: Spectral energy distribution from radio to infrared for the core of the elliptical galaxy NGC4374. Filled circles are the SCUBA data and the sources of other data are described in the text. The solid line is a composite model of a power-law ($\alpha = -0.23$) plus (35 K) greybody (Leeuw et al., 2000). This model fits the data quite well for the radio through to 60μm infrared detections. The dashed line shows the 35K greybody alone, showing that the SCUBA data lie above this component. The dotted line is a power law of slope -0.6, passing through the integrated radio fluxes to 31 GHz. The downward arrow indicates a 3 sigma upper limit at 25μm.

The Core SED

In Figure 4.2, the single available core-radio flux for NGC 4374 at 5GHz (Jenkins et al., 1977; Wrobel, 1991) is plotted; the circles are the means of the SCUBA data listed in Table 4.1. The 5 GHz core flux together with the SCUBA data give a power-law slope of $\alpha = -0.23 \pm 0.03$. In compact radio galaxies, such flat spectra have been found to comprise spectra from many unresolved components, each with its own synchrotron spectrum, the sum of which results in the observed flat power-law. Although there is only one radio-core point and the SCUBA data, the observed flatter power-law of the NGC 4374 core could be a consequence of such unresolved synchrotron components; but, with the current data, this is only a suggestion rather than anything stronger at this stage. At 5GHz, the northern jet in NGC 4374 is brighter than the southern jet for the first 10″ (Bridle & Perley, 1984); this one-sided inner-jet may comprise such unresolved components.

It is worth noting that the SCUBA fluxes at 850, 1350 and 2000 μm alone give a spectral index of $\alpha^{350\,\mathrm{GHz}}_{146\,\mathrm{GHz}} = -0.16 \pm 0.32$ in the submm, forming a flat spectrum resembling that of a free-free emission component (or is characteristic of low-luminosity blazars; see below and Section 5.7). While this 2000 to 850 μm spectral index is consistent with that of free-free emission ($\alpha = -0.1$), the large uncertainty on its value limits the ability to prove conclusively its origin. The SCUBA 450 μm data-point lies well below this $\alpha = -0.16$ spectrum, which does not help to prove or disprove its origin, but instead adds the complication that this free-free component might have a high-frequency cut-off between 850 and 450 μm. In steep spectrum radio galaxies such as NGC 4374, it is uncharacteristic for a free-free component to dominate the power-law in the mm-submm wavelength range (e.g. Gear et al., 1985). Therefore, if this component is real it would

have to come from very high ionization and it would be an interesting discovery. To explore this further, the 'submm flat-spectrum component' in Figure 4.2 was crossed correlated with the well known spectrum of 3C 273, using data taken with SCUBA on 1998 February 15, just one night after and under very similar conditions as the photometry observations of NGC 4374. The spectrum of 3C 273 gives a much steeper slope and a spectral index of $\alpha_{146\,\mathrm{GHz}}^{350\,\mathrm{GHz}} = -0.7 \pm 0.1$, as expected of this variable object during its quiescent phase (Robson et al., 1993). Therefore, with the current limited data, it is not possible to say if the 850, 1350 and 2000 μm fluxes come from significant free-free emission, if there is any at all.

In the case of Centaurus A, a low-luminosity FR I radio galaxy like NGC 4374, Hawarden et al. (1993) and Kellermann et al. (1997) determined a very flat nuclear mm-to-submm spectrum in the core, which they attributed to a low-luminosity blazar (see Chapter 5). In terms of the blazar/FR I unification scheme of AGN, a misaligned blazar in the core is consistent with the FR I morphology that is seen in large-scale radio maps of NGC 4374 and Centaurus A. While a very flat spectral index is also consistent with free-free emission ($\alpha = -0.1$) from ionised gas in star-formation regions, high resolution VLBA observations of Centaurus A by Kellermann et al. (1997) set lower limits of 10^{10} K on the core brightness temperature, thus excluding free-free emission from star-formation as a possible contributing factor. Therefore, if the core of NGC 4374 is as compact as in Centaurus A and has similar brightness temperature, free-free submm emission may indeed be highly unlikely in this case too. Furthermore, if indeed the submm core spectrum of NGC 4374 is flat as the observations indicate, the results would, more plausibly, support the hypothesis that *flat* spectra are a characteristic of low-luminosity blazars (see Section 5.7). Submm observations of a larger sample of low-luminosity blazars are

needed to provide a more definitive test.

To model the radio to infrared SED, a combination of a power-law (non-thermal radio emission from the active nucleus) plus greybody (re-processed emission from dust (Hughes et al., 1994)) was used.[2] The composite model flux is

$$F_\nu = C\nu^{-\alpha} + \Omega B_\nu(T)[1 - \exp(-(\frac{\lambda_o}{\lambda})^\beta)]. \quad (4.1)$$

In equation (4.1), C is the normalisation for the power-law component, α the power-law spectral slope, Ω the solid angle for the greybody component, $B_\nu(T)$ the Planck function at temperature T, λ_o the wavelength at which the optical depth is unity and β the emissivity index of the grains. The normalisation factors (C and Ω) are obtained by forcing the model to agree with the 5 GHz core-radio and IR (60 and 100 μm) fluxes respectively, since the two components dominate in these different wavebands. The power-law index and its uncertainty were estimated from linear regression fits to the core-radio plus SCUBA data in a log-log plot. It is assumed that the *IRAS* emission comes from a region less than $\sim 10''$ due to lack of extension seen at 450 μm. The best fit temperature and its uncertainty for the greybody component were estimated by eye from plots of the composite model versus the data. Other parameter values ($\lambda_o = 7.9\,\mu$m and $\beta = 1.3 \pm 0.5$) were fixed at the values given by Hughes et al. (1994) in their study of M 82. The parameter values determined from the model are summarised in Table 4.2, and the model is plotted as a solid line in Figure 4.2. The greybody fit demands that the warm dust emission comes from a very compact zone, much smaller than the SCUBA 450 μm resolution (see Table 4.2). The simplest explanation for the 450 μm data point lying below the sum of

[2]The composite model was constructed by Anne Sansom in collaboration with L. L. Leeuw and E.I. Robson for a paper presented by Leeuw et al. (2000).

the thermal and non-thermal emission (see Figure 4.2) is that the synchrotron spectrum steepens between 850 and 450 μm (or somewhat longward of 850 μm, given the uncertainties). Some small part of the 450 μm emission could be due to low surface brightness dust of $\sim$ 15 to 20 K. Better spectral coverage and higher signal-to-noise data in the submm are clearly needed to test more complex spectral models.

Table 4.2: Parameters determined from the model fit to the SED for NGC 4374

Parameter	Value	Uncertainties	Units
α	-0.23	$\pm$0.03	-
Ω	3.96E-11	-	steradians
	1.46	-	arcseconds
T	35	$\pm$5	K

4.3.2 Dust Mass and its Implications

The temperature that fits the *IRAS* data and is constrained by the SCUBA 450 μm measurement is $\sim 35\pm5$ K (see Figure 4.2). Not surprisingly, this is the same temperature as Goudfrooij (1994) found for this galaxy from his analysis of the *IRAS* data alone. Changing β between 2.0 and 1.0 makes very little difference to the best fit temperature. The mass of the emitting dust $M_{\rm d}$ is derived as in Section 1.3.1. Using the distance of 20.74 Mpc for NGC 4374, as assumed by Goudfrooij (1994), and the grain mass absorption coefficient of $k_{\rm d}^{100\,\mu{\rm m}} = 2.5\,{\rm m^2 kg^{-1}}$ (Hildebrand, 1983), a dust mass is estimated of $1.2\times 10^5 {\rm M}_\odot$ for $S_{100\,\mu{\rm m}} = 0.98\pm0.21$ Jy and $T = 35$ K. The dust mass calculated for NGC 4374 is about the same as Goudfrooij & de Jong (1995), as expected since they used the same temperature. Furthermore, it is similar to that found in a recent *HST* $(V-I)$ study of the dust lane in NGC 4374 by Bower et al. (1997), who found the dust mass to be in agreement with that derived from *IRAS* data, in contrast with the dust *deficit* found in

other optical studies of ellipticals (Goudfrooij & de Jong, 1995). However, for NGC 4374 this is at least one order of magnitude lower than Knapp & Patten (1991), who assumed a cooler temperature of 18 K (based on objects in their sample of nearby radio galaxies for which 1350, 800 and 450 μm fluxes were detected). Also, they obtained the higher mass even though they assumed a smaller distance of 13 Mpc. While the low dust temperatures (15 to 20 K) estimated by Knapp & Patten (1991) are similar to the Galactic Plane value of $T = 19$ K, they are inconsistent with the SCUBA plus *IRAS* observations of NGC 4374 if the dust is assumed to be all a single temperature of 35 K (Goudfrooij, 1994; Leeuw et al., 2000).

As for the extended radio-lobe emission, the extended low-level emission from diffusely distributed dust was not detected with SCUBA. The 2000 to 850 μm data from the central region of the galaxy are most unlikely due to diffuse cold dust, but some small part of the 450 μm emission could be due to dust of $\sim$ 15 to 20 K. Also, the 3σ upper limit to the surface brightness at 450 μm is too high and not useful for setting dust mass upper limits on this possibly colder dust. Deeper SCUBA imaging observations are clearly needed to address this question.

A very rough dust mass limit is estimated for the diffuse dust using the 3σ upper limit of $\sim$ 0.6 Jy on the 850 μm integrated flux within a region of about $2'$ (13 kpc of the galaxy) diameter, which is the flux density upper limit on the undetected low, level diffuse dust as well as the extended radio-lobe emission (c.f. Section 4.3.1). Assuming the distance of 20.74 Mpc for NGC 4374, as above, and the grain mass absorption coefficient of $k_{\rm d}^{850\,\mu{\rm m}} = 0.15\,{\rm m^2 kg^{-1}}$ (Hildebrand, 1983), a dust mass is determined of $3.6 \times 10^7 {\rm M}_\odot$ and $1.2 \times 10^7 {\rm M}_\odot$ for cold dust of $T = 12$ (as estimated by Leeuw et al. (2002) in Centaurus A) and 18 K (as assumed by Knapp et al. (1990) and is similar to the Galactic Plane value)

respectively. These mass limits for cold, diffuse dust are about two orders of magnitude higher than calculated assuming the dust in NGC4374 is all at a single temperature of 35 K (Leeuw et al., 2000). It is noted that the mass limits are of the order of the dust contents in luminous spiral galaxies ($\sim 10^6$ to $10^8 M_\odot$). Saying any more at this point would be over-interpretation as the limits are very rough. Again, deeper submm imaging observations are needed to place tighter constraints on the cold dust contents in NGC4374 and other ellipticals.

4.4 Conclusions

Following the suggestion that elliptical galaxies may contain diffusely distributed dust (Goudfrooij 1994), this was searched for with submm imaging observations of the elliptical galaxy NGC4374, using SCUBA. Low-level, diffusely distributed dust was not detected. The 3σ upper limit on the 850 μm integrated flux within a region of about $2'$ (13 kpc of the galaxy) diameter, just less than the SCUBA array, is $\sim$ 0.6 Jy, giving the flux density upper limits on the undetected low, level diffuse dust. The emission at 850 μm is spatially unresolved (diameter $< 15''$), showing that the detected dust is confined to the central region of diameter < 1.5 kpc.

Adding the SCUBA submm data to existing radio through IR data for this galaxy, the core dust component can be constrained to a single temperature of $\sim$ 30 to 40 K, implying a dust mass of $\sim 1.2 \times 10^5 M_\odot$. The model fitting in Section 4.3.1 gives an angular extent of the dust to be $\sim 1''.5$ in diameter, which corresponds to a size-scale of only 0.15 kpc. Mindful that this result is too simplistic for a radiative model of an AGN torus (e.g. Alexander et al., 1999), it is noted in passing that if there is a co-mixing of the molecular gas and dust, this constrains the size of any molecular torus around the

AGN core of NGC 4374 to around only 150 pc in diameter. Using the 3σ upper limit of the 850 μm integrated flux within a region just less than the SCUBA array ($\sim$ 13 kpc of the galaxy diameter), a very rough dust mass limit is determined of $3.6 \times 10^7 M_\odot$ and $1.2 \times 10^7 M_\odot$ for the undetected cold diffuse dust of $T = 12$ and 18 K respectively, which is of similar order to the dust contents in luminous spiral galaxies.

The mm-submm observations show a flat spectral index that is consistent with the 5 GHz radio core flux. The spectral index of the 850 to 2000 μm fluxes alone is consistent with that expected from free-free emission. The possibility of a free-free component is very unusual and intriguing. Given the care taken over calibration, no systematic reasons for the peculiar mm-submm SED seems likely.

A flat mm-to-submm spectrum has also been observed in the core of Centaurus A (see Chapter 5), and it may be characteristic of low-luminosity blazars (Hawarden et al., 1993). If indeed the submm core spectrum is flat as the observations indicate, the results would plausibly support the hypothesis that *flat* spectra are a characteristic of low-luminosity blazars, as NGC 4374 is a low-luminosity FR I radio galaxy like Centaurus A. Submm observations of a larger sample of these objects are needed to provide a more definitive test.

Chapter 5

Direct Imaging of Cold Dust Structures in Centaurus A

5.1 Introduction

NGC 5128 (Centaurus A) is the nearest giant elliptical galaxy and is remarkable in several respects. It is a powerful radio source with a double-lobed structure extending approximately $3.5° \times 8°.5$ on the sky (Bolton et al., 1949; Clarke et al., 1992; Tingay et al., 1998). At the other extreme of scales a central source, less than 0.4 milliarcsec (~ 0.008 pc) in extent (Kellermann et al., 1997), is prominent on radio through X-ray images. This feeds subparsec-scale relativistic outflows that are approximately aligned with, and clearly the generators of, the vast outer radio lobes.

The optical appearance is dominated by a dramatic warped dust lane at least $12'.5$ in E-W extent, which effectively bisects the main body of the elliptical galaxy and almost completely obscures the nucleus and all optical structure in the inner 500 pc (e.g. Schreier et al., 1996). The outer isophotes of Centaurus A are markedly elongated in P.A. $\sim 25°$.

Faint shells, associated with both H I and CO emission, are evident in these outlying parts (Malin et al., 1983; Schiminovich et al., 1994; Charmandaris et al., 2000). The somewhat chaotic dust lane, and especially the shells, are strong evidence of a relatively recent merger (Baade & Minkowski, 1954; Graham, 1979; Tubbs, 1980; Schreier et al., 1996; Israel, 1998) which is generally believed (cf. Marconi et al., 2000, and references therein) to be responsible for the nuclear activity.

Hα and molecular line observations (e.g. van Gorkom et al., 1990) indicate that the nucleus is surrounded by a rapidly rotating massive inner disc with a pronounced warp (Nicholson et al., 1992; Quillen et al., 1992), a scenario that is supported by modelling of the structure of the obscuring dust seen in near-infrared (Quillen et al., 1993) images.

At an assumed distance of ~ 3.5 Mpc (Hui et al., 1993), 1″ at Centaurus A corresponds to 20 pc; hence, it is close enough that observations with large single dish telescopes and interferometers can be used to reveal details of the structure of the galaxy at radio through submillimetre (submm) wavelengths. Previous observations have been reviewed extensively in the literature, most recently by Israel (1998). Here, new deep observations at submm wavelengths, that are sensitive in particular to emission from cold interstellar dust, are described.

Submm-wavelength emission, apparently thermal in origin, was first observed from Centaurus A by Cunningham et al. (1984), using the single-pixel bolometer UKT 14 mounted on the 3.8-m UK Infrared Telescope with a beam size of $\sim 80''$. Millimetre-wave continuum observations by Eckart et al. (1990) in 22″ and 45″ beams show an unresolved nuclear source, surrounded by extended thermal emission seen by *IRAS* at 60 and 100 μm and which is roughly co-extensive with a region of strong CO molecular line emission. More extensive submm continuum observations were made by Hawarden

et al. (1993), who mapped the galaxy using the smaller beamsize of $\sim 15''$ afforded by UKT14 mounted on the 15-m James Clerk Maxwell Telescope (JCMT). Although extended emission was visible in their images, these were not sensitive enough to reveal much detailed structure beyond a general extension corresponding to the optical dust lane and a brighter, elongated, central feature, with an apparently thermal spectrum, surrounding the strong, flat-spectrum nuclear source.

This chapter presents new high-quality deep submm images of Centaurus A obtained with SCUBA. These resolve the structure of the inner disc down to scales of ~ 150 pc, while also revealing details not previously seen of the faint outer dust emission at large radii. These results are compared with observations by Mirabel et al. (1999) who used ISOCAM, the infrared (IR) imager on the *Infrared Space Observatory* (*ISO*), to obtain images at mid-IR wavelengths. Additionally, reprocessed *IRAS* data is used to complement the detailed study of the dust properties in the disc.

5.2 Observations

Centaurus A presents special challenges for observations at submm wavelength from Mauna Kea since it never rises more than 28° above the southern horizon. Images were nevertheless obtained using SCUBA during several observing periods in 1998.

The simultaneous 850 and 450 μm images were obtained during three nights (UT 1998 March 29, April 9 and April 11) during a period in which sky conditions were exceptionally transparent, with zenith opacities often as low as 0.1 and 0.4 or better at 850 and 450 μm respectively. The data were taken using the "jiggle-mapping" mode of SCUBA. A series of seven overlapping field centres were observed, placed 55″ apart along a line at a position angle of 120° (North through East), roughly corresponding to that of

the dust lane of Centaurus A. The chop throw was 120″ perpendicular to this line.

The strong overlap (> 50%) between neighbouring fields compensated for the limited rotation of the very southerly source with respect to the SCUBA arrays, offsetting the effect on the final reduced images of occasional excessively noisy pixels. A different subset of the seven fields was observed on each of the three nights. Since the bright nucleus appears on the central three fields, it was observed at least twice per night, allowing corrections for pointing drifts to be measured and applied to the final images.

To determine the beam pattern of the JCMT, the bright unresolved blazar 3C 279 was observed each night using the same jiggle-pattern mode as applied to Centaurus A. Atmospheric opacities were determined from skydips made at intervals during the observing, and instrumental gains were derived from images of the JCMT secondary calibrators CRL 618, IRC+10216 and 16293−2422 (Sandell 1994, 1998). Corrections for pointing drifts were incorporated in the final images using the fields in which the core source appeared. The apparent core source size was reduced from 9.2 to 8″.4 (FWHM) at 450 μm after the inclusion of these corrections.

An image at 850 μm had been previously obtained under somewhat worse conditions on UT 1998 February 14, 15 and 16. This image was made using the "scan-mapping" mode and covers an area 4′ square centred on the bright core source. Despite the lower quality of this dataset, it provides a useful comparison for the reality of features in the two 850 μm images. The sky transmission was not good enough on this occasion for the simultaneous 450 μm data to be useful. The instrumental gains for the "scan-mapping" mode observations are 20% less than those typical for the "jiggle-mapping" mode; therefore, the gains have to be determined separately for the individual modes. The beam in the 850 μm "scan-mapping" image of Centaurus A in this paper is slightly

larger than in the "jiggle-mapping" images and the photometry differences between the two final maps are within and proportional to the uncertainties: the percentage differences are larger in the less sensitive parts of the maps.

5.3 The Submm Images and Comparisons with other Wavelengths

The images of Centaurus A at 850 and 450 μm obtained from the combined "jiggle-map" datasets are about 6′ long and 2′ wide (respectively 7 and 1.7 kpc at Centaurus A) and cover much of the dust disc. They are shown in Figures 5.1 and 5.2. Figure 5.3 presents the 850 μm image obtained from the "scan-mapping" observations.

The submm images show extended emission centred on the nucleus of Centaurus A and oriented at a position angle of about 115° (North through East) on the plane of the sky, clearly corresponding to the prominent optical dust lane. Within about 90″ at both 850 and 450 μm, the emission has a much higher surface brightness than at larger radii. The bright structures have a reversed S-shape suggestive of spiral structure or, as pointed out by Mirabel et al. (1999), a bar.

The central source has a flux density per beam at least 40 times brighter than the surrounding emission from the dust lane, as shown in the profiles along the major axis in Figure 5.4. Furthermore, the close resemblance of the central source to the profiles of the JCMT beam (line with crosses in Figure 5.4), shows the source is unresolved. The point-source core has been isolated from the extended emission and separate submm-to-IR spectral energy distributions (hereafter SEDs) have been constructed for the core and extended galactic emission. These are discussed in Section 5.6.

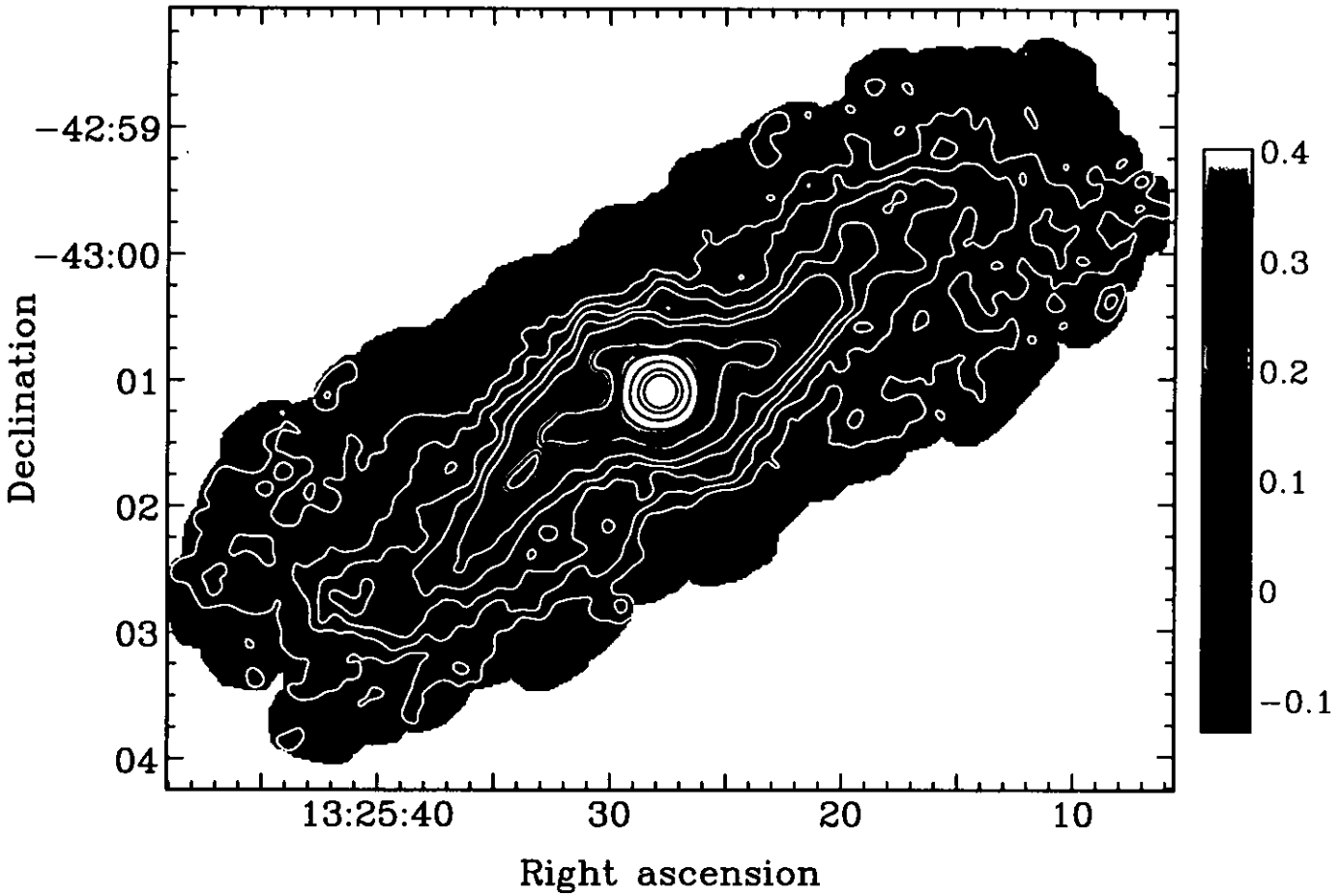

Figure 5.1: Image of Centaurus A obtained with SCUBA at 850 μm derived from individual "jiggle-mapping" exposures offset along a line roughly corresponding to the optical dust band of Centaurus A. The central source is displayed saturated in order to highlight the low-level, extended emission. The panel key indices are in Jy/beam corresponding to colour-coded intensities, and the contour heights in the image are 0.01, 0.03, 0.05, 0.07, 0.1, 0.14, 0.2, 0.3, 0.4, 1.0, 2.5 and 4.0 Jy/beam.

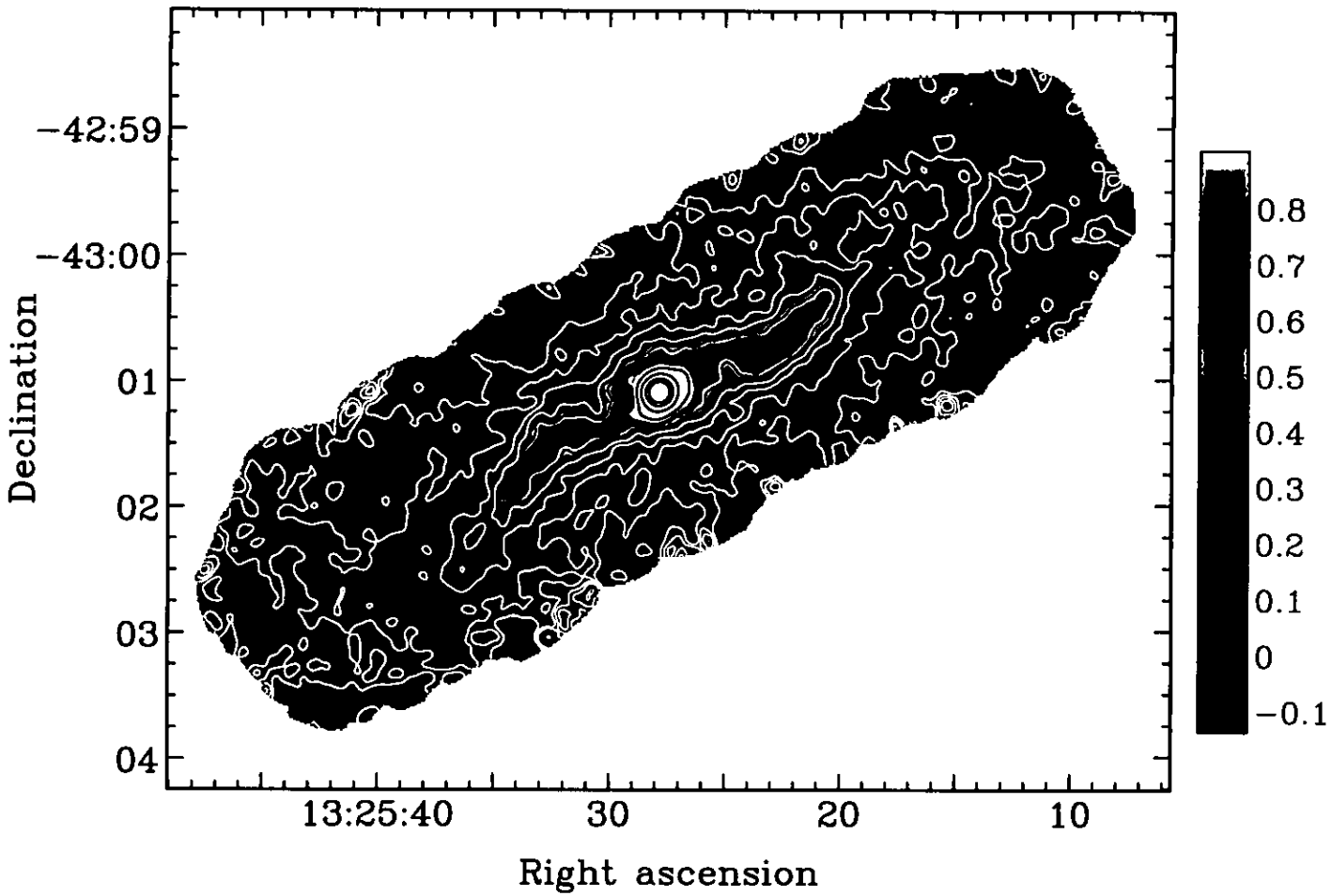

Figure 5.2: Image of Centaurus A obtained with SCUBA at 450 μm derived from individual "jiggle-mapping" (see text) exposures offset along a line roughly corresponding to the optical dust band of Centaurus A. The image is smoothed slightly and the central source displayed saturated in order to highlight the low-level, extended emission. The panel key indices are in Jy/beam corresponding to colour-coded intensities, and the contour heights in the image are 0.04, 0.16, 0.28, 0.40, 0.52, 0.8,1.0, 1.5, 2.5 and 3.5 Jy/beam.

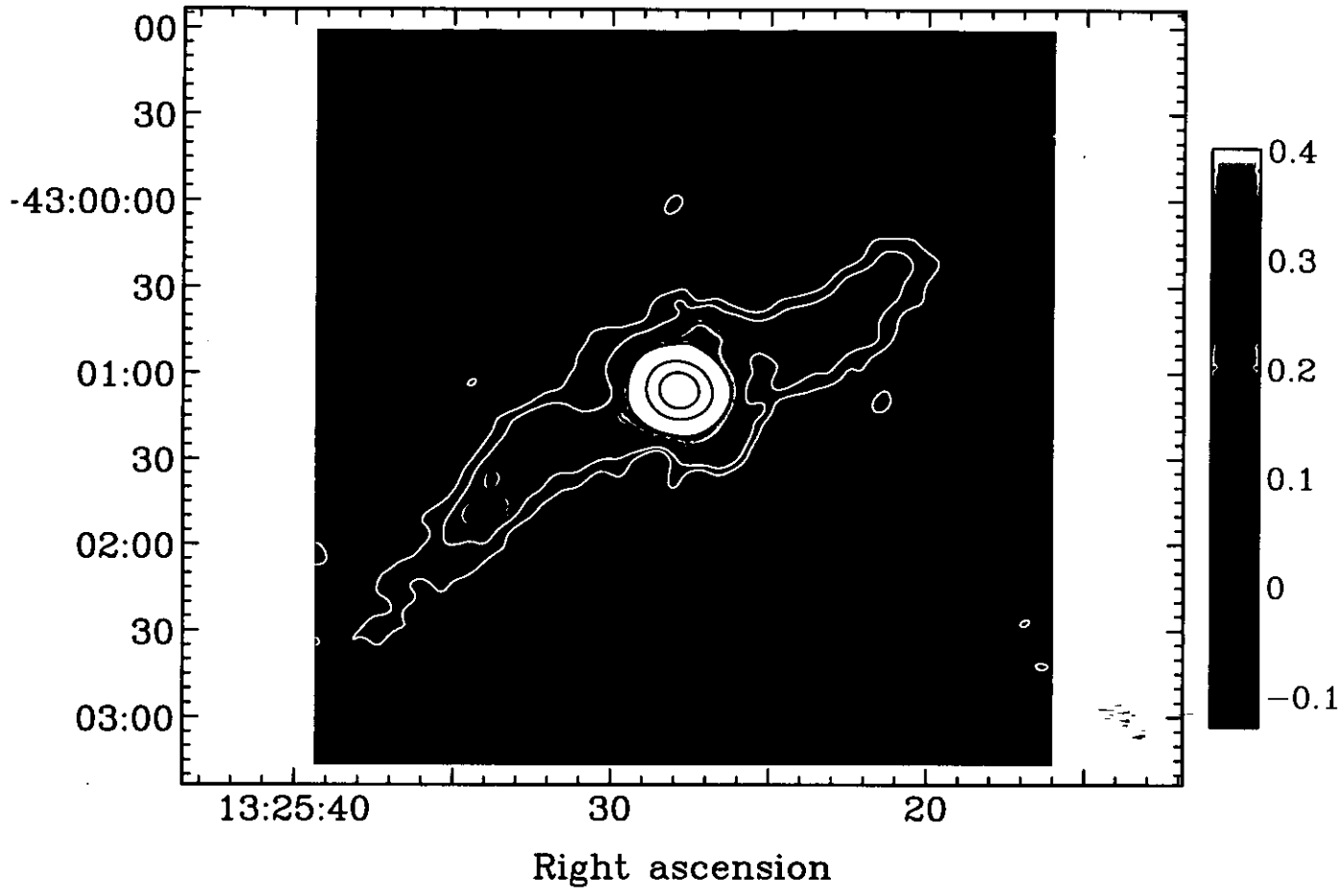

Figure 5.3: Image of the central 4′ at 850 μm obtained with SCUBA and using the scan-mapping technique. The central source is displayed saturated in order to highlight the low-level, extended emission. This map covers a smaller area than the jiggle-maps of Figures 5.1 and 5.2 and is thus not plotted to scale with those. The panel key indices are in Jy/beam corresponding to colour-coded intensities, and the contour heights are 0.07, 0.1, 0.2, 0.4, 1.0, 2.5 and 4.0 Jy/beam.

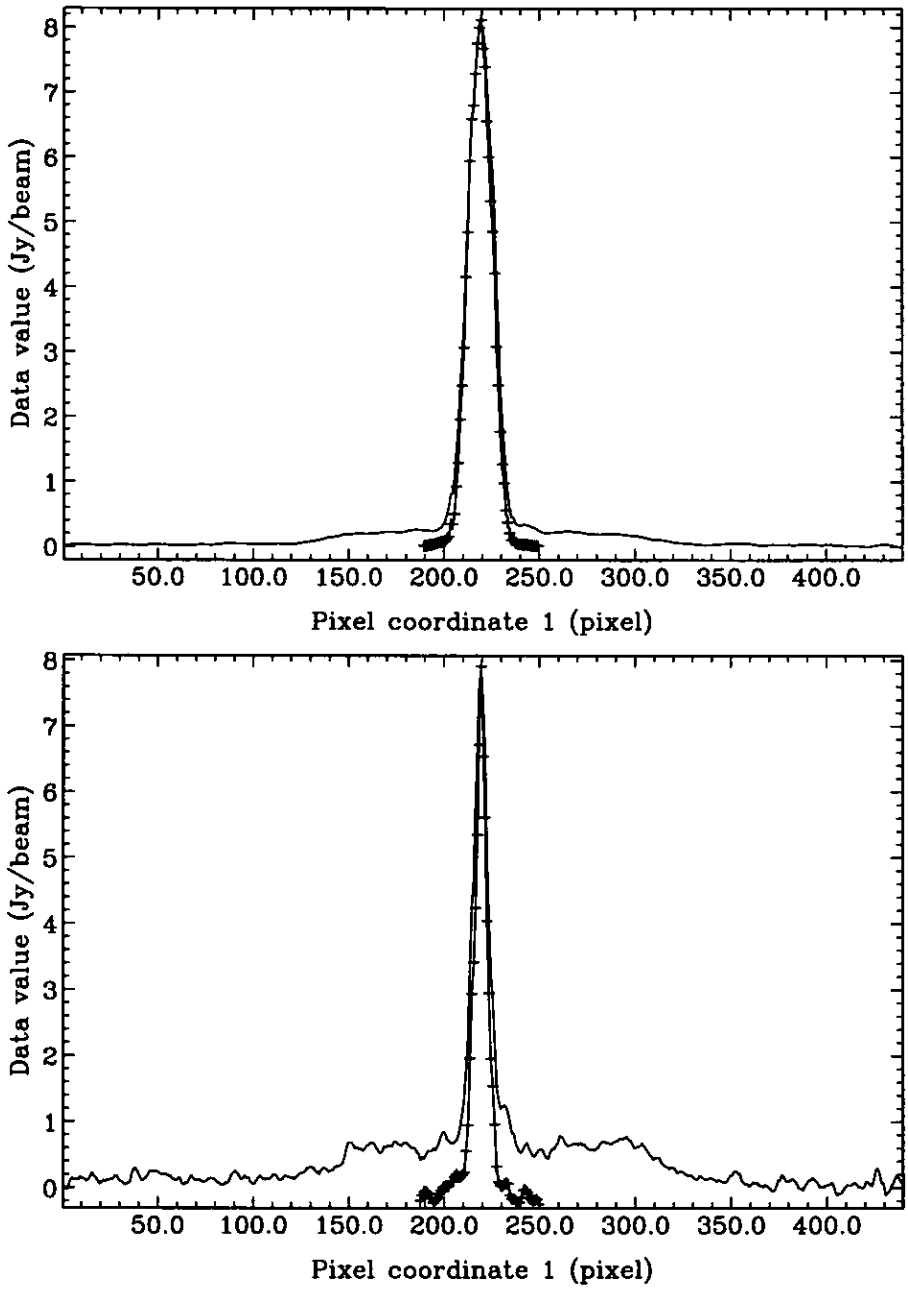

Figure 5.4: Profiles of the emission from Centaurus A at 850 and 450 μm (top and bottom respectively) along an axis roughly coincident with the optical dust lane. The profile of the JCMT beam is superimposed in a line marked with crosses. This beam profile is obtained from a map of the JCMT pointing source 3C279 scaled to the peak flux of Centaurus A and determined along an axis roughly coincident with the major axis of the dust lane. The horizontal offsets are in pixels, re-binned so that one pixel equals one arcsecond, and the vertical axis is in Jy/beam.

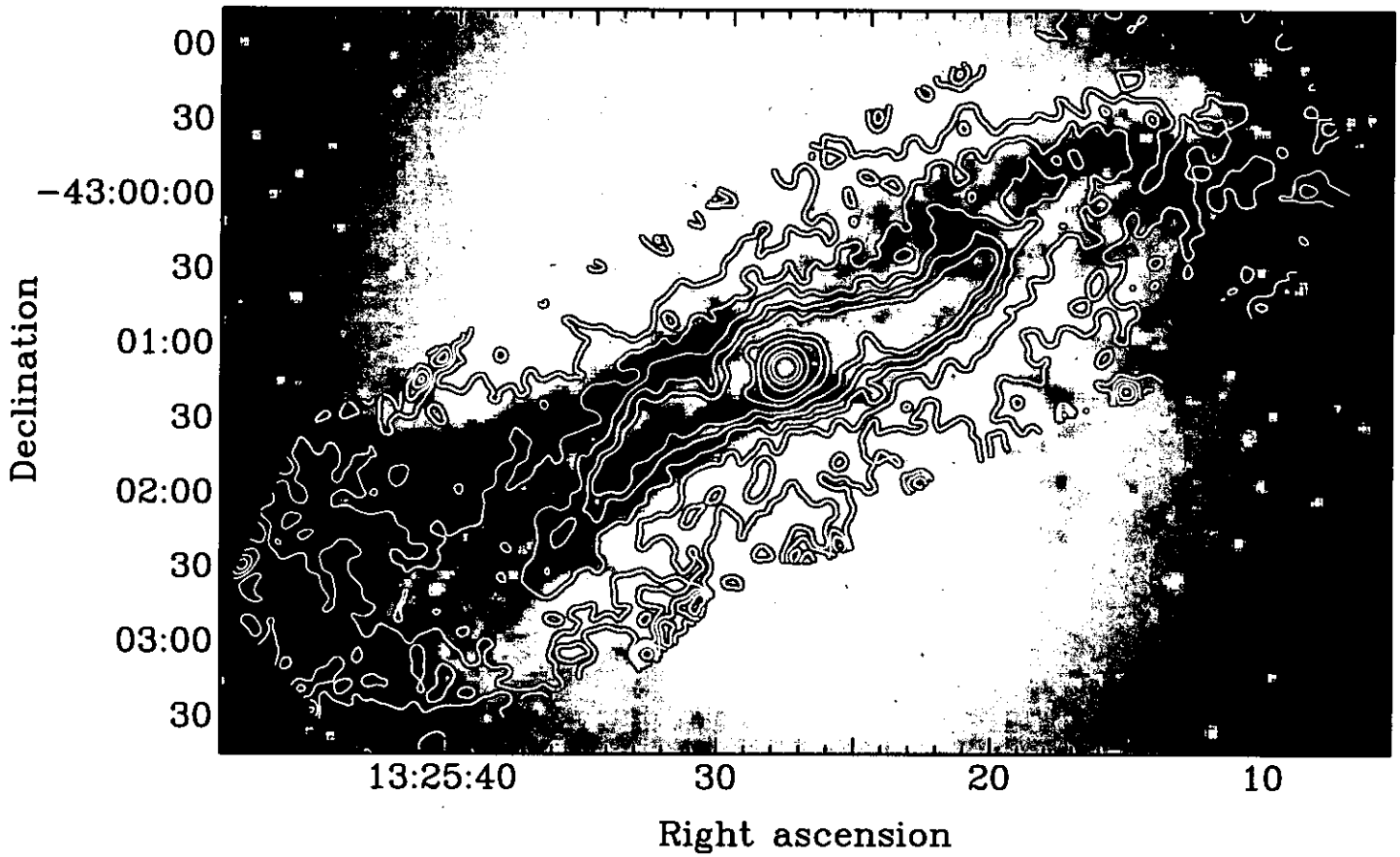

Figure 5.5: Contours of the 450 μm image superposed on an optical J waveband image of Centaurus A, digitised from the $IIIaJ$ emulsion photographic plates which are sensitive to emission between 395 and 540 nm wavelengths, courtesy of the Anglo-Australian Observatory.

Figures 5.5, 5.6 and 5.7 show the 450 μm contours, from the highest resolution SCUBA image, superimposed on 1) an optical J waveband image courtesy of the Anglo-Australian Observatory[1], 2) the 7μm ISOCAM image and 3) the 100 μm *IRAS*, HIRES-reprocessed image. In Figure 5.7, the 450 μm image is smoothed to a resolution comparable to that in the 100 μm HIRES map.

The SCUBA contours were overlaid on the optical, *ISO* and *IRAS* images using the Starlink program CONTOUR, within the KAPPA software package, which aligned the images in the celestial co-ordinate system. Before the alignment, the KAPPA program WCSFRAME was used to convert the images from their supplied celestial co-ordinate frame and the epoch at which the sky co-ordinate system was determined to the Julian 2000 co-ordinate frame, which is the domain in which all the Centaurus A images here are plotted. Aligning the images using the celestial co-ordinates was preferred because Centaurus A has very different structure in the wavelengths that were compared here, and there was no unresolved astrophysical source seen and known to be co-spatial in all the frames. Such a source(s) would have provided a point(s) to do the alignment independent of the astrometry accuracy of the different telescopes that supplied the sky co-ordinates in their respective maps. The SCUBA and *ISO* images were exceptions to this; because, in both cases the AGN core of Centaurus A was unresolved and much brighter than the surrounding structure. For these two maps, registration was determined assuming that the unresolved submm and mid-IR sources had a common origin on the sky and using the JCMT supplied co-ordinates, because the telescope's pointing accuracy at the elevation of Centaurus A is about 1″.5 compared to 3″.5 for *ISO*. This involved shifting the *ISO*

[1]Original plate material for the Digitised Sky Survey in the southern sky is copyright (c) the Anglo-Australian Observatory and was used, with their permission, to produce the The Digitised Sky Survey at the Space Telescope Science Institute under US Government Grant NAG W-2166.

image by 6″ west and 2″ south to the SCUBA sky position. As noted in Section 5.3.2, this results in remarkly well aligned extended and unresolved structure.

5.3.1 Submm vs. Optical Morphology

The well-defined reverse-S-shape structure that is seen in high surface brightness submm emission, within 90″ of the galaxy nucleus, is largely indiscernible in optical maps, implying that the denser material around the nucleus, seen in the submm, is heavily obscured in the optical. However, the southern edge of the SE high surface brightness submm emission aligns with the southern ridge of the optical dust lane, in turn suggesting that the SE reverse-S-shape structure is on the near-side and therefore relatively less obscured in the optical, as reported by Block & Sauvage (2000) and Quillen et al. (1993), based on their analysis of mid-infrared versus V and near-infrared data respectively. Furthermore, if the submm/optical morphology is a manifestation of a warped dusty disc or spiral structure that is highly inclined on the plane of the sky (c.f. Section 5.5), the southern edge is consistent with an inner fold of the disc seen tangent to the line of sight. Such a ridge would have a high column density in the line of sight, as evident in the aligned southern edges of *high* surface brightness submm emission and the *dark* optical lane.

The low surface brightness submm emission generally follows the optical dust absorption distribution, including the clockwise twists in the east and west of the dust lane. This submm emission corresponds especially well with the dark optical obscuration in the NW and NE and also the very dark twist in the east, indicating that some low level submm emission must arise from the optically prominent dust material. There is no marked difference between the flux densities of submm low level emission that corresponds with the dark optical obscuration in the NE and the low level emission in the

southern edge of the dust lane: in both regions, the flux densities are in the range ~ 40 to ~ 120 mJy/beam and ~ 10 to ~ 60 mJy/beam at 450 and 850 μm respectively. Schreier et al. (1996) find that the extinction in the southern ridge is much more than that in the NE, where it reduces the R flux by a factor of 6 compared to a factor of only 1.5 to 2 in the NE. Therefore, the similarity of the flux densities in the northern and southern low level submm emission despite the higher extinction in the southern ridge indicates that the NE dust lane is well in the foreground, in a region of low stellar density, and is thus heated by a more dilute stellar radiation field.

Within the length (major diameter) of 270″ that excludes the clockwise twists, low surface brightness submm emission extends farther north and south beyond the optical feature: the average width (minor diameter) of the dust feature seen in submm emission is $\gtrsim 90''$ compared with the optical obscuration of $\lesssim 60''$ (see Figure 5.5). The extension is appreciably so in the south, where the dust giving rise to the submm emission here lies on the far-side of the galaxy and is overlain by the stellar body. Consistent with this scenario, when Schreier et al. (1996) removed the effects of foreground dust obscuration from *HST* I' band images, they found a band of residual obscuration, presumably caused by dust within the stars on the farther side of the galaxy.

While it is clear that the maximum width at which the dust lane will be detected in extinction and seen in thermal emission will depend on the relative sensitivity of the two techniques, the width at which the feature is detected in the submm observations ($\gtrsim 90''$, cf. Figure 5.5) surpasses the maximum width detected in all optical observations currently available in literature, including the recent *HST* (Schreier et al., 1996; Marconi et al., 2000) and VLT[2] observations ($\lesssim 60''$), supporting the assertion that the low-level

[2]VLT astronomical image gallery is available at http://www.eso.org/outreach/info-

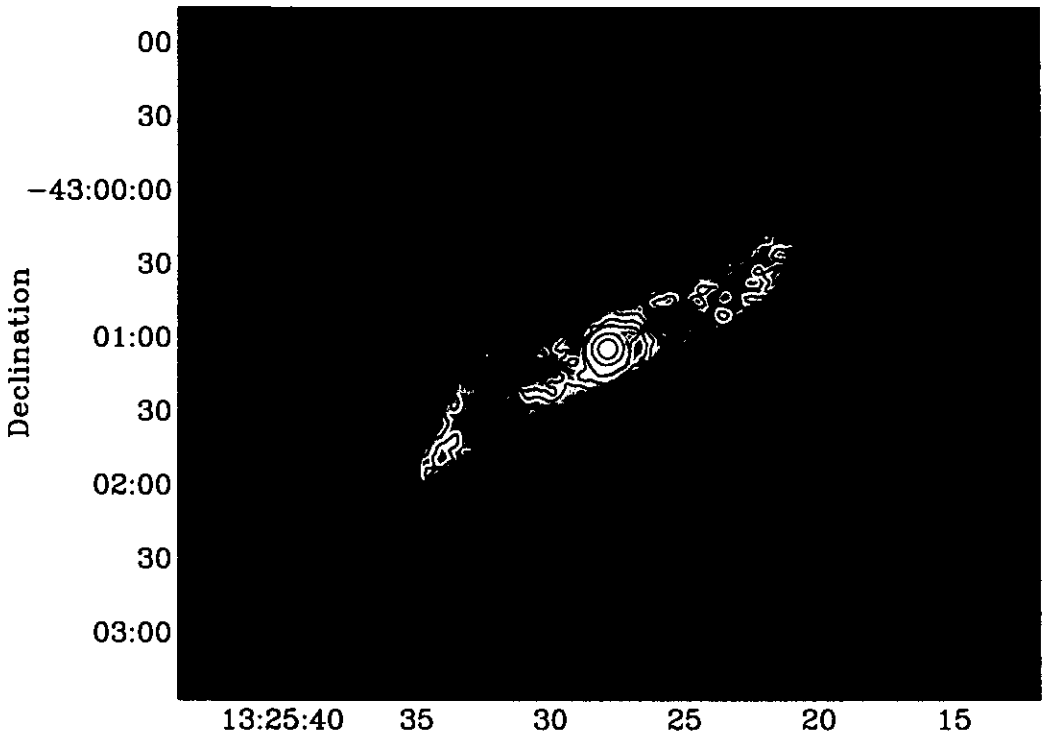

Figure 5.6: Contours of the 450 μm image of Centaurus A (see 5.2) superposed on a 7μm ISOCAM image (Mirabel et al. (1999)).

submm emission extends well beyond the optical obscuration.

5.3.2 Submm vs. *ISO* Mid-IR Morphology

Mirabel et al. (1999) presented images of Centaurus A at 7 and 15μm obtained with ISOCAM as well as early SCUBA "jiggle-mapping" images of a 2′ field around the core of the galaxy at 450 and 850μm. They note the similarity of their IR (ISOCAM) and submm (SCUBA) images (which are much less sensitive to faint emission than those presented here), observing that there was the "same general distribution" between the "warm" and "cold" dust seen respectively in the ISOCAM and the early SCUBA image published by them. Mirabel et al. (1999) conclude that the absence of submm emission from the optical dark lanes "is not due to major differences between the spatial distributions of

events/ut1fl/astroimages.html

the cold and very warm dust components," attributing the optical dust features to "small amounts of cold dust in the outer parts" of the system.

The SCUBA data exhibited in this thesis, which have much greater sensitivity and extend much farther from the nucleus than the images published by Mirabel et al. (1999), show that there are *remarkable* similarities between the appearance of Centaurus A in the mid-IR and the submm (see Figure 5.6 and 5.7). This is particularly true of the 450 and 7μm images, even though their wavelengths differ by a factor of 65. Both images show the reverse-S-shaped, high surface brightness submm structure out to 90″ from the core and the fainter extensions of this structure out to 120″. The major *difference* is that the submm emission is seen to much larger angular distances than is the mid-IR, and as pointed out above, faint submm emission from some of the more outlying dust in the optical dust lane is evident.

The contours in Figure 5.6 show a feature extending to about 15″ radius from the nucleus in position angle 145°; this may correspond to that attributed to a circumnuclear torus by Hawarden et al. (1993); Israel (1998) and Bryant & Hunstead (1999). The SCUBA and ISOCAM images suggest it may represent the inner folds of the reverse-S-shaped structure (or warped disc, c.f. Section 5.5) mentioned above.

5.3.3 Submm vs. *IRAS* Far-IR Morphology

Archival *IRAS* data for Centaurus A were re-analysed using the HIRES facility to extract the best possible spatial resolution and to ensure the same registration of the regions to determine integrated fluxes for comparison with the SCUBA and ISOCAM measurements (c.f. Section 5.6). The resolutions achieved in the *IRAS*, HIRES-reprocessed images (of Figure 5.8) are 60″, 50″, 80″ and 90″ respectively at 12, 25, 60 and 100μm, which are

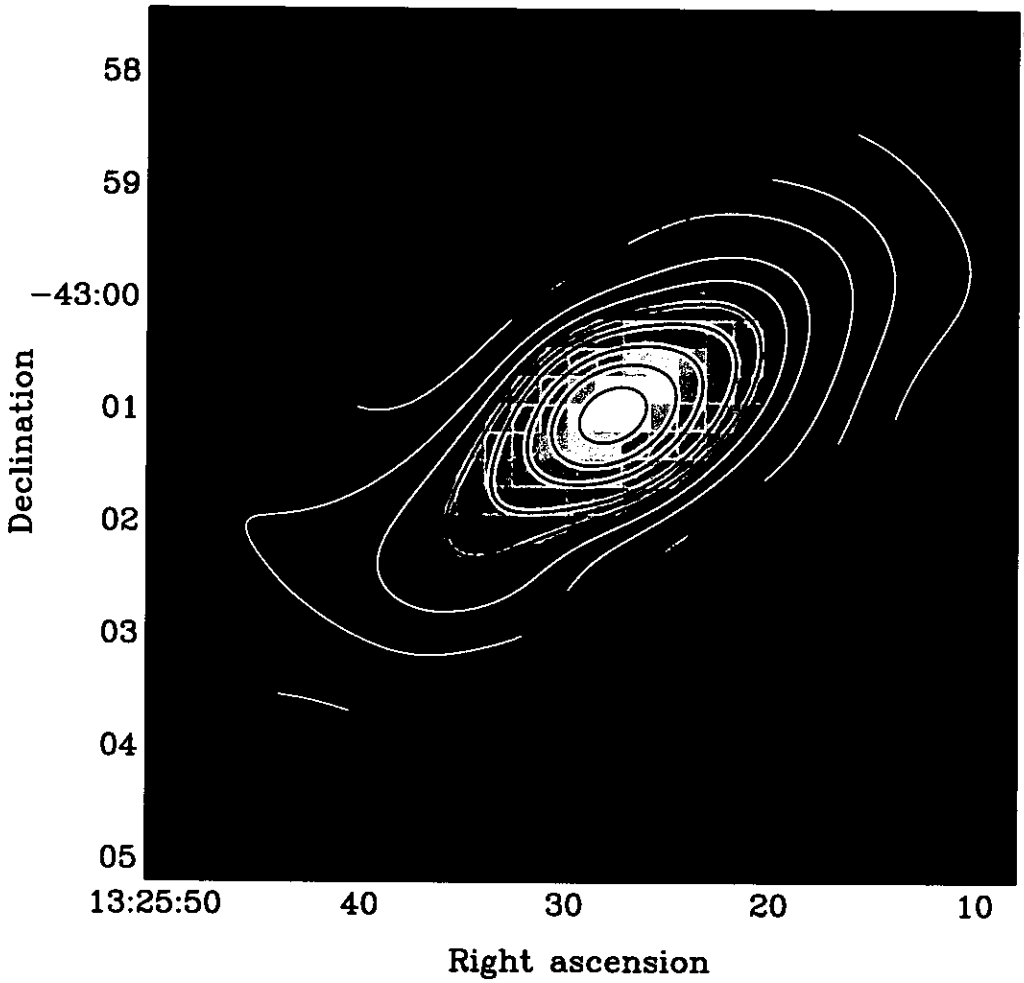

Figure 5.7: Contours of the SCUBA image of Centaurus A at 450 μm (see Figure 5.2) superposed on the *IRAS*-HIRES image at 100 μm. The 450 μm image is smoothed to a resolution comparable to that in the 100 μm HIRES map (i.e. 90″).

much larger than the 4″ to 15″ resolutions in the ISOCAM and SCUBA images.

As shown in Figure 5.8, the extent of the *IRAS* detected emission increases with wavelength. At the short wavelength range (12, 25μm), the emission is extended to scales comparable to the ISOCAM detections, while at 100 μm the emission is broadly similar to the very extended 450 μm detections (see the 450μm image smoothed to a similar resolution and overlaid on the *IRAS* 100 μm image in Figure 5.7). A full analysis of the mid-infrared to submm spectral energy distribution therefore needs to refer to

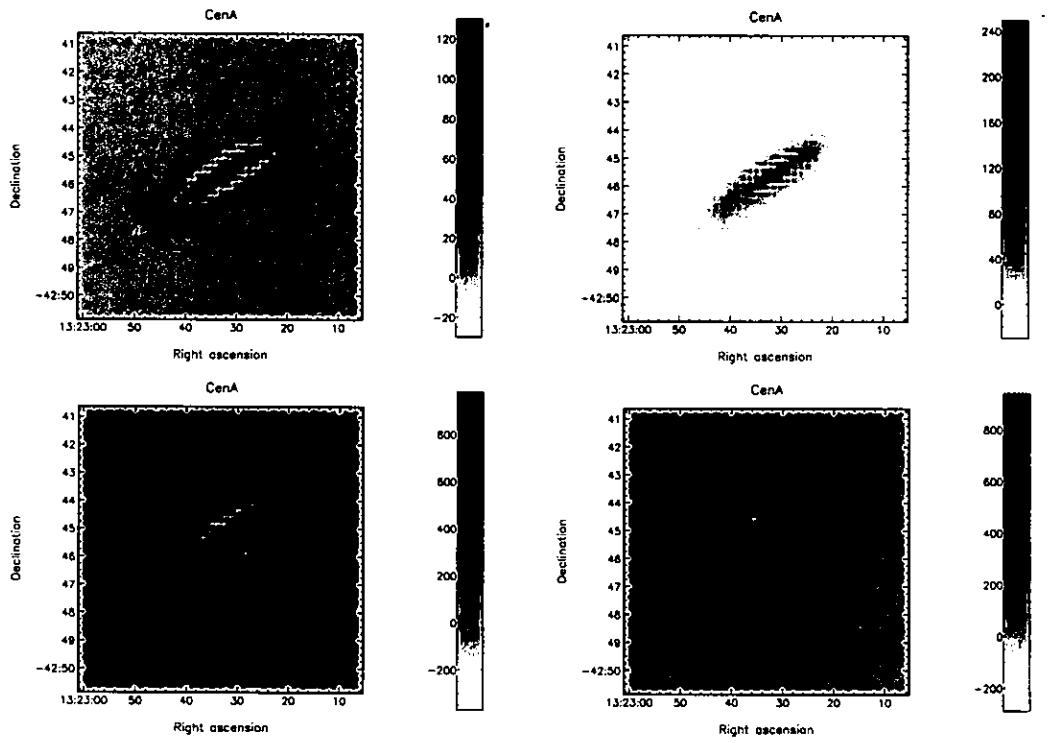

Figure 5.8: *IRAS* reprocessed 12, 25 (top panels), 60 and 100 μm(bottom panels) images of Centaurus A.

particular spatial locations. The submm observations and 60 and 100 μm *IRAS* data allow this for the large-scale "cold" component out to $\sim$ 7 kpc from the nucleus.

In an early comparison of their 100 μm and CO (1–0) data, Eckart et al. (1990) concluded that about half of the 100 μm emission was more extended than the CO (1–0) molecular disc and was not associated with massive star-formation, but rather with diffuse "cirrus" clouds. They predicted that the submm extended emission would follow this extended far-IR emission, which, as can be seen from Figure 5.7, is indeed the case: the very low-level 100 μm emission exhibits a morphology with large western and eastern warps comparable with the optical dust lane and the submm images. This also resembles the distribution of the H I detected in Centaurus A (Schiminovich et al., 1994), indicating that the H I emission traces the "cirrus" dust in this galaxy just as in the Milky Way.

5.3.4 Submm vs. Warped-Disc–Model Morphology

Figure 5.9 shows contours from the warped-disc model, that was proposed by Quillen et al. (1992) and explored by Quillen et al. (1993), overlaid on the 850 μm image of Centaurus A in pixel co-ordinates and aligned about the high surface brightness, reverse-S-shaped submm structure. The warped-disc model was originally determined to fit the velocity field observed in CO emission (Quillen et al., 1992) and then modified to produce the geometry that would show the absorption features observed in the J, H and K band infrared images of Centaurus A (Quillen et al., 1993).

The overlay in Figure 5.9 shows that the overall reverse-S-shape morphology is more extreme and the distance of the eastern- and western-disc warps is underestimated in the model than in the emission observations. However, the correspondence between the two morphologies, particularly from about radii 25″ to 90″, is striking, especially because the model geometry was constructed to match infrared images tracing extinction and a velocity field rather than an emission map. This good correspondence constrains the disc inclination to the line of sight and position angle on the sky plane respectively to $65 \pm 6°$ and $120 \pm 6°$. Model plots with disc inclination and position angle outside these deviations show less direct resemblance to the SCUBA images.

The contours in Figure 5.9 not only demonstrate how well the model corresponds with the submm morphology but also illustrate the general disc geometry that is responsible for the dust structure that is seen in complex IR-submm emission and optical extinction images. In particular, the plot shows the almost face-on or high inclination of the disc to the line of sight, that is not directly apparent in the SCUBA or optical data, together with disc warps along a major-axis with (the more apparent) a SE-NW position angle of $\sim 120°$ on the plane of the sky.

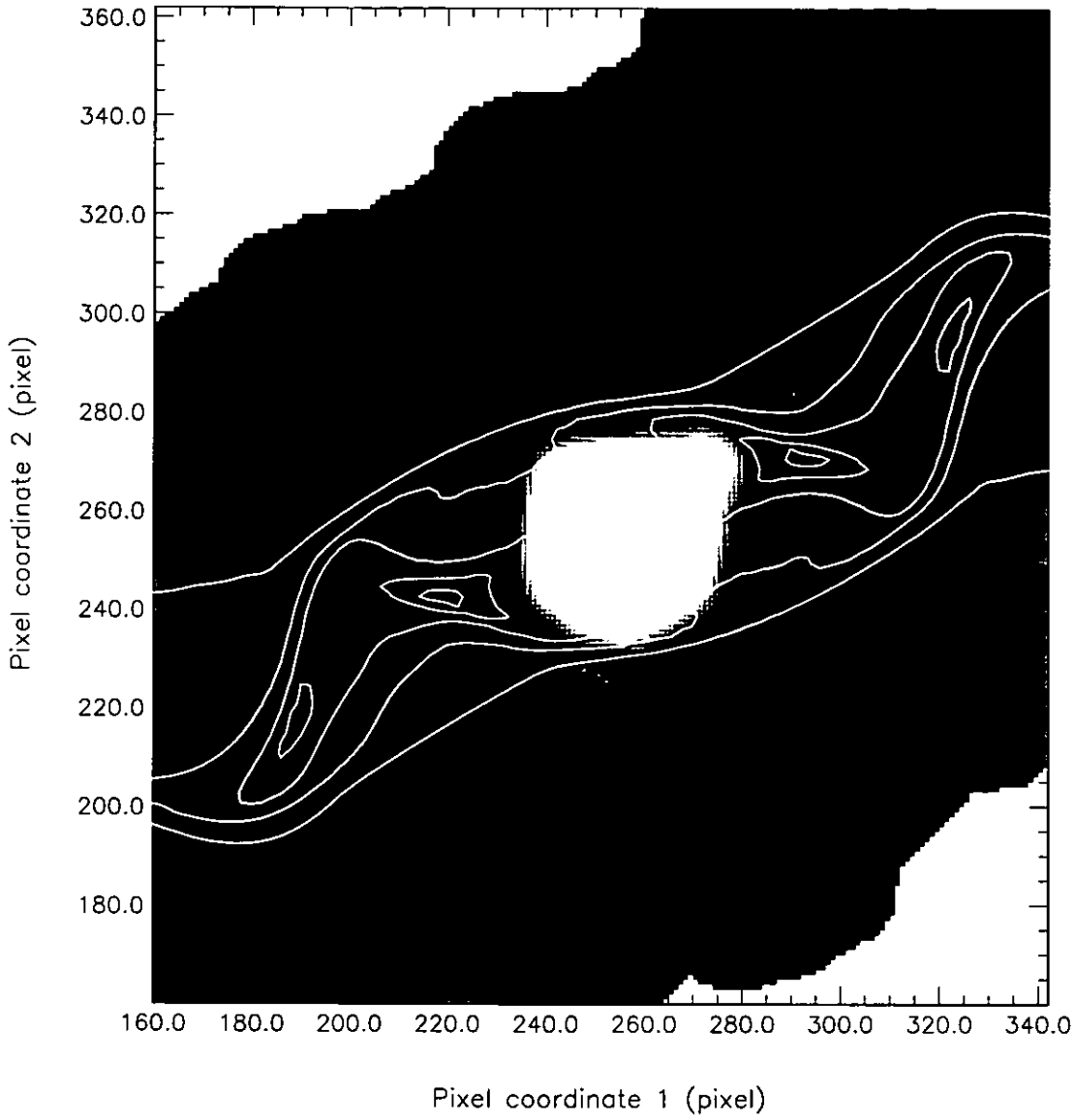

Figure 5.9: The inner $180'' \times 200''$ image of Centaurus A at $850\,\mu$m(see Figure 5.1), superimposed in pixel co-ordinates with contours from the geometric, warped-disc model, provided by Alice Quillen based on infrared-extinction work by Quillen et al. (1993) after modifications of an earlier CO-velocity model by Quillen et al. (1992). The contours illustrate the almost face-on or high inclination of the predicted disc to the line of sight (c.f. Figure 5.10). The pixel co-ordinates are plotted so that one pixel equals one arcsecond, and the colour codes mark relative $850\,\mu$m intensities.

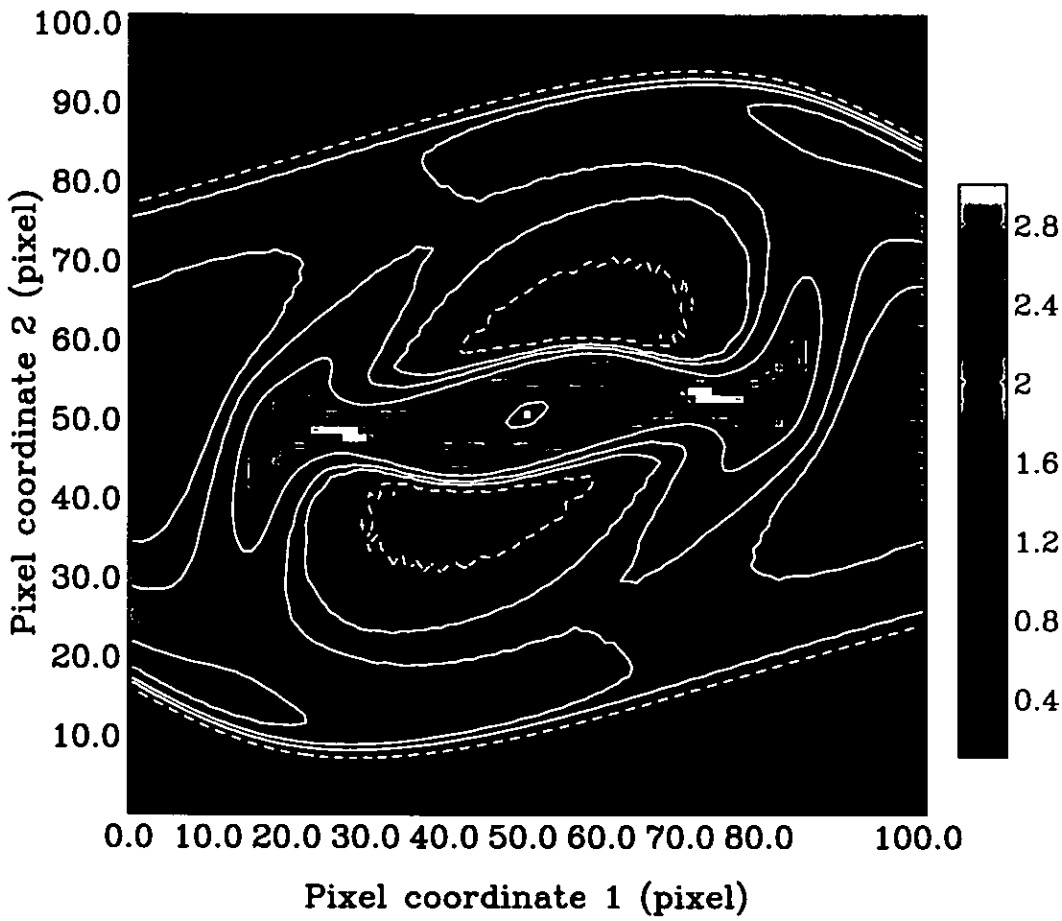

Figure 5.10: The face-on morphology produced from the warped-disc model of Centaurus A by Quillen et al. (1993) (cf. contours in Figure 5.9). The colour codes indicate relative model intensities, that are also marked out by contours at 90%, 70%, 50% and 30% of the peak intensity. The dashed contours are below 50% of the peak intensity, and the pixel co-ordinates are plotted so that one pixel equals 2.4 arcseconds.

The projected face-on morphology of the disc is displayed in Figure 5.10, where the model prediction by Quillen et al. (1993) (cf. contours in Figure 5.9) is now plotted at an inclination of 90°. The central, spiral-shaped warp that manifests within radii 90″ in the submm and infrared emission maps (see, e.g., Figures 5.6) is also apparent in this figure. The image supports the arguments in Section 5.5 that the warped-disc model predicts the spiral-shaped feature of the colder and warmer material seen respectively in the submm and mid-IR, rather well, without a need for any additional structures.

The morphology of the high surface brightness submm structure within radii $\sim 90''$, as seen in comparison with the model plots, suggests the scale height of the disc is no less than the 0.08 predicted by Quillen et al. (1993). A highly inclined disc with a lower scale height would result in a model with line of sight intensities (or column densities) that are relatively higher at the disc edges compared to the smoother folds and thus produce a disc morphology with more pronounced edges and sharper warps (see Figure 5.11). Plots of the disc that are produced with scale heights higher than determined by Quillen et al. (1993) show less severe warps within radii $\sim 90''$ and generally present a better correspondence with the high surface brightness submm emission up to scale height ~ 0.14 (see Figure 5.11), suggesting that the dust seen in the submm emission may have a higher scale height than determined in the model prediction. Scale heights higher than ~ 0.14 produce model morphologies that have very smooth high-brightness shapes with almost no warping and thus show much less resemblance to the submm emission maps. Further implications of the model on the data at the submm and other wavelengths are discussed further in Section 5.5.

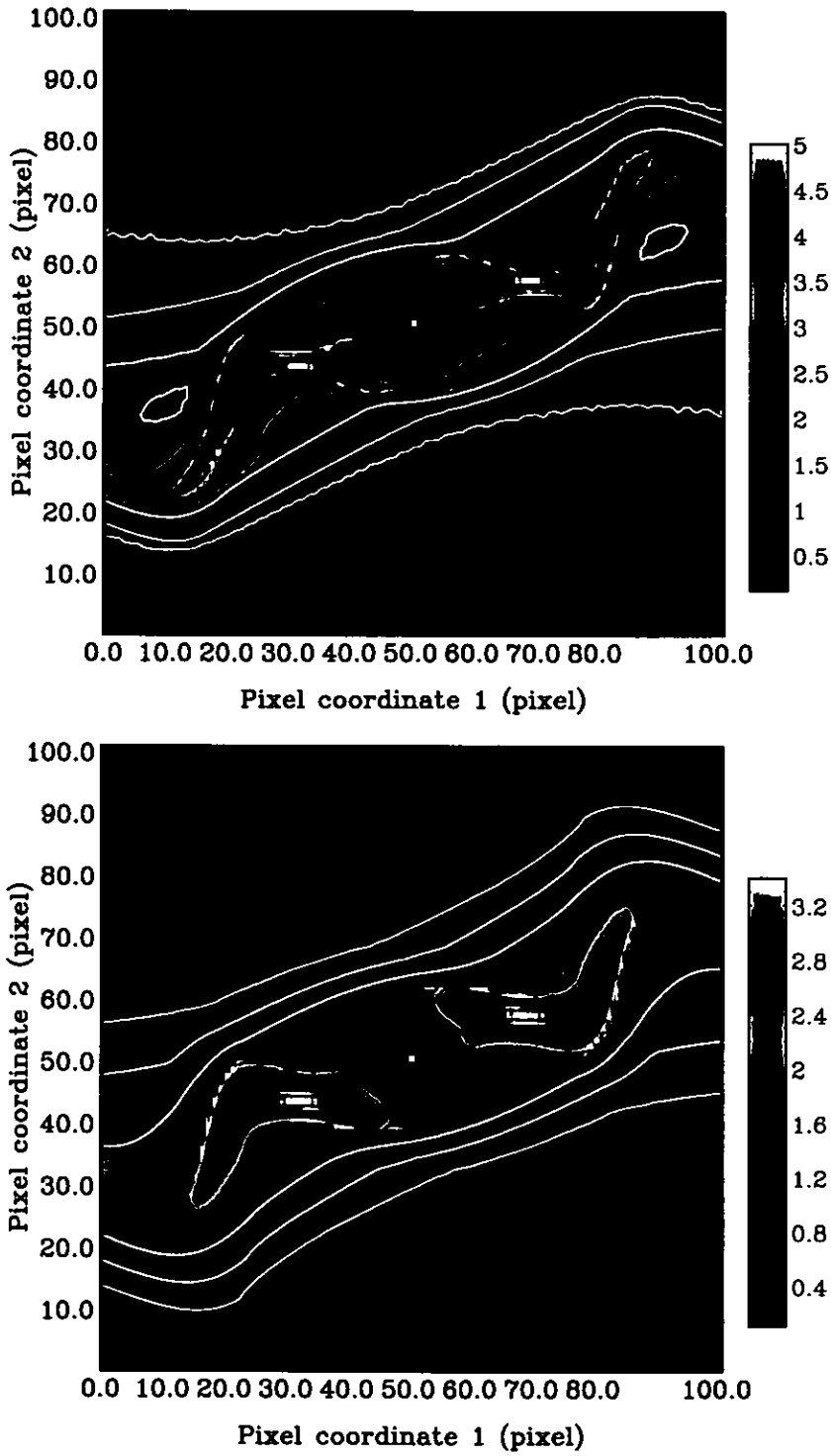

Figure 5.11: The warped-disc model of Centaurus A by Quillen et al. (1993) (cf. contours in Figure 5.9) is plotted with scale heights of 0.06 (top panel) and 0.14 (bottom panel). The colour codes indicate relative model intensities, that are also marked out by contours at 95%, 85%, 75%, 65% and 55% of the peak intensity. The pixel co-ordinates are plotted so that one pixel equals 2.4 arcseconds.

5.4 The Submm Spectral Index Distribution

Using the 450 and 850 μm imaging data, the global spectral index distribution of Centaurus A is derived at submm wavelengths and used to delineate the submm components in the nuclear regions of the galaxy as well as to investigate the dust properties of the extended emission. The following procedure was used. The 450 μm data were first smoothed to the 14″ resolution of the 850 μm map. The spectral index α, where $S_\nu \propto \nu^\alpha$, between 450 and 850 μm was then computed as

$$\alpha = \log\left[\frac{S_{450}}{S_{850}}\right] \Big/ \log\left[\frac{850}{450}\right], \tag{5.1}$$

where S is the flux density per beam at each point in the map. The uncertainty in the spectral index is then given by

$$(\Delta\alpha)^2 = \left[\left(\frac{\Delta S_{450}}{S_{450}}\right)^2 + \left(\frac{\Delta S_{850}}{S_{850}}\right)^2\right] \Big/ \left(\log\frac{850}{450}\right)^2, \tag{5.2}$$

where the variables are as for equation 5.1. The largest probable uncertainty in ΔS arises from the calibration, especially for the 450 μm flux densities. The maximum uncertainty in the final map is estimated as $\mid \Delta\alpha \mid_{\rm max} \approx 1.5$ and the mean uncertainty as $\mid \Delta\alpha \mid_{\rm mean} \approx 0.5$. The uncertainty in the regions with $\alpha > 3.2$ is most probably underestimated as this is also the region of the map with the least sensitivity.

The spectral index map of Centaurus A between 450 and 850 μm is shown in Figure 5.12. There are four regions apparent in the map. Contours at the spectral indices 2.0 (dashed lines) and 3.0 and 3.3 (solid lines) are overlaid to guide the eye to the less obviously manifested features. In the nuclear area, the unresolved core and a feature

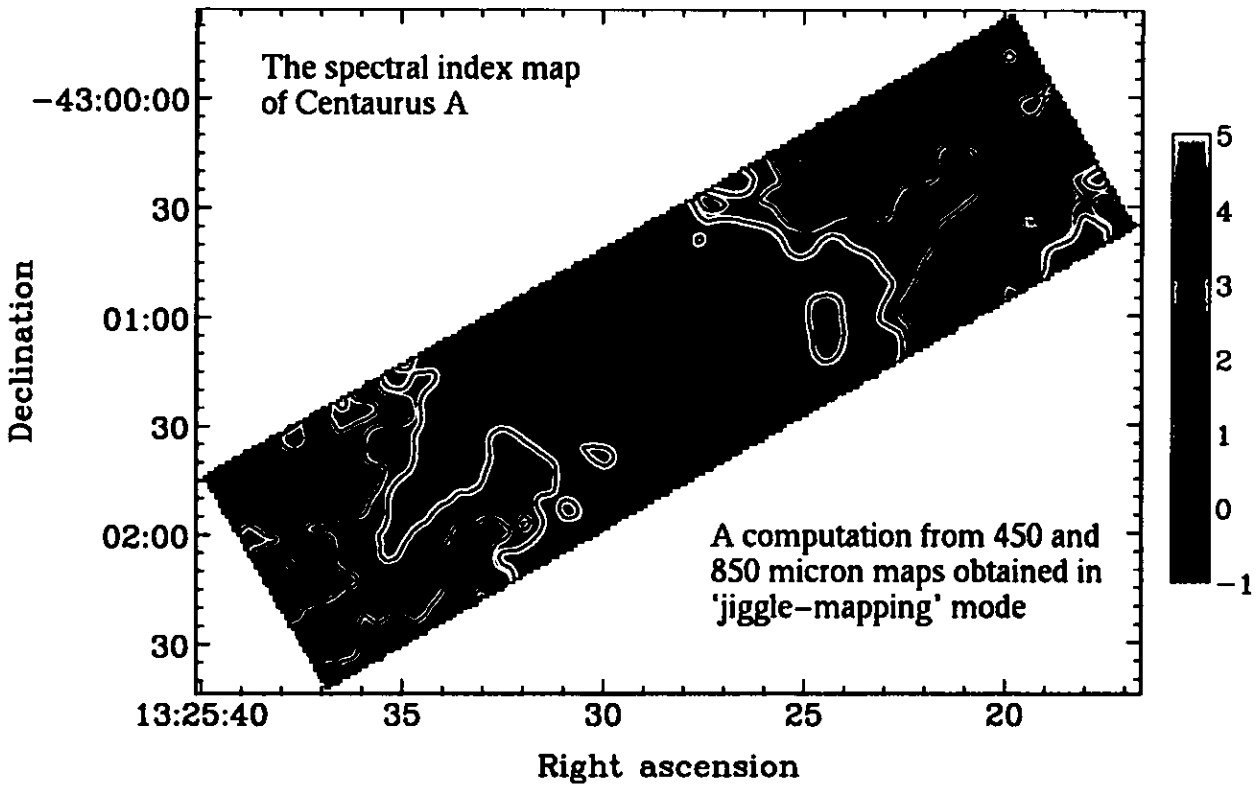

Figure 5.12: Map of the spectral index distribution of Centaurus A at submm wavelengths, derived from the 450 and 850 μm data (see Figures 5.1 and 5.2). Four regions are clearly apparent in the map: the unresolved core (blue-black) and a feature apparently representing the inner jet (green-blue) in the nuclear area; and the reverse-S-shaped *inner disc* (yellow-green-red), familiar from the intensity maps and the fainter *outer disc* (red-yellow) farther from the nucleus. Contour heights are the spectral indices 2.0 (dashed lines) and 3.0 and 3.3 (solid lines). The panel key indices correspond to the colour-coded spectral indices.

apparently representing the inner jet are distinguished. Farther from the nucleus we can discern, with progressively increasing spectral indices, the bright, reverse-S-shaped structure, familiar from the intensity maps, and the fainter outer dust, roughly corresponding to the optical dust lane (see Section 5.3.1).

The spectral index of the **unresolved core** is close to zero, consistent with the nonthermal spectrum from an AGN nucleus. These results confirm that the core source has a flat submm spectrum (i.e. $\alpha \approx 0$), which is common for BL Lacs (blazars) (see, e.g., Brown et al., 1989, and Section 5.7).

The feature which this thesis refers to as the **inner jet** is not evident on the intensity maps but is prominent in Figure 5.12 as (green-blue) areas of low spectral index to NE and SW of the nucleus. The spectral index of these areas is in the range $1.5 \leq \alpha \leq 2.5$ (see dashed contour lines). The northern extension is coincident with the inner radio jet (Clarke et al., 1992), which, as implied by the designation in this thesis, is not considered to be merely by chance. However, the observed spectral index is much higher than would be expected from extrapolation of the power-law spectrum of the radio jet itself. One possible explanation is that the submm spectrum is not a manifestation of the electron distribution of the relativistic radio jet itself (or the jet overlaid by a warm dust component), but rather of some internal mechanism (e.g. ionisation of gas) resulting from the interaction of the jet and the ISM in the inner regions of the galaxy.

Brodie et al. (1983) and others have proposed that optical jets in galaxies such as Centaurus A may be due to emission from interstellar gas that has been entrained and heated by the flow of relativistic particles from the nucleus. The entrained gas would generate free-free continuum emission with spectral index, in the optically thick case, of $\alpha \approx 2$, consistent with the observed spectral range of the inner jet $1.5 \leq \alpha \leq 2.5$.

The southern nuclear extension in the submm spectral map in this thesis is attributed to the same mechanism, though in this case associated with the fainter counter jet recently reported by Tingay et al. (1998) and Kraft et al. (2000), respectively from their high resolution VLBI radio and *Chandra* X-ray images.

A similar interaction of the jet and interstellar medium was proposed by Joy et al. (1991) based on their near-IR observation of the inner jet of Centaurus A, which manifested itself as a region of 'bluer' colour, with spectral index $1.3 \leq \alpha \leq 2.9$, coincident with the radio jet. Marconi et al. (2000) also reported a 'blue channel' coincident with the radio jet, but they attributed it to low extinction resulting from relatively low concentration of dust that has been mechanically 'evacuated' by the jet. This thesis disagrees with this interpretation as there is no sign of a deficiency of emission on the 450 μm map at this location: the inner jet feature of Figure 5.12 arises from a relative enhancement of emission at 850 μm in these locations.

The spectral index of the **inner disc** is in the range $2.5 \leq \alpha \leq 3.2$, consistent with thermal emission from dust. The lowest indices occur in an almost circular region about 30″ in radius around the nucleus; this is coincident with an area of hot molecular gas reported by Schreier et al. (1998)[3] from their *HST* observations. Emission with a steeper spectrum ($2.6 \leq \alpha \leq 3.2$, see solid contour lines) approximately traces the inner disc of brighter structures seen in the 7 and 450 μm images out to $\sim$ 90″ (see Section 5.3.2 and Figure 5.6). Farther still from the nucleus, in the fainter **outer disc** the spectral index increases to $\alpha \sim 4$. As underscored by the solid line contours in Figure 5.12, the spectral index is asymmetric about the nucleus in the inner disc region of the map: it is

[3]STScI-PRC98-14 Electronic Press Release is available at http://oposite.stsci.edu/pubinfo/pr/1998/14/pr-photos.html

somewhat flatter on the eastern part of the inner disc, indicating slightly different relative distributions of dust grains on either side of the nucleus.

If the dust seen in the maps presented in this thesis is emitting with blackbody spectral index $\alpha = 2 + \beta$ (where β is the emissivity index), the spectral index in the extended region implies that for a given temperature, the dust in Centaurus A has on average a low β., i.e. the dust is made of relatively large grains, and that its temperature is fairly cool. Furthermore, the somewhat flatter spectral index in the south-east suggests the dust in this region is made of smaller grains with moderately warmer temperatures than those in the same region in the NW. This is not surprising as the SE is reported to exhibit stronger H I emission (van Gorkom et al., 1990), weaker ^{12}C(1-0) and stronger Hα line emission compared to the NW, that led Eckart et al. (1990) to speculate that star-formation and its associated high radiation field were greater in the SE.

The uncertainty in the emissivity analysis in the spectral index map (Figure 5.12) does not permit us to quantitatively examine the effects, if any, due to diffuse "cirrus" grains in the map. The dust in the outer disc, where the emissivity index $\beta > 1.5$, may well consist of "cirrus" grains, which, as it is generally accepted (e.g. Rowan-Robinson, 1992), would have an emissivity index close to $\beta = 2$ and temperatures $15 < T < 40$ K. In fact, Eckart et al. (1990) associated the far-IR emission outside the molecular star-forming disc (i.e. radius $>\sim 90''$) with "cirrus" clouds with scale height larger than that of the molecular gas disc (c.f. Section 5.3.3); and they predicted that the submm extended emission would also originate from dust constituting "cirrus" grains as could well be the case.

5.5 Implications of the Multiwavelength Images

The submm images in this thesis demonstrate that outlying dust in Centaurus A is significantly cooler than the material in the bright elongated features within $\sim 90''$ of the nucleus. This is naturally to be expected: at larger radii the ambient radiation field heating the dust is more dilute because of the much lower density of stars (Eckart et al., 1990; Schreier et al., 1996; Marconi et al., 2000). The emission from this dust generally follows the optical dust lane.

Figures 5.6 and 5.7 showed that there are *remarkable* similarities between the appearance of Centaurus A in the mid-IR and the submm, the major *difference* being that the submm emission is seen to much larger angular distances than is the mid-IR. It follows that the warped-disc model, consisting of tilted rings of material that absorbs galactic light (Quillen et al., 1993), not only predicts structure of the colder material seen in the submm (as demonstrated in Figure 5.9) but also warmer material seen in the mid-IR, rather well, particularly for radii less than about $\sim 90''$ of the nucleus. This scenario is supported by Eckart et al. (1999), who showed that a warped structure of tilted rings explained not only the line emission in the disc of Centaurus A (Quillen et al., 1993), but also a complex absorption-line system towards the nucleus, without a need for any additional structures.

From their *ISO* 7 and 15μm images, Mirabel et al. (1999) conclude from a comparison with similar mid-IR images of the dwarf barred spiral NGC 1530 that the structure imaged in the mid-IR in Centaurus A is itself a barred spiral: the prominent emission peaks $\sim 75''$ from the nucleus at each end of the bright mid-IR and submm structures are hypothesised to be foreshortened arms twisting anti-clockwise from the outer ends of the

bar. Block & Sauvage (2000) support this proposal from their V, H, K and 15μm study of Centaurus A, noting too that the warm dust seen by ISOCAM contributes little to the extinction seen at optical wavelengths.

Kinematics is clearly important in understanding the true nature of the near-nuclear structures in Centaurus A. Mirabel et al. (1999) address these in their Figure 4, a comparison of the IR images with the CO kinematics in the form of a position-velocity (P-V) plot from Quillen et al. (1992). On this figure, they identify the strong CO feature extending from $-1'.2$, $300\,\mathrm{km\,s^{-1}}$ to $+1'.2$, $800\,\mathrm{km\,s^{-1}}$ as the bar, undergoing solid body rotation, and weaker outlying features at nearly constant velocity at larger radii as the "typical" rotation curve of galactic discs.

However, an alternative interpretation of the PV diagram is that the "bar" represents a nearly-complete, highly foreshortened, ring of material at a radius of $\sim 65''$ ($\sim 1300\,\mathrm{pc}$). In that scenario the concentrations of IR and submm emission NW and SE of the nucleus represent the ends of the ring where the optical depth is maximised. Similarly, the "EW high-velocity feature" mentioned by Mirabel et al. (1999), which they note does not fit their scenario, is readily explained by another ring of molecular material at a radius of $\sim 20''$ ($\sim 400\,\mathrm{pc}$), tilted relative to the outer ring and evident on the mid-IR images as two small extensions to the nuclear feature in PA 80° and 260°. Furthermore, the outer features of the PV diagram also have an alternative interpretation: the feature $>1'.7$ SE of the nucleus has the properties of an arc of material starting at radius of $\sim 4.6\,\mathrm{kpc}$ and ending perhaps 2 kpc from the nucleus close to the minor axis: in a normal edge-on spiral, such a feature would be interpreted as a spiral arm.

Marconi et al. (2000) also accept the bar model since its edges appear to be delineated by linear concentrations of star-forming regions seen in their Paα images, suggesting

that these delineate the shocks normally seen as dust lanes along the leading edges or the midlines of galaxy bars in optical images. However, they also noted that their data do not rule out a warped ring without a bar, as the star-formation is found in regions of the warp that are tangent to the line of sight, and if the young stars are above or inside the disc, they would indeed appear to be concentrated where the Paα emission is seen.

This thesis suggests the latter interpretation is more plausible for the following two reasons. First, the same elongated distribution of Paα emission regions, which Marconi et al. (2000) show to coincide precisely with the elongated mid-IR ridge that passes just south of the nucleus, is equally coincident with the dense, narrow, optical dust lane that passes south of the nucleus in Figure 5.5. Since this is the *only* feature of the bright central complex (apart from the nucleus itself) that is potentially identifiable with an optically-visible feature, we suggest that it is not in fact part of the near-nuclear complex at all, but, as suggested by the models of Quillen et al. (1992), a manifestation of an outlying fold or ring in the warped disc.

Second, it is noted that the bar-shocks traced by dust in early-type field spirals are asymmetric about their nuclei, since they lie in the leading edges of the bars, while those in late type systems are centred in the bars. However, the Paα emission regions in Figure 13 of Marconi et al. (2000) pass by several arcsecs south of the nucleus from the SE to west of the nucleus. This is not what would be expected of a shock in a bar in a field spiral, but more the distribution to be expected if the star-forming regions are associated with the trailing dust lanes in a typical spiral arm, or in this case the dusty rings postulated by Quillen et al. (1992).

Therefore, the combined evidence to date from the CO kinematics, the mid-IR images, the bright and faint submm features and the Paα images supports the warped-disc model

of Quillen et al. (1992) rather than indicating the presence of a true bar, and may even represent spiral structure in the dust lane of Centaurus A.

One of the attractions of the bar scenario for both Mirabel et al. (1999) and Marconi et al. (2000) is its expected utility as a mover of material from larger to smaller radii in the disc in order to fuel the AGN. However, since the association of barred structure with the presence of an active nucleus in field galaxies, though long looked for, is marginal at best (cf., for example, Ho et al. (1996) and references therein), the presence of the AGN cannot be taken as an argument for the reality of the putative bar. Not having a bar to fuel the active nucleus is not too bad a loss; e.g. recent work by Duschl et al. (2000) suggests that viscosity in a thin gas plane may also provide an efficient AGN fuelling mechanism.

5.6 The Extended Emission Temperature and Dust Mass Estimates

This thesis has shown that the central source is unresolved and has a flux density per beam at least 40 times brighter and a spectrum markedly flatter than the surrounding emission from the dust lane; i.e. the central source is clearly distinct from the extended emission (c.f. Sections 5.3, 5.4 & 5.5 and Figures 5.4 & 5.12). The core flux densities from 850 to 7μm are presented in Table 5.1, together with integrated flux densities determined for two regions of the extended emission from the dust lane: (1) an ellipse of $60'' \times 180''$ *minus* the core measurement and (2) an elliptical annulus of $(120'' - 60'') \times (450'' - 180'')$. The far-IR flux densities are archival *IRAS* data for Centaurus A that were re-analysed using the HIRES facility to extract the best possible spatial resolution

Table 5.1: Submm to Mid-IR Fluxes of the Centaurus A Core and Extended Emission

Filter	Frequency (GHz)	Core (Jy)	*Inner disc* (Jy)	*Outer disc* (Jy)
SCUBA 850	350	8.1 ± 0.8	2.7 ± 0.4	3.4 ± 0.5
SCUBA 750	407	8.1 ± 1.6	...	...
SCUBA 450	667	7.9 ± 0.8	16.9 ± 3.2	22.6 ± 5.2
SCUBA 350	866	7.7 ± 1.9	...	...
IRAS 100	3000	8 ± 2	119 ± 20	181 ± 36
IRAS 60	5000	8 ± 2	96 ± 15	77 ± 15
IRAS 25	12000	...	15 ± 2	6 ± 1
ISOCAM 15	20000	1.2	10.4	...
IRAS 12	25000	...	11 ± 2	6 ± 1
ISOCAM 7	42857	0.7	9.4	...

In columns four and five, the integrated fluxes presented are determined respectively in an ellipse of $60'' \times 180''$ minus the core flux and in an elliptical annulus of $(120'' - 60'') \times (450'' - 180'')$. Core fluxes have not been subtracted from the integrated fluxes for *IRAS* 100 and 60 filters as no reasonable estimate of the core fluxes at these wavelengths could be estimated from the present data. In the case of the 100 and 60 μm core fluxes, the data listed are an extrapolation of the submm core SED ($\alpha_{81\,\mathrm{GHz}}^{877\,\mathrm{GHz}} = -0.01$, $S_\nu \propto \nu^\alpha$) to 60 μm (5000 GHz), as the HIRES beams are very large ($50''$ to $90''$) so that it was impossible to isolate the core fluxes from the extended emission.

and to ensure the same registration of the regions from which integrated flux densities are determined. The ellipse and annulus are denoted respectively as the *inner disc* and *outer disc*, as the two regions have different submm continuum morphology and spectral index distributions (see Sections 5.3.2 & 5.4). The SED for the two extended regions are plotted in Figure 5.13, and temperatures as well as dust masses determined for the emission from these regions are discussed below.

The compact core is unresolved on the submm and *ISO* mid-IR images (FWHM $< 8''$ at 450 μm and $< 4''$ at 7μm, see Section 5.7). In the case of the *IRAS* data, HIRES beams are very large ($50''$ to $90''$) so that the core extent is impossible to constrain and its flux not easily separable from that of the extended emission. Therefore, the 100 and 60μm core fluxes listed in Table 5.1 are an extrapolation of the submm core SED ($\alpha_{81\,\mathrm{GHz}}^{877\,\mathrm{GHz}} = -0.01$, $S_\nu \propto \nu^\alpha$) to 60μm (5000 GHz); and, for the *inner disc IRAS* fluxes

listed in the table, the integrated flux measurements were simply subtracted from these extrapolated numbers. A further discussion of the SED of the submm core in Centaurus A is carried out in Section 5.7.

The integrated submm to far-IR flux densities are fit by a two-component optically thin greybody of the form

$$S_\nu = (1 - \exp(-\lambda_o/\lambda)^\beta)[\Omega_1 B_\nu(T_1) + \Omega_2 B_\nu(T_2)], \tag{5.3}$$

where S_ν is the observed flux density at frequency ν, Ω the solid angle for the greybody component, $B_\nu(T)$ the Planck function at temperature T, λ_o the wavelength at which the optical depth is unity and β the emissivity index of the grains. First, a 12 and 40 K two-component greybody with dust emissivity index of 1.3 fits the data for the *inner disc*, and secondly, a 12 and 30 K greybody with dust emissivity index of 1.6 fits the data for the *outer disc* (c.f. Figure 5.13). These fits, in particular the derived relative emissivities and temperatures, are consistent with the spectral index maps, showing that the average dust temperature decreases from the galactic core outwards. Unsurprisingly, these temperatures are also consistent with the 42 and 32 K determined by Eckart et al. (1990) from their 50 and 100 μm *IRAS* flux densities alone, as well as the average $\sim$ 40 K determined by Unger et al. (2000) from their 40 to 100 μm *ISO* LWS maps of the *inner disc* region.

The mass of emitting dust M_d is derived as in Section 1.3.1. It is assumed that values of the grain mass absorption coefficient are $k_\mathrm{d}^{450\,\mu\mathrm{m}} = 0.25\,\mathrm{m^2 kg^{-1}}$ and $k_\mathrm{d}^{60\,\mu\mathrm{m}} = 3.3\,\mathrm{m^2 kg^{-1}}$ (e.g. Hildebrand, 1983), yielding dust masses of $2.5 \times 10^4 \mathrm{M}_\odot$ for T = 40 K and $9.6 \times 10^5 \mathrm{M}_\odot$ for T = 12 K in the *inner disc* and dust masses of $4.9 \times 10^4 \mathrm{M}_\odot$ for T = 30 K

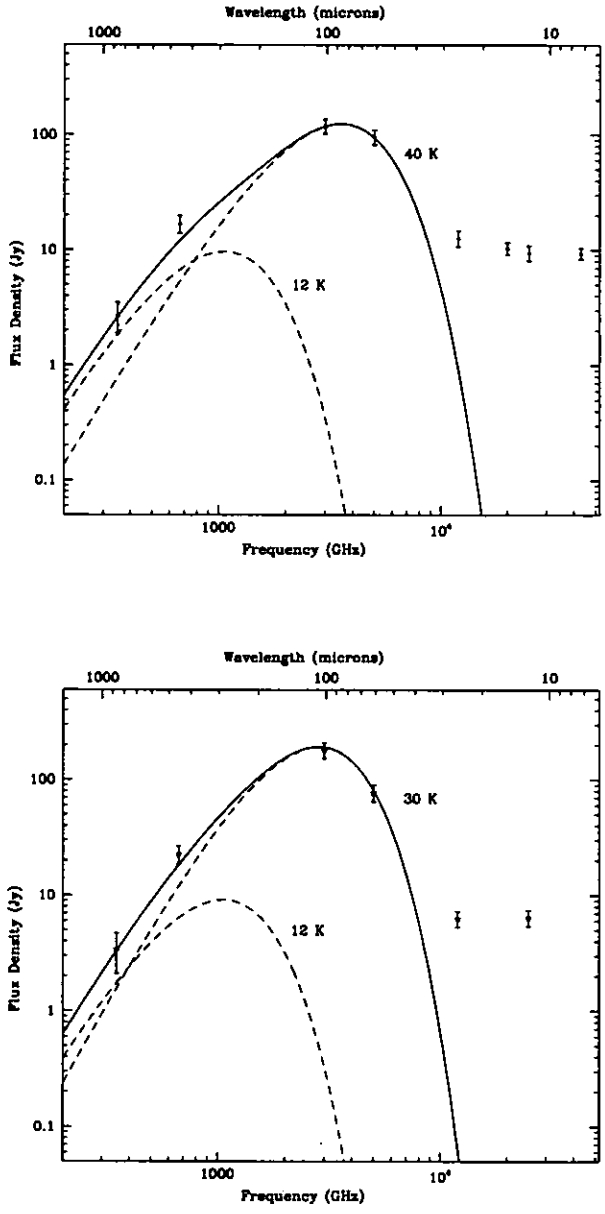

Figure 5.13: Integrated fluxes in two annuli centred on the core of Centaurus A. The upper frame for the *inner disc* of $60'' \times 180''$ minus the core flux and the lower frame for the *outer disc* annulus of $(120'' - 60'') \times (450'' - 180'')$. The submm to far-IR data points are fit by two component optically thin greybodies of temperatures 12 and 40 K with dust emissivity index of 1.3 for the *inner disc* and 12 and 30 K with dust emissivity index of 1.6 for the *outer disc* annulus.

and $1.2 \times 10^6 M_\odot$ for T = 12 K in the *outer disc*. The total mass for the dust that emits from the far-IR through the submm wavelength is then $9.9 \times 10^5 M_\odot$ and $1.2 \times 10^6 M_\odot$, respectively in the *inner disc* and *outer disc*, giving an overall total of $2.2 \times 10^6 M_\odot$ for the dust lane region of the galaxy observed in this thesis (i.e. radii $< 225''$ or ~ 4.5 kpc).

5.7 The Unresolved Core: Radio to Optical SED

Using the highest resolution SCUBA and *ISO* images, the extent of the compact core is constrained to $8''$ in the submm and $4''$ in the mid-IR respectively from the 450 and 7 μm observations, i.e. the core is indeed unresolved, as would be expected if it is entirely a manifestation of the unresolved central radio source (cf. Kellermann et al., 1997). Recent near-IR and optical size constraints, the first-ever at these wavelengths, ($< 0''.2$ at 2.2 μm and $< 0''.1$ at .8 μm) by Marconi et al. (2000) are also consistent with the submm nuclear emission size upper-limits.

In Figure 5.14 are plotted the fluxes of the core source for observations ranging from radio (1.6 GHz) through submm 850 and 450 μm (450 and 677 GHz) imaging data, other submm measures from Hawarden et al. (1993), the *ISO* 15 and 7μm results from Mirabel et al. (1999) and H and J band near-IR values and optical I and R fluxes from Marconi et al. (2000). The core spectrum is self-absorbed below 30 GHz and very flat to higher frequencies, up to about 1000 GHz: with $\alpha_{81\,\mathrm{GHz}}^{877\,\mathrm{GHz}} = -0.01$ ($S_\nu \propto \nu^\alpha$, see Figure 5.14). A flat spectrum in this wavelength regime is common for BL Lacs (blazars). Hawarden et al. (1993) and Kellermann et al. (1997) determined a *very* flat nuclear mm-to-submm spectrum in the core of Centaurus A, attributing it to a low-luminosity blazar, as first suggested by Bailey et al. (1986) from near-infrared polarimetry. Hawarden et al. (1993) suggested that the flat mm-to-submm is a characteristic of low-luminosity blazars (and/or

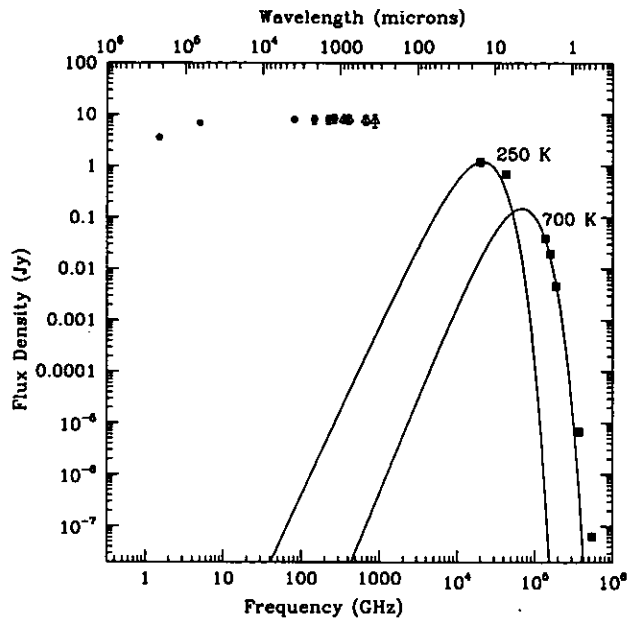

Figure 5.14: The spectral energy distribution of the central core in Centaurus A. The open triangles indicate the SCUBA data points, while the solid squares and circles respectively indicate data as cited by Hawarden et al. (1993) and Marconi et al. (2000). The two curves represent thermal emission from warm dust with temperatures of 250 and 700 K with an emissivity index, β, of 1.3.

jet sources at a large angle to the line of sight), which has been supported by observations of NGC 4374, another low-luminosity AGN (Leeuw et al., 2000, see Chapter 4).

While a very flat spectral index is also consistent with free-free emission ($\alpha = -0.1$) from ionised gas in star-formation regions, Hawarden et al. (1993) showed that this is highly unlikely in the case of Centaurus A. This has been confirmed by high resolution VLBA observations by Kellermann et al. (1997), which set lower limits on the core brightness temperature of 10^{10} K, thus excluding free-free emission from star-formation as a possible contributing factor.

Therefore, the very flat mm-submm spectrum in the core of Centaurus A is indicative of synchrotron emission, probably from the *base* of a jet, perhaps in the standing shock (e.g. Gear et al., 1985). In terms of the BL Lac/FR I unification scheme, a misaligned

BL Lac object in the core is consistent with the FR I morphology that is seen in large-scale radio maps of Centaurus A.

Marconi et al. (2000) concluded that the optical emission, and some fraction of the near-infrared, from the core source in Centaurus A could also be attributed to non-thermal emission from an AGN, as in the BL Lac scenario noted above, while the rest of the near-IR emission is from warm, circumnuclear dust at $\approx 700\,\mathrm{K}$. Indeed, the near- to mid-IR emission in the core of active galaxies is usually accounted for by thermal emission from dust heated by an AGN (e.g. Rieke & Lebofsky, 1981), while the decline in the SED at $\lambda < 2\,\mu\mathrm{m}$ is ascribed to sublimation of the dust close to the source (Sanders et al., 1989). The data from Marconi et al. (2000) are plotted in Figure 5.14 and a 250 K greybody (representing a cooler component of the circumnuclear dust) is fitted to the mid-infrared ISOCAM core fluxes.

5.8 Conclusions

The SCUBA 850 and $450\,\mu\mathrm{m}$ images in this thesis show that the submm continuum morphology and spectral index distribution of Centaurus A comprise:

1. **The Nucleus** and associated structures: A distinct, unresolved, flat-spectrum AGN core is attributed to a low-luminosity blazar, plus a circumnuclear structure, including, to the northeast and southwest, areas of low spectral index which it is suggested arises from free-free emission in ionised gas entrained in the nuclear outflow.

2. **Inner disc:** A prominent, elongated feature that may be a circumnuclear ring (or bar) extends across the centre of the galaxy out to a radius of $\sim 90''$. It contains

considerable real structure, including concentrations of emission towards its ends and a reverse-S-shaped twist; this structure appears reflected about the nucleus. The details of this structure are very similar indeed to what is seen on mid-IR *ISO* images, so the cooler dust seen in the submm is very closely co-extensive with the much warmer material (transiently heated by UV-photon absorption) seen at 7 and 15 μm, and which establishes that the *inner disc* is a locus of vigorous star formation. It is also a strong source of CO emission with kinematics consistent with a ring or rings of gas around the nucleus, rather than a bar, as has been suggested elsewhere (Mirabel et al., 1999).

3. **Outer disc and outlying dust features:** Low-level emission, at least some of which comes from the foreground material in the prominent optical dust lane, extends to the eastern, and probably to the western, end of the submm maps. It traces the clockwise twist of the optical feature.

   Some of the observed low-level emission does *not* coincide with optically-visible dust. The deep SCUBA images are, for the first time, showing the direct detection of emission arising from dust that is in the far side of the galaxy, overlaid and obscured by the stellar component of Centaurus A, and thus not seen in the optical.

A warped-disc model consisting of tilted rings (Quillen et al., 1993) predicts the structure of the warmer and colder material, especially in the *inner disc*, rather well. It appears that in this vicinity the IR and submm images to a large extent reveal the same material; however, at larger radii, the dust is cooler because it is immersed in a much less intense stellar radiation field. Alternative arguments are presented by Mirabel et al. (1999) and Block & Sauvage (2000), who interpret the mid-IR (and brighter submm)

structures as a true barred spiral.

Using the continuum integrated fluxes from far-IR through submm wavelengths a total dust mass of $2.2 \times 10^6 M_\odot$ is derived within a radius of 225″ of the nucleus of Centaurus A. About 45% of the dust mass is in the star-forming *inner disc* within about $< 90''$ of the nucleus.

Chapter 6

Properties and Outflows of Cold Dust in M 82

6.1 Introduction

Massive ejections of gas and dust originating in galactic nuclei have been observed at scales of a few kpc in optical emission lines, submillimetre molecular lines, radio continuum emission and soft X-rays (e.g. Watson et al., 1984; Devine & Bally, 1999). One explanation for the outflows is that a high supernova rate in the galactic nucleus heats up the surrounding gas to high temperatures and sound speeds exceeding the escape velocity of the galaxy, creating a *wind* that expands outward from the galaxy (Chevalier & Clegg, 1985). The wind entrains cosmic rays, warm and cool gas, as well as cool dust, making the outflow visible in many wavebands. The outflows are usually oriented along the minor axes of the galaxies and are thus most easily observed in edge-on galaxies.

Figure 6.1 shows detailed, filamentary outflows of the H_α winds of the nearby galaxy M 82, that were imaged in B (0.45 μm), V (0.5 μm) and H_α (0.65 μm) filters during the

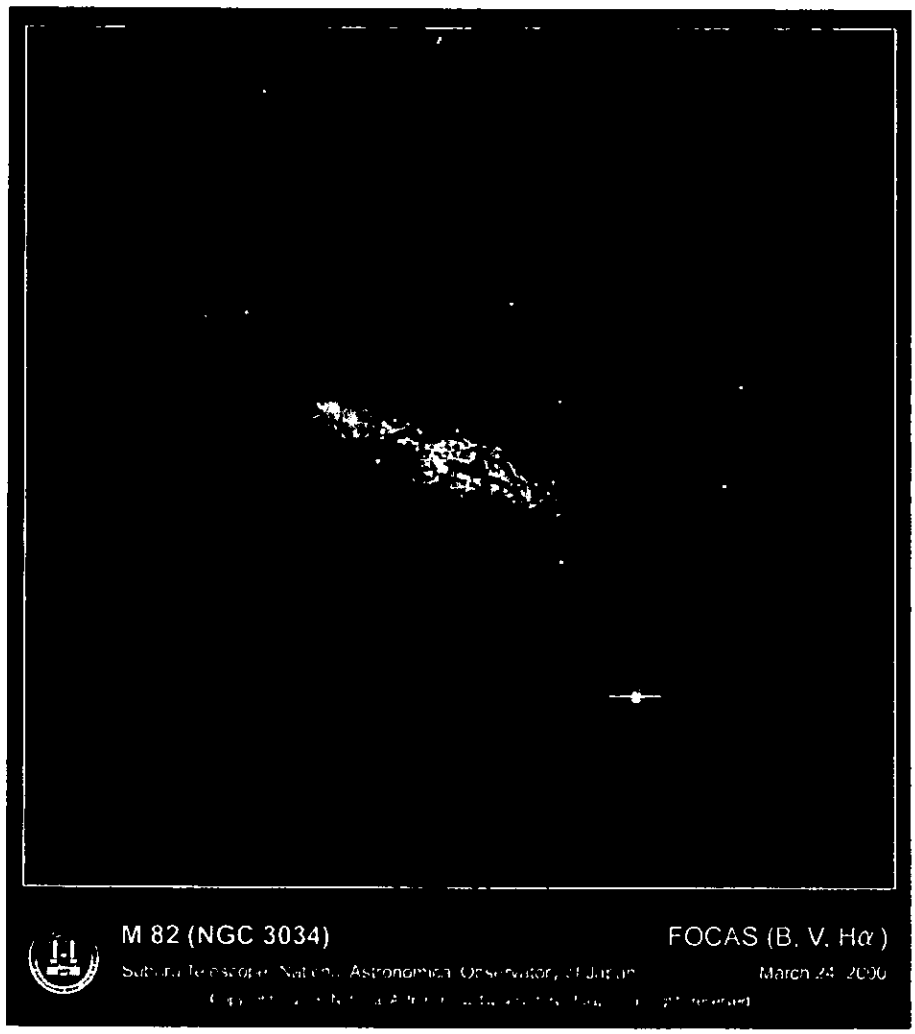

Figure 6.1: The H_α outflows from M82 as imaged in B (0.45μm), V (0.5μm) and H_α (0.65μm) filters during the commissioning of Subaru's Faint Object Camera and Spectrograph. The field of view is about 6′ in diameter and centred on the position of the galactic nucleus. The image is provided courtesy of the Subaru Telescope.

commissioning of the Faint Object Camera and Spectrograph on the Subaru Telescope, provided courtesy of the National Observatory of Japan. As described above, it is thought that this outflow is being driven by the copious formation of massive stars (or a starburst) and subsequent explosions of supernovae. The starburst outflow not only provides the ejection mechanism for the material from the galactic nucleus, but also heats the gas and ionises the hydrogen, causing it to glow with the red light of H_α emission line.

M82 (NGC3034) is a favourite object in which to investigate the physical association

between galactic nuclei and large-scale outflows. The galaxy is edge-on with an inclination of about 10° at position angle 72° and is classified as IrrII. At an estimated distance of 3.25 Mpc (Tammann & Sandage, 1968), it has optical dimensions of $11'.2 \times 4'.3$, i.e. $\sim 10.8 \times 4.1$ kpc. The nuclear region, within $4' \times 2'$ about the major axis of the galactic disc, has numerous point sources or emission concentrations, some of which originate from supernovae and massive star clusters, that have been detected from the X-ray to radio wavebands. Layers of dust filaments laden these inner regions producing severe optical extinction and copious infrared to submm re-radiated emission.

A spectacular natural-colour composite, optical-band photograph of the inner region of M 82 obtained with the *Hubble Space Telescope*, courtesy of Dr. Richard de Grijs at Cambridge University, is displayed in Figure 6.2. This detailed *HST* image shows more than 100 compact groupings of about 10^5 stars in very bright star clusters as white dots sprinkled throughout M 82's central region, the prominent dust lanes that crisscross the disc – including a huge dark-cloud of dust just above the centre of the picture, knotty filaments of nitrogen and hydrogen gas (of Figure 6.1) in a strong galactic wind that is clear below the centre and to the right of the image, and many other regions of varying star-formation environments in the nuclear parts of this galaxy (see, e.g., Section 6.4 or de Grijs, 2001). The huge clusters of massive stars, numerous X-ray and radio detected supernovae, gas concentrations, optically-dramatic dust filaments, galactic winds and other active nuclear features have been attributed to a large burst of star formation 10^7 to 10^8 years ago, that was probably triggered by a tidal interaction with the nearby galaxy M 81 (see, e.g., Förster Schreiber, 2000, for a recent review).

It is noted that up until the early 1960s, it was believed that the chaotic optical morphology and extended H_α emission in M 82 was caused by a single massive explosion

at the centre of the galaxy (e.g. Lynds & Sandage, 1963). It was only after the discovery of the many supernova remnants, clusters of massive stars and large amounts of outflowing molecular gas, did it emerge that the nuclear morphology and outflows were a result of the star-formation and subsequent explosions of supernovae.

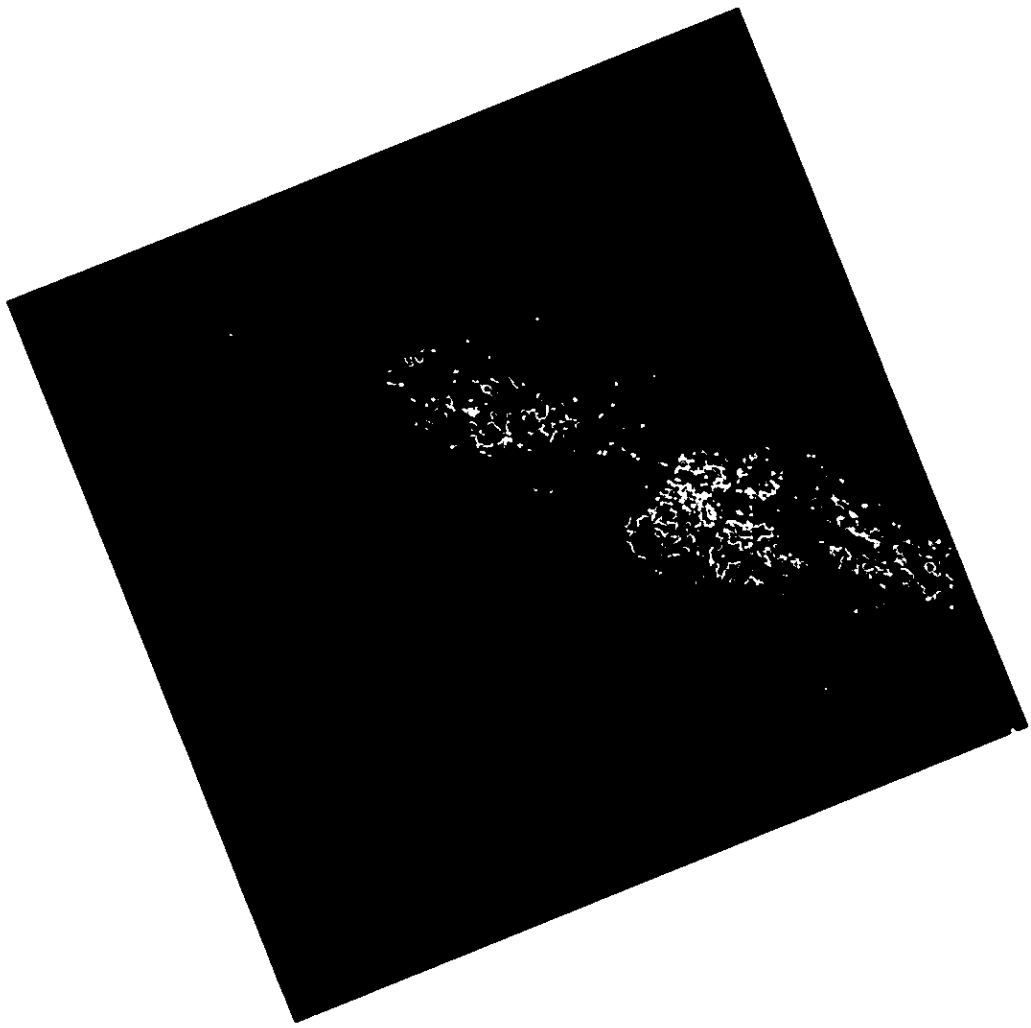

Figure 6.2: The natural-colour composite of the central region of M 82 reconstructed from photographs obtained with the *HST*'s Wide Field and Planetary Camera 2 in blue, green and red filters, courtesy of NASA and ESA. The image shows more than 100 compact star clusters as very bright, white dots sprinkled throughout the central region; prominent dust lanes that crisscross the disc; and knotty filaments of hydrogen and nitrogen gas in a strong galactic wind that is clear below the centre and to the right. These features together manifest varying star-formation environments in the nuclear parts of this galaxy. The field of view is about $2'.5 \times 2'.5$.

The proximity of this galaxy makes it possible to observe the region of interaction

between the star-formation regions and the halo, including expanding radio shells and "chimneys" that are producing a clearer picture of the localised driving mechanisms for the outflows (e.g. Wills et al., 1999). The proximity also allows the detections of *low-level* emission in the halo and consequently the determination of the amounts and possible origin of material that results in this emission (e.g. Seaquist & Clark, 2001). Studying the contents and interactions between the star-formation regions and the halo is important for understanding their role in the evolution of M 82 and may provide clues to general galaxy evolution as well as details of the composition of the intergalactic material.

This chapter focuses on the SCUBA maps of the copious submm re-radiated emission that results from the dust-laden, nuclear disc, as well as large-scale, low-level emission that is associated with the outflows in the halo of M 82. Submm continuum observations of the dusty central regions in M 82 were previously obtained with UKT 14 by Hughes et al. (1990, 1994) and later with SCUBA by Leeuw et al. (1998) and Alton et al. (1999). The current study was intended to extend these previous imaging submm observations in spatial extent, sensitivity and to all the four submm wavelengths available with the SCUBA array (see Section 6.2). The study includes a co-addition of data observed by other astronomers and mined from the SCUBA Data Archive, as well as exploratory observations that were obtained with the 180″ chop throw rather than the 120″ chop that is customarily used at the JCMT for mapping extended emission.

The co-added data produce the deepest submm continuum maps yet of M 82, in which low-level emission is detected out to 1.5 kpc for the first time in the submm continuum of this galaxy. The deep maps are used in a detailed morphological study of the nuclear and large-scale detections (see Sections 6.3 and 6.5), including a focused comparative analysis to optical (see Section 6.3.1) and high-resolution CO (1-0) (see Sec-

tion 6.3.2) morphology. The maps are also used in the computation and investigation of the first submm spectral index distribution of the high-brightness, nuclear region (see Sections 6.4 and 6.5). These observational results are used in the discussion of the origin and structure of submm continuum morphology and spectral index distribution of M 82 and reviewed in the context of relevant interpretations by other researchers, including those who use data from other wavelengths (see Section 6.5). In particular, (a) the commonly assumed interpretation that the double emission peaks that are seen in the mm to infrared continuum are due to emission from the edges of an inclined, dusty-molecular torus is challenged (see Section 6.5.1), (b) an analytical review of CO results is undertaken to assess if CO emission may significantly contaminate the continuum observed in SCUBA filters (see Section 6.5.2), and (c) a morphological comparison is conducted to check whether the localised outflows that are reported in radio and SiO maps respectively by Wills et al. (1999) and García-Burillo et al. (2001) can be seen in the SCUBA maps (see Section 6.5.3). Furthermore, preliminary analyses are conducted to investigate (i) whether Maximum Entropy Method deconvolution can improve the SCUBA resolution of standard JCMT sources (see Section 6.6.1) and the deep submm maps of M 82 (see Section 6.6.2), and (ii) if observations with the 180″ chop throw can improve the detection of the submm continuum in M 82 (see Section 6.6.3), as the large throw was designed to chop clear of any unknown low-level emission. Finally, the overall implication of the results are discussed and possible future work is outlined (see Section 6.7). It is emphasised that the results in this chapter are presented as work in progress, and therefore some of the conclusions are rather *preliminary*.

6.2 Observations

SCUBA 350, 450, 750 and 850 μm imaging observations of M 82 were obtained with the telescope pointed at the 2.2 μm infrared nuclear peak of the galaxy using positions from Dietz et al. (1986). Jiggle mapping observations were conducted with the secondary chopping in azimuth at 7.8 Hz and with a throw of 120″, the recommended maximum chop when using SCUBA on the JCMT. On a separate occasion, a chop throw of 180″ was used in an attempt to chop clear of any extended emission. The imaging observations employed the common 64-point jiggle pattern with a 3″ offset between each position, giving fully sampled images with both arrays.

Because M 82 has been a popularly observed source with SCUBA, additional maps that were obtained with a chop throw of 120″ by other observers were mined from the SCUBA Data Archive in order to co-add the related data and maximise the signal-to-noise in the final maps. Following JCMT guidelines by Sandell (1998), data sets from the SCUBA Archive were separately flux calibrated and corrected for JCMT pointing errors and then co-added, with each observation being weighted according to its relative integration time and the noise in the map. The 450-850 μm dual mapping wavebands have been used more commonly than the 350-750 μm combination, and therefore the archival maps constitute about 85% and 35% of the respective co-added, total-integration time for the 450-850 μm and 350-750 μm dual maps.

The imaging data analysis for all maps was undertaken using SURF software and standard SCUBA data reduction techniques (see Chapter 2). All the data were calibrated using instrumental gains determined from nightly beam maps of Mars and Uranus, primarily, or the JCMT secondary calibrators. Unfortunately, calibration observations of

the planets or the JCMT secondary calibrators were not obtained with the 180″ chop throw at the time. Instrumental gains determined from observations with 60″ and 120″ chop throws can differ by as much as 20% (e.g. Sandell, 1998). Therefore, some gain difference is also expected between observations with the 120″ and 180″ chop throws. For this thesis, the observations from the 180″ chop throw data set are presented with calibrations determined from instrumental gains of the 120″ chop throw, without any attempt to compensate for the uncertainty introduced by the likely gain difference of the 120″ and 180″ chop-throws. Those data are displayed with an emphasis *only* on the morphology seen in the maps, until proper 180″ chop throw instrumental gain observations, or 120″ and 180″ throw gain ratios, are available and these maps can be rigorously calibrated.

There is also a calibration problem with the 750μm data of the 120″ chop throw. This is manifested in 'noisy' maps with a morphology that has no resemblance to the other submm maps of M 82. No obvious cause of this has currently been found. Alton et al. (1999) reported a similar (unexplainable) 750μm calibration problem evident in their spectral energy distribution (SED) diagram. These 750μm data are not presented in this thesis and are being investigated by the JCMT staff. The SCUBA filter-drum has been inoperable since the time of these observations, operating only at 450 and 850μm, and so the problem is awaiting SCUBA to be restored to full filter configuration.

6.3 The General Submm Continuum Morphology

Figure 6.3 shows the 850 and 450 μm co-added maps of M 82 that were obtained with a chop throw of 120″ in jiggle mapping observing mode, respectively at 14″.5 and 8″.5 resolution and about 8 and 110 mJy/beam sensitivity. Figure 6.4 displays the 350 μm

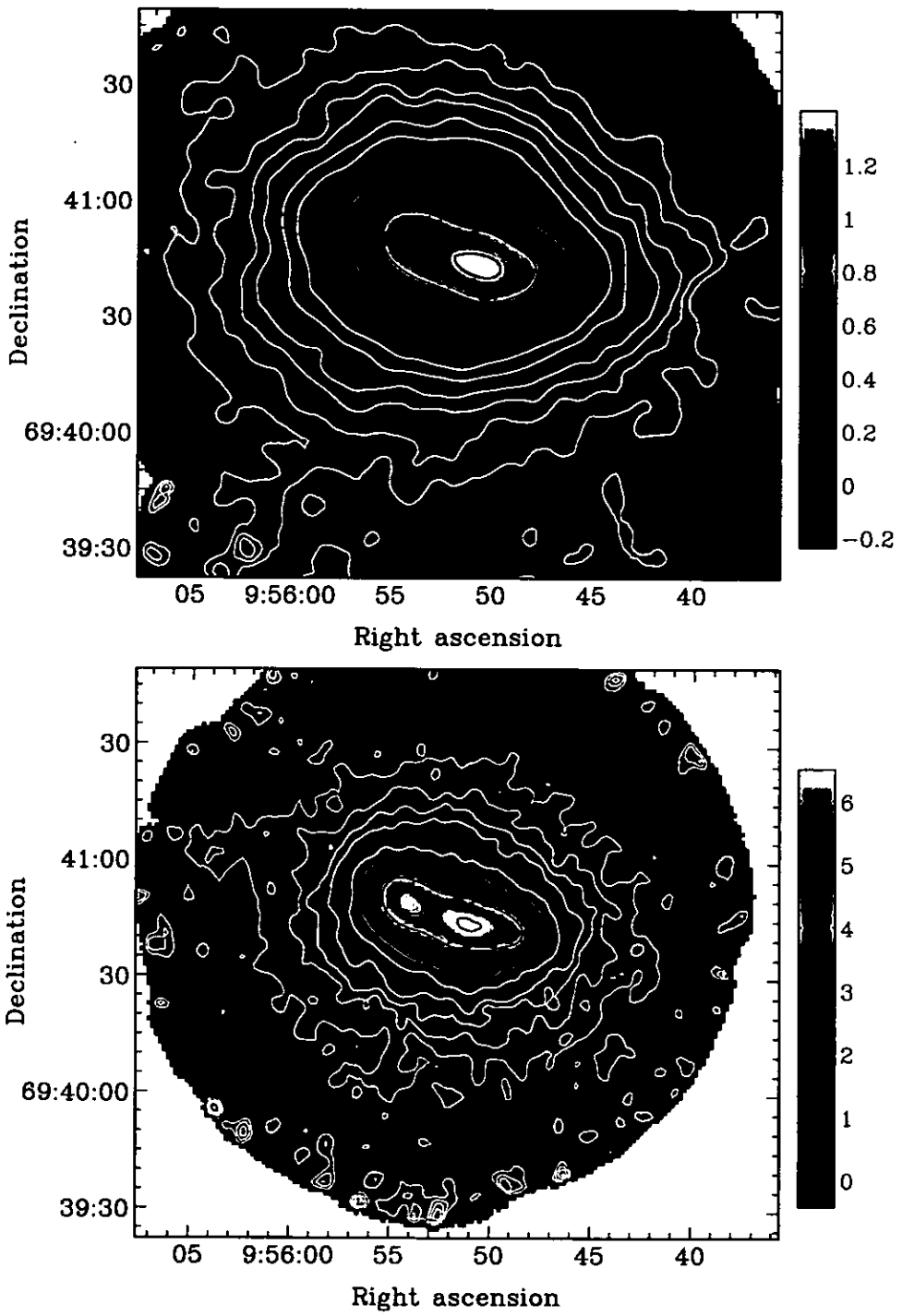

Figure 6.3: Deep maps of the 850 (top panel) and 450 μm (bottom panel) continuum emission centred at the near-infrared nucleus of M 82 and obtained with a 120″ chop throw. The 850 and 450 μm contours on the respective maps are [16, 32, 48, 64, 96, 128, 200, 300, 400, 600, 800, 1000, 1175, 1350] and [225, 450, 900, 1450, 2000, 3000, 4000, 5000, 6000, 6800] mJy/beam; the rms uncertainties are about 8 and 110 mJy/beam. The keys are colour-coded intensities in Jy/beam, and the X and Y axes are J2000 coordinates.

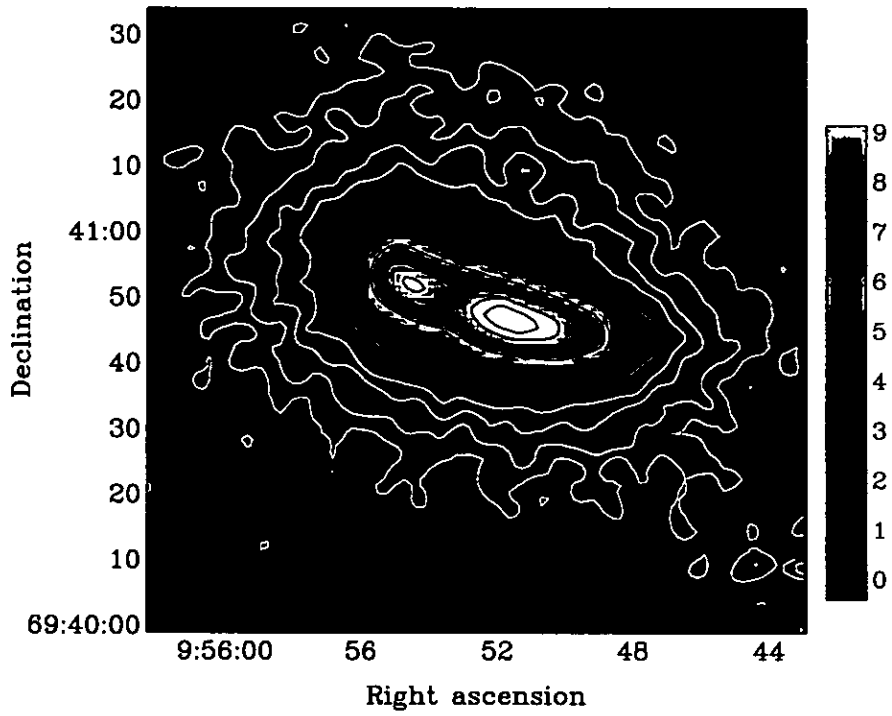

Figure 6.4: Deep 350 μm continuum emission maps centred at the near-infrared nucleus of M 82 and obtained with a 120″ chop throw. The contours are 650, 1050, 1500, 1950, 2000, 3000, 4000, 5000, 6000, 8000, 9000 and 10000 mJy/beam, and the rms uncertainty is at least 325 mJy/beam. The key is colour-coded intensities in Jy/beam, and the X and Y axes are J2000 coordinates.

image, that was also obtained with a chop throw of 120″ in jiggle mapping observing mode. This has a sensitivity of 350 mJy/beam and the highest submm resolution of 6″.7. The chop throw of 120″, that was used to obtain the maps in Figures 6.3 and 6.4, is the standard recommended SCUBA chop for observing extended emission (cf. maps of the 180″ chop throw that are shown in Figures 6.12 and 6.13).

The 850 μm image has a single emission peak that is centred about 9″ west of the galactic nucleus, while the 450 and 350 μm maps have two emission peaks centred about 10″ and 6″ respectively east and west of the nucleus along the galactic disc. The peak in the west is slightly elongated along the galactic disc and is brighter than the eastern peak, showing east-west asymmetry about the nucleus. The overall extended morphology has an elliptical shape with the major axis position angle of 72°, i.e. roughly the same

as the galactic disc in the nuclear region. This general morphology is similar to previous continuum observations at mm (e.g. Kuno & Matsuo, 1997; Thuma et al., 2000), submm (Hughes et al., 1994; Leeuw et al., 1998; Alton et al., 1999) and mid-infrared (Telesco et al., 1991) wavelengths, as well as to CO line transitions (e.g. Nakai et al., 1987) and H_α (e.g. Devine & Bally, 1999) observations of comparable resolution.

It is noted that although the maps presented in Figure 6.3 have similar features to those in published submm continuum maps by Hughes et al. (1994) and Alton et al. (1999), the very sensitive 850 μm map presented here also shows that the 850 μm emission (that is expected to be from cold dust) extends by at least 10″ ($\sim$ 160 pc) radius farther into the halo than detected by those authors. Furthermore, the maps presented in this thesis show that the 850 μm emission traces the CO(2-1) emission very well, contrary to claims by Thuma et al. (2000) that the CO(2-1) emission is more extended than the cold dust emission in M 82, and therefore made the galaxy exceptional in this regard.

6.3.1 Submm vs. Optical Morphology

First, it is noted that the detailed Subaru Telescope and *HST* photographs shown in Section 6.1 or other reasonable optical images of M 82 are not currently available in a suitable format to be electronically overlaid with the SCUBA images for direct spatial comparison in this thesis. The electronic maps are essential because the structure in the optical image is rather complex (e.g. de Grijs, 2001) and spatial comparison of features in the respective wavebands is best done with the maps overlaid in sky coordinates. The following preliminary points are made about the submm versus optical morphology based on overlays of scaled paper copies of the relevant maps. An analysis of the submm versus optical morphology is important because the complex optical morphology that is seen in

M 82 is thought to result from obscuration of optical light by dust grains that re-radiate in the infrared to submm wavelengths.

The submm morphology of M 82 generally resembles the optical picture in that the nuclear emission has an apparently elliptical shape whose major axis is clearly aligned with that of the galactic disc at a position angle of $\sim 72°$. However, the submm morphology is much smoother than the optical, and the huge dark dust cloud that is slightly to the left of centre and the prominent filamentary dust lanes that run north-south in the optical picture (see Figure 6.2) are not obvious in the submm continuum. In fact, the submm emission has a brightness peak west of the nucleus, i.e. on the opposite end of the galactic centre to the dark dust cloud. The lack of correspondence between the very dark optical clouds and filaments with bright submm emission suggests that these optical features are due to obscuration by cool dust grains that are in the near side of the galaxy and at large distances from the nuclear region, where they are heated by a dilute stellar radiation field. Therefore, though they evidently have enough column densities to obscure optical light in the line of sight, they only emit very low-level submm emission that shows no striking features in the current maps.

One explanation for the submm low-level continuum having a relatively smooth morphology is that, because this emission is optically thin, the detected radiation at a particular submm wavelength represents the total emission from the entire galactic column of dust in the line of sight. This is different from the optical morphology of dust because the dust is typically seen *obscuring* stellar light, and therefore only the dust in certain spatial stratifications (usually the foreground) of the line-of-sight columns is observed. In other words, morphology due to spatial-depth or stratification of similar dust grains that are heated by a dilute radiation field is often more obviously seen in optical obscu-

ration than in submm emission. These morphological effects will of course depend on the sensitivities of the instruments used.

Deep *HST* images of M 82 show optical morphology that is complex, with visual extinction values (A_V) that range from about 3 to 25 (e.g. Alonso-Herrero et al., 2001) across the galaxy. The dust lanes must vary not only in their geometric structure but also in their heating mechanisms and composition. Clearly, a more quantitative spatial-correspondence and optical-depth analyses (and radiative modelling) of the submm versus optical images are needed to make more definite assertions about the origin of any of the features noted here.

It is noted that the submm peaks and high-brightness, diffuse emission that runs east-west along the major axis of the galactic disc may be associated with east-west dust lanes with a blue-brownish hue that are seen in the very central regions of M 82, shown in Figure 6.2. In that case, the hot, massive, young stars that are responsible for the blue hue could be heating the dust in these inner regions, leading to the submm high surface brightness emission. This type of heating will also result in bright short-wavelength infrared emission as well as emission lines associated with intense star-formation which has been extensively reported in M 82 (e.g. Alonso-Herrero et al., 2001). Further investigation of these central features will elucidate any differences between the heating of dust in the central and outer parts of M 82.

6.3.2 Submm vs. High-Resolution CO (1-0) Morphology

Figure 6.5 shows black contours of the integrated-intensity-CO (1-0) data, that were obtained with the Berkeley Illinois Maryland Association (BIMA) interferometer by Shen & Lo (1995), overlaid on the SCUBA 450 and 850 μm continuum images. The BIMA

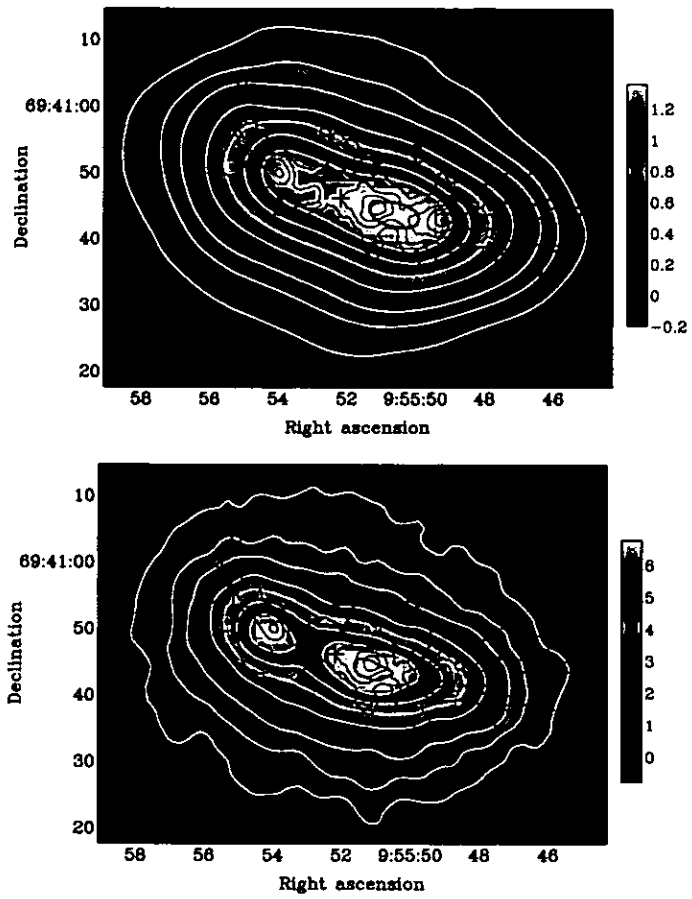

Figure 6.5: The central $76'' \times 56''$ region of M 82 at 850 (top panel) and 450 μm (bottom panel) overlaid with the integrated-intensity (black contours) of the CO (1-0) interferometry data by Shen & Lo (1995). The white 850 and 450 μm contours on the respective maps are [200 to 1175] and [900 to 6000] mJy/beam, as displayed in Figure 6.3. The red 850 and 450 μm contours are at 1350 and 6800 mJy/beam and are plotted to highlight the position of the respective western submm peak. The cross marks the 2.2 μm peak (Dietz et al., 1986). The keys and coordinates are as in Figure 6.3.

maps are at resolution $2''.4 \times 2''.6$ and are plotted to investigate the spatial correspondence between the submm continuum morphology and the high-resolution CO features. It was noted earlier that CO (1-0) (e.g. Nakai et al., 1987) and (2-1) (e.g. Thuma et al., 2000) observations, that are of comparable resolution to the SCUBA maps, showed that CO emission traced dust re-radiation rather well in the nuclear regions of M 82. Therefore, the BIMA maps are expected to give a reasonable indication of how dust emission may appear at higher resolution and perhaps also some insight about the structure seen in

the SCUBA images. The BIMA maps probably provide the best observational, high-resolution evidence of nuclear structure that is associated with dust, as submm continuum observations of dust in M 82 are not currently available at a resolution higher than 6″.7, that is obtainable with SCUBA at 350 μm (cf. Section 6.6.2 on resolution-enhancement of the SCUBA images).

The first obvious difference between the SCUBA and high-resolution-BIMA maps is that the emission peak that is indicated by red contours and appears about 8″ west of the nucleus in the submm maps is resolved into two peaks centred about 9″ apart in the CO maps. Of these two CO western peaks, the one closer to the nucleus is co-spatial with the 450 μm (red contour) and slightly east of the 850 μm (red contour) western peaks, and the one farthest from the nucleus is on the eastern edges of the submm 850 and 450 μm high-brightness lobes. Assuming that the CO and dust grains are mixed and that the relative brightness of peak and diffuse emission in CO is similar to that in submm continuum, then it is quite reasonable that the elongated submm western peak corresponds with the resolved CO western peaks. In fact, the roughly 9″ resolved separation of these western peaks as seen by the 2″.5-BIMA beam is consistent with the 10″ unresolved elongation (in the same direction as the separation of the CO peaks) as seen by the 6″.7-350 μm and 8″.5-350 μm beams. The good correspondence suggests the BIMA maps do indeed give a reasonable indication of how dust emission peaks may appear at higher resolution.

Contrary to indications above that the CO and submm emission peaks correspond very well at the scale of the BIMA and SCUBA beam-sizes, it appears from Figure 6.5 that the CO, however, does not trace direct emission of diffuse dust in a very simple way, particularly in the nuclear region west of the most western CO peak. Here, the CO

emission fans-out westerly at position angle 85°; i.e., it diverts from the 72°–position-angle of the submm continuum lobes and disc along the major axis, as well as that of the CO within a 10″ radius from the galactic nucleus. There is some hint from the south-western ridge of the high surface brightness continuum in the 850 μm and especially the 450 and 350 μm images that the dust emission also bends northward from the position angle of 72°. This is strengthened by the data from the submm spectral index maps (Figures 6.6 and 6.7) that are shown in Section 6.4, where the deviation is interpreted as a manifestation of a star-formation environment that is different to that near the galactic nucleus (also see Section 6.4 or Achtermann & Lacy, 1995). Higher resolution observations of dust that will soon be possible with the commissioning of the Smithsonian Submillimeter Array (Moran, 1996) and the *Space Infrared Telescope* (e.g. Deutsch & Bicay, 2000) will provide direct observational evidence to further test how well the CO and dust emission trace each other at the small scales shown in the BIMA maps. Those future observations will also test if dust emission has more complex morphology than has currently been detected, as is suggested by the increasing structure that is seen in the SCUBA maps going from low to high resolutions. Further discussion of the origin and structure of the submm emission peaks is detailed in Section 6.5.

6.4 The Nuclear Spectral Index Distribution

An analytical review of CO results is undertaken in Section 6.5.2 to assess if CO emission may contaminate the continuum of M 82 observed in SCUBA filters. For one, significantly different contributions in the 850 and 450 μm will affect the appearance of spectral index distribution in this galaxy and indeed its interpretation. If the differences are important, the spectral index distribution should in theory be calculated after correcting or

accounting for the CO contamination. It is currently not obvious if the contamination to the higher-frequency continuum will be less or higher than the *47%* estimated to the SCUBA-850 μm band by Seaquist & Clark (2001); even though it is clear that it may also be important (see Section 6.5.2). While relevant CO data need to be acquired in the future to make a quantitative calculation of the relative contributions in the SCUBA bands, for the practical determination of the spectral index of M 82 in this thesis, it is assumed that the CO contribution in 850 and 450 μm data is the same.

The spectral index distribution of M 82 has been computed from the deep 850 and 450μm imaging data that were obtained using a 120″ chop throw and shown in Figures 6.3. The spectral index map is used to investigate the dust properties in the galaxy and to probe the nature and extent of dust outflows entrained in the reported winds out of the galaxy. First, the 450μm map was convolved with a gaussian function in order to convert the 8″.5 resolution of this map to the 14″ resolution of the 850μm map. The spectral index α and the relative uncertainty $\Delta\alpha$ in its determination were computed using equations 5.1 and 5.2 respectively, as described in Section 5.4. Following equation 5.2, the estimated maximum error in the final spectral index map is $\mid \Delta\alpha \mid_{\rm max} \approx 1.2$ and the mean uncertainty is $\mid \Delta\alpha \mid_{\rm mean} \approx 0.3$.

Figure 6.6 shows the spectral index map of M 82 between 450 and 850μm overlaid with 850 μm intensity contours that range from 0.12 to 1.35 Jy/beam and are adopted from Figure 6.3. The distribution of the spectral index is asymmetric about the major axis and delineates two unique areas: 1) a flattened region of minor radii 10″, that is outlined by a dark-blue colour in the middle of Figure 6.6 and referred to as the *disc*, and 2) a region north and south of the disc, that is marked by green and yellow-red colours in the same figure and referred to as the *inner-halo*. The spectral index disc is slightly

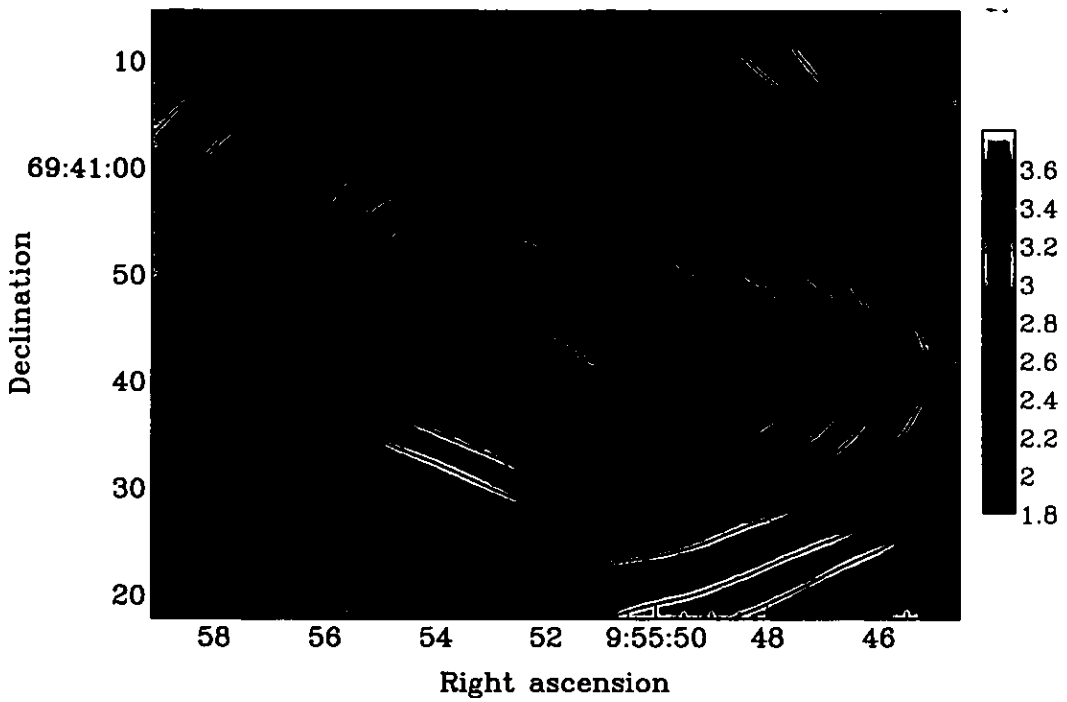

Figure 6.6: The spectral energy distribution map of M 82 between 450 and 850 μm is overlaid with 850 μm contours. The colour-coded key is the spectral indices, and the cross marks the 2.2 μm peak (Dietz et al., 1986). The contours are 850 μm intensities from 0.12 to 1.35 Jy/beam and separated as in Figure 6.3.

to the north of the dynamical nucleus and roughly co-spatial with the continuum disc.

The spectral indices range from about 2.3 to 2.6 in the star-forming disc to about 2.7 and 2.9, respectively, in the north and south inner-halo plateaus. These indices are consistent with thermal re-radiation of low-emissivity (i.e. $\beta \sim 1.3$; e.g. Hughes et al., 1994) dust that dominates the emission in M 82 at these submm wavelengths. In the south of the disc, the spectral index gradient is steeper and more uniform than in the north, as marked by the black contours that are stratified parallel to the major axis of the disc (see Figure 6.7). The spectral index distribution is rather knotty in most of the inner-halo, though with a general north-south asymmetry. The south is smoother and has on average higher indices. In general, the spectral index distribution increases from the nuclear region out along the minor axis of the disc, and is fairly flat along the major

axis.

It is worth mentioning some remarkable similarities between disc features in the spectral index distribution map and those seen in the morphology of M 82 obtained from other wavelengths. The spectral index disc has position angle $\sim 72°$, as seen at other wavelengths, but here its major axis goes slightly north rather than through the galactic dynamical nucleus. About 18″ west of the nucleus, the disc bends to position angle $\sim 85°$, very similar to the bend seen in the CO (1-0) emission here (see Figure 6.7). The CO (and also 850 and 450 μm) peak that is $\sim 6''$ west of the nucleus is at the position of separation between the regions of position angles 72° and 85°. The two regions are referred to as the *central* and *western* discs respectively and will be discussed further below. In maps of NeII by Achtermann & Lacy (1995), these regions show similar change in position angles after the western emission peak; those authors refer to the area of separation as the 'wedge'.

As mentioned in Section 6.3.2, the western disc is known to have relatively lower gas density and thus also lower star-formation efficiency than the central disc (Achtermann & Lacy, 1995). That the two regions have two different star-formation environments is supported by optical spectroscopic studies by Förster Schreiber (2000) and de Grijs (2001). In the submm spectral index map, the western disc is distinguished by a "hole" with $\alpha < 2.5$, perhaps indicating a change from a dominance of thermal to non-thermal emission, or a manifestation of the destruction of grains that see radiation directly from the central heating of the galaxy. As shown in Figure 6.7, the contours of the CO (1-0) fan-out westerly along the major axis of the disc in this region.

It is noted that the spectral index distribution map does not have similar western peaks to the 350, 450 or 850 μm continuum maps. The difference from the 850 μm is

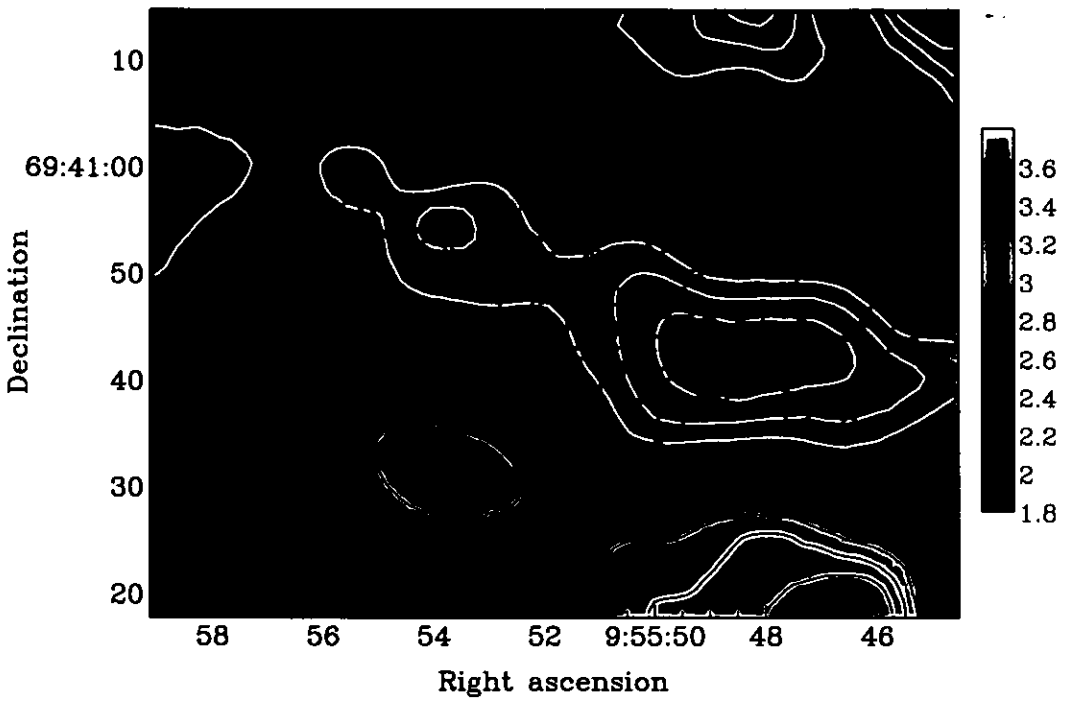

Figure 6.7: The submm spectral energy distribution map of M 82 is shown overlaid with red contours of the CO (1-0) interferometry data by Shen & Lo (1995). The colour-coded key is the spectral indices between 450 and 850μm and the black and white contours are spectral indices from 2.3 to 3.2 in steps of 0.1. The cross marks the 2.2μm peak (Dietz et al., 1986).

especially surprising because that map is of similar resolution. Also, the spectral index from the position of the nucleus to the position of the submm emission peaks (see, e.g., Figure 6.3) increases inversely to the flux density in the continuum maps, indicating that the ratio of 450 to 850 μm, or temperature (as expected), is higher at the 2.2μm nucleus in comparison to that at the peaks. As with the continuum distribution along the disc, the temperature increase about the nucleus is asymmetric, supporting suggestions in this thesis that the submm emission in the inner disc originates from re-radiation of dust concentrations rather than a dusty torus about the nucleus (see Section 6.5.1 below).

6.5 Origin of Submm Continuum Morphology and Spectral Index Distribution

6.5.1 Source and Structure of the Nuclear Submm Continuum

The radiation at the radio, mm and submm-to-infrared wavelengths in M 82 is respectively dominated by synchrotron emission from supernovae, free-free emission from ionised gas, and thermal re-radiation from dust heated by young stars. In this light, the double peaks seen in the mm to infrared continuum have commonly been interpreted as due to emission from the edges of an inclined, dusty-molecular torus, that – as a result of their geometry on the plane of the sky and optically-thin nature of radiation – have relatively high optical-depths in the line of sight (e.g. Hughes et al., 1994). In Figure 6.3, and other mm-to-infrared maps of similar or worse resolution (such as those from *IRAS*), the double peaks are not resolved and appear as a single, elongated lobe that is brightest in the southwest. Like the galactic disc, the lobe (or nuclear peaks when resolved-out) has a position angle of roughly 72° and – in the tori interpretation (e.g. Shen & Lo, 1995) – an inclination of $\sim 10°$.

The peaks of emission seen in the mm to infrared have alternatively been interpreted simply as dust and molecular concentrations along the galactic disc, perhaps in a bar structure (e.g. Neininger et al., 1998). This interpretation is supported by at least three reasons. First, the east-west, double peaks have now been seen in maps of both optically thin and thick CO emission (e.g. Petitpas & Wilson, 2000). This is reasonable if the emission is from a structure that constitutes concentrations or clouds of dust but is contrary to what is expected if the emission is from a structure with tori geometry that, like the galactic disc, is thought to be highly inclined (e.g. Shen & Lo, 1995). For optically

thin radiation, it will be possible to detect emission from the inner parts of the imaged structure, and either dust clouds or indeed edges of an inclined torus would manifest as regions of relatively higher optical-depth or brighter optically-thin emission in the line of sight (e.g. Hughes et al., 1994). However, as also noted by Neininger et al. (1998) and Petitpas & Wilson (2000), for optically thick radiation, it will be possible to directly detect emission only from the foreground surface of the imaged structure. In that case, the dust clouds will be seen as two emission peaks, while the torus (or bar) will manifest as an elongated, barlike emission of roughly the same optical depth or optically-thick brightness.

Second, the two main peaks seen in maps of similar resolution as the 450 and 350 μm images in Figures 6.3 and 6.4 are not symmetric. In maps of better resolution and sensitivity (e.g. Shen & Lo, 1995, see the CO contours in Figure 6.5), the peak west of the nucleus has a morphology clearly different from the eastern peak and can be resolved into two or three structures. High resolution VLA maps by Wills et al. (1999) show that the western peak is associated with locations of supernova explosions of higher intensity and earlier evolutionary stage than the eastern peak. This is supported by high resolution *HST* imaging of stellar clusters that indicates that the regions near the eastern and western submm peaks have different star-formation histories (e.g. de Grijs, 2001). In this light, the submm peaks indicate concentrations of dust environments associated with different locations of varying supernova and star-formation activity, not the commonly assumed dust torus.

Third, observations of line ratio gradients indicate that the average temperature across the lobe increases from the northeast to southwest, while the density increases in the opposite direction (e.g. Petitpas & Wilson, 2000). Further evidence of the higher

temperature or, at least, column density in the southwest is seen in the lopsided 850 and 750 μm lobe and the double-peak 450 and 350 μm lobes in which the southwest parts are the brighter. A torus that probably houses and is heated by an active galactic nucleus (e.g. Muxlow et al., 1994), would be expected to have temperature and density that increase from its inner to outer walls. One explanation for the higher temperature and lower density in the the southwest is linked with star-formation activity that both heats and depletes the interstellar medium (ISM) at this location (Wills et al., 1999), or simply western and eastern regions of two different star-formation physical environments (e.g. Achtermann & Lacy, 1995; Förster Schreiber, 2000; de Grijs, 2001). Evidence in this thesis in terms of clearly asymmetric submm emission seen in almost all the presented intensity and spectral index distribution maps seems to disfavour the commonly assumed interpretation of a dusty torus in M 82.

6.5.2 Possible CO Contamination of the Submm Continuum?

It is worth noting that the dust morphology that is mapped in the submm continuum from M 82 may be substantially enhanced by CO emission from this galaxy. A recent flux comparison between CO(3-2) emission and 850 μm continuum in M 82 showed that CO makes a 47% (i.e. high) contribution to the integrated continuum in this SCUBA band (Seaquist & Clark, 2001). From analysing collated CO(4-3) observations together with those of CO at lower transitions, Guesten et al. (1993) concluded that the line strengths in M 82 increased as one went to higher transitions, indicating that the higher transitions must provide significant cooling in the galaxy. All SCUBA bands have roughly the same widths, i.e. 30 GHz, and therefore the CO contribution to the higher frequency continuum would be expected to be equally or more significant than that reported for the 850 μm

band by Seaquist & Clark (2001). However, because the submm continuum in M 82 has a thermal spectrum (e.g. Hughes et al., 1994), and therefore the submm fluxes increase with frequency, the CO contribution to the higher frequency continuum may be less than the estimates for the 850 μm band.

Recent observations using a new high frequency, Fabry-Perot spectrometer on the JCMT have lead to clear detections of the high transition CO(7-6) in M 82 and NGC 253 (Bradford et al., 1999), the first such detection in any extragalactic sources. The analysis by Guesten et al. (1993) and the recent detections of CO(7-6), whose transition line lies in the 450 μm filter bandpass, suggest that other higher transition lines, such as the 13CO(8-7) line that lies at the centre of the SCUBA 350 μm band, could be very strong in M 82, supporting the proposition above that the high frequency SCUBA images may have significant contribution from CO. In this light, the morphology seen in the SCUBA images is a direct probe of the galactic cooling and the general interactions of active star formation and the ISM in M 82.

If molecular line contamination is indeed significant in M 82, it could explain some small differences seen in the 450 and 350 μm continuum, such as most obvious in the maps obtained with the 180″ chop throw shown in Figure 6.13. The 350 μm observations have only a slightly better resolution than the 450 μm and are separated only by 100 μm in wavelength space. Also, the fluxes from the two wavebands are both on the Rayleigh-Jeans slope and are expected to come from optically thin dust of roughly the same temperature. Therefore, the continuum morphology is expected to be the same. However, the contamination by lines of different transitions could be of varying degrees in the two continuum bands, particularly if the conclusion by Guesten et al. (1993), that the line strengths in M 82 increased as one went to higher transitions, is applicable in these bands.

It is noted that because the transitions lines are narrow compared to the continuum bandpass, their total flux would have to be extremely large, in order to have a continuum contribution of say higher than 47% (e.g. Seaquist & Clark, 2001), and would indeed prove that the lines provide significant cooling in the galaxy.

Although it is not obvious if the CO contribution to the higher frequencies of SCUBA will be less than or as significant as estimates by Seaquist & Clark (2001), it is clear that the CO contamination to higher-frequency continuum warrants investigation. Future work on this galaxy will attempt to acquire the data of the CO lines in the 450 and 350 μm bands and make a quantitative comparison of these data in order to determine the possible contributions of CO to the high-frequency-SCUBA data. Such work is important (among other things) in the determination and interpretation of submm spectral index distribution and thus the nature of dust emission in M 82 (see Section 6.4).

6.5.3 Implications of the SCUBA maps on the Outflow of Cold Dust

There is a general north-south asymmetry and filamentary structure in the spectral index distribution map of the nuclear region and the continuum morphology in the inner-halo of M 82, that is consistent with the north-south asymmetric X-ray and H_α winds (e.g. Watson et al., 1984) and the associated UV, optical, molecular and indeed infrared to mm structures that have been reported in M 82 (e.g. Seaquist & Clark, 2001). Therefore, a simple interpretation of the asymmetric, filamentary structures in the submm spectral index distribution in the nuclear region and the continuum morphology in the halo of M 82 and is that they are a manifestation of an outflow of dust from the nucleus to the halo.

Seaquist & Odegard (1991) presented one of the earlier, extensive evidence of the nuclear-to-halo outflows from spectral index distribution computations using radio continuum maps at several wavelengths between 0.33 and 4.9 GHz (90 and 6 cm). They found spectral indices between –0.3 and –0.6 in the nuclear region, steepening to about –1.0 at a radius of about 1 kpc along the minor axis, and concluded that these were from relativistic synchrotron-emitting electrons that were being scattered against infrared photons emitted in the nuclear regions of M 82. Recently, Wills et al. (1999) used high resolution VLA continuum data between 1.4 and 5 GHz and computed spectral indices from -0.6 to -0.8 about 20″ north of the galactic disc, in localised nuclear sites of the outflows that they call 'chimneys'. These values are consistent with the results by Seaquist & Odegard (1991) in the same wavebands, and Wills et al. (1999) also interpreted them as indicating synchrotron emission from relativistic electrons entrained in the wind.

A thermal component in the filaments has previously been suggested based on 'tentacles' observed in Ne II maps of M 82 (Achtermann & Lacy, 1995), which presumably are also a manifestation of the outflow phenomenon. In the maps in this thesis, the values of the spectral index distribution in the inner-halo range from about 2.6 to 3.1, consistent with thermal re-radiation of low-emissivity dust that dominates the emission in M 82 at these submm wavelengths (see, e.g., Hughes et al., 1994). The submm indices are asymmetric and increase predominately along the minor axis of the disc, similar to the radio spectral index gradient by Seaquist & Odegard (1991) and Wills et al. (1999) and consistent with the north-south asymmetric, large-scale X-ray and H_α winds (e.g. Shopbell & Bland-Hawthorn, 1998). In this light, the submm continuum maps indicate an outflow of dust grains that are ejected from the nuclear region by, or entrained in, the starburst winds.

One explanation for the outflow being asymmetric was given by Shopbell & Bland-Hawthorn (1998), who suggested that if the star-forming disc is slightly shifted up from the galactic disc, this would imply that there is less covering material in the north and would make collimation difficult, resulting in an immediate blow-out of material in the north. Detections confirming that collimation is better to the south of M 82 have been made of large-scale emission extending to 1.5 kpc, and more extended in the south, not only in optical line maps (e.g. Devine & Bally, 1999), but also in CO(2-1) and CO(3-2) respectively by Thuma et al. (2000) and Seaquist & Clark (2001). Another valuable result of the co-addition of SCUBA archive data in this thesis is that the most sensitive submm maps that are displayed in Figure 6.3 show submm extended emission that is associated with the outflows on scales that for the first time match the 1.5 kpc CO detections noted above.

Recently reported radio 'chimneys' (e.g. Wills et al., 1999), that are about 20″ north of the disc and hypothesised to signify local blow-outs of material by supernova-driven winds, are not obvious in the SCUBA maps. However, prominent SiO features associated with the localised radio outflows have now been detected in mm-heterodyne observations obtained with the IRAM interferometer (e.g. García-Burillo et al., 2001). Contours of these SiO features overlaid on the 5 GHz radio maps by Wills et al. (1999) are reproduced from the work by García-Burillo et al. (2001) and displayed in Figure 6.8. The authors explain the SiO detections in a framework of shocked chemistry at the sites of the gas ejections from the starburst disc. It appears that the shocked gas has for the moment proved to be a better probe of the localised outlows than the direct observations of dust emission in the mm to submm continuum.

Localised sites of the outlows or 'emission spurs', although long sought-after and

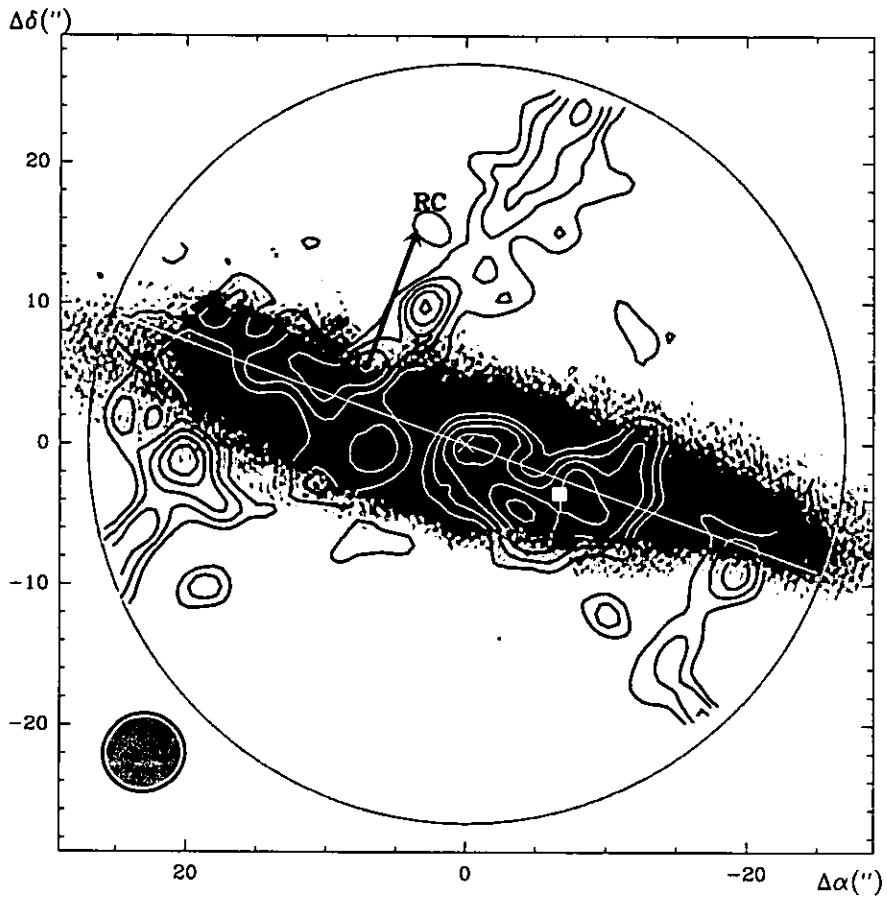

Figure 6.8: The velocity-integrated intensity map of SiO (v=0,J=2-1) in the central region of M 82, that was produced by García-Burillo et al. (2001), is overlaid on the saturated gray-scale of the 5 GHz continuum image from work by Wills et al. (1999).

sometimes reported in mm to submm continuum and CO maps (e.g. Hughes et al., 1994; Shen & Lo, 1995; Leeuw et al., 1998; Alton et al., 1999), have not been reliably reproduced in the different mm to submm observations. All the continuum maps in this thesis also have some low-level 'spurs', but almost none are reproduced at exactly the same locations and extend to the same degrees between any two different observations. This would suggest that the spurs might be artefacts in the maps. However, it is mentioned in passing that the spurs at the edges of the submm maps may be associated with complex optical filaments that are seen criss-crossing M 82 in optical pictures (see, e.g., Figure 6.2). If the filaments have different optical depths and re-radiate low-level emission in relatively

narrow wavebands, they may not be reproduced in maps at certain wavelengths and sensitivities. Preliminary results from high-resolution, interferometry observations of '...molecular streamers around M 82' by Walter et al. (2001) seem to strongly support the association of mm-continuum spurs with optical filaments. Therefore, the above hypotheses will almost certainly be tested in the near future as sensitive submm and optical observations become available and allow precise spatial associations between the emission spurs and the absorption filaments to become possible.

6.6 Exploratory Analysis of MEM and the 180″ Chop Throw

6.6.1 Can MEM reprocessing Improve SCUBA Images?

This section presents original and Maximum Entropy Method (MEM)-reprocessed, SCUBA-450 μm maps of CRL 618 and Centaurus A, in an effort to investigate the usefulness of employing the MEM technique to improve the resolution of SCUBA images as used in the more complex submm maps of M 82 and described in Section 6.6.2. CRL 618 is a submm-bright, proto-planetary nebula that is a point source in the SCUBA beam and is used as a secondary calibrator at the JCMT (e.g. Sandell, 1994). Centaurus A is a merger-remnant galaxy that, as must now be familiar from this thesis (see Chapter 5), has a very bright, compact core and extended submm emission that have been observed with SCUBA (Leeuw et al., 2002).

The MEM routines used in this thesis are provided by the Starlink Project to perform a deconvolution of 2-dimensional images. The program uses algorithms based on Bayesian analysis of image reconstruction as presented in the Gull and Skilling Maximum-Entropy-

System-5 Manual.[1] This follows various improvements on the 'classical' MEM that was presented by Gull & Skilling (1983). The Starlink routines take an image and a point-spread function as input and, based on the noise and signal in the image, iteratively produce an equal-sized image as output with higher resolution. For this thesis, the SCUBA maps are reprocessed with beam-widths estimated from the relevant, nightly beam maps and the common assumption that the beam shapes are Gaussian (e.g. Sandell, 1998).

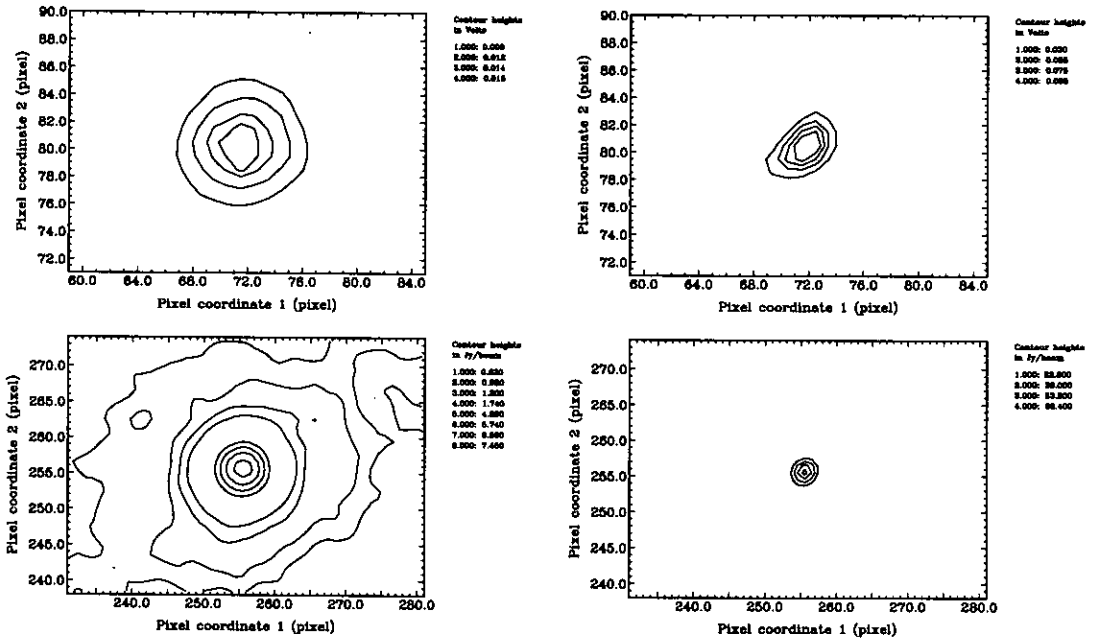

Figure 6.9: Original SCUBA-450 μm maps of CRL 618 and Centaurus A to the left and MEM-reprocessed images of these sources to the right. The CRL 618 and Centaurus A images are at top and bottom respectively. The keys are relative intensities shown by the contours. The axis are in pixel, representing arcsecond, displacements. Note that the bottom row images are at half the scale of the top images, in order to include the depiction of the extended emission in Centaurus A.

Figure 6.9 presents the original SCUBA-450 μm maps of CRL 618 and Centaurus A flushed to the left and the MEM-reprocessed images of these sources flushed to the right. The resolutions achieved in the SCUBA and MEM-reprocessed images of CRL 618, that

[1]The MemSys5 Manual describes the latest Fortran code implementation of the Gull and Skilling Maximum-Entropy Method, as is used in the Starlink software, and is available at http://www.maxent.co.uk

are shown in the top row of Figure 6.9, are 7″.8 and 2″.4 respectively, and those of Centaurus A, that are shown in the bottom row at half the scale of the top images, are 8″.2 and 2″.6 respectively. Therefore, for the 450 μm maps shown in Figure 6.9, MEM improves the SCUBA resolution by a factor of ~ 3. The images of Centaurus A in the bottom panels of Figure 6.9 show that in images with strong peaks that are surrounded by relatively low-level extended emission, the MEM devolution smoothes-out the diffuse emission and emphasises the isolated peaks at an improved resolution. Therefore, in the case where the peak is of much higher level relative to the diffuse emission, the technique is not ideal for seeing structure in the extended emission.

While the MEM-reprocessed image of Centaurus A that is shown in Figure 6.9 is fairly round, i.e. its major to minor axis ratio is ~ 1.1 and very normal for the not-perfectly–Gaussian SCUBA beams, the reprocessed image of CRL 618 is clearly elongated, i.e. its major to minor axis ratio is $\sim$ 1.5. High-resolution, mm-to-radio–interferometry observations of the CS (2-1) and CO (1-0) gases and 23 GHz radio continuum in CRL 618 respectively by Hajian et al. (1995, 1996) and Martin-Pintado et al. (1995) have reported detections of a multicomponent, extended structure that is dominated by a spherical halo of CO gas with radius $\sim 15''$ and a core east-west, bi-polar outflow of roughly $3'' \times 5''$ that is seen in all these observations and is roughly cross-shaped in CS gas. The elongation in the MEM image of CRL 618 is therefore probably the real, extended structure from the diffuse emission of this nebula. It is generally east-west, like the bi-polar outflow in the mm-to-radio–interferometry observations, and has the same orientation as one of the components in the CS gas maps. Therefore, although it is unresolved in the SCUBA beams (Sandell, 1998), it is revealed here by MEM for the first time in the submm. Extended, low-level submm emission is quite common in nebulae, which makes many of

them unsuitable secondary calibrators, even though their cores can be bright enough to make calibrators, in the submm regime (Sandell, 1998). The resolved submm emission in the MEM-reprocessed image of CRL 618 suggests that in the case that the extended emission is not too low-level compared to the peak emission, MEM deconvolution may be useful for seeing structure that is unresolved by SCUBA. While the images show that the MEM technique produces reasonable morphological results of reprocessed SCUBA maps, statistical tests and modelling of the MEM images, or comparisons with higher resolution images at the same wavelengths, are needed to confirm the quantitative usefulness of the employed routines.

6.6.2 Are MEM-reprocessed–SCUBA Peaks of M 82 Reliable?

This section presents Maximum Entropy Method (MEM) deconvolution of SCUBA-850, -450 and -350 μm images of M 82 to investigate if MEM reprocessing can reliably produce resolution-enhanced submm features of this galaxy. As is the case for CRL 618, the extended submm emission in the nuclear region of M 82 is not too low-level compared to the emission of the peaks in the same region, and in principle MEM deconvolution can produce useful results for M 82. If similar 'reliable' enhancement of resolution can be produced for the complex nuclear structure such as is expected in the active starburst of M 82, then the MEM submm images can be used for a comparative analysis with high resolution data from other wavelengths.

The SCUBA maps of M 82 that are used in the MEM deconvolution are the deep 850, 450 and 350 μm images that were obtained with the 120″ chop throw and presented in Figures 6.3 & 6.4. Their excellent signal-to-noise ratio makes them a good choice for use with MEM. For the input parameters of the MEM deconvolution, it is assumed

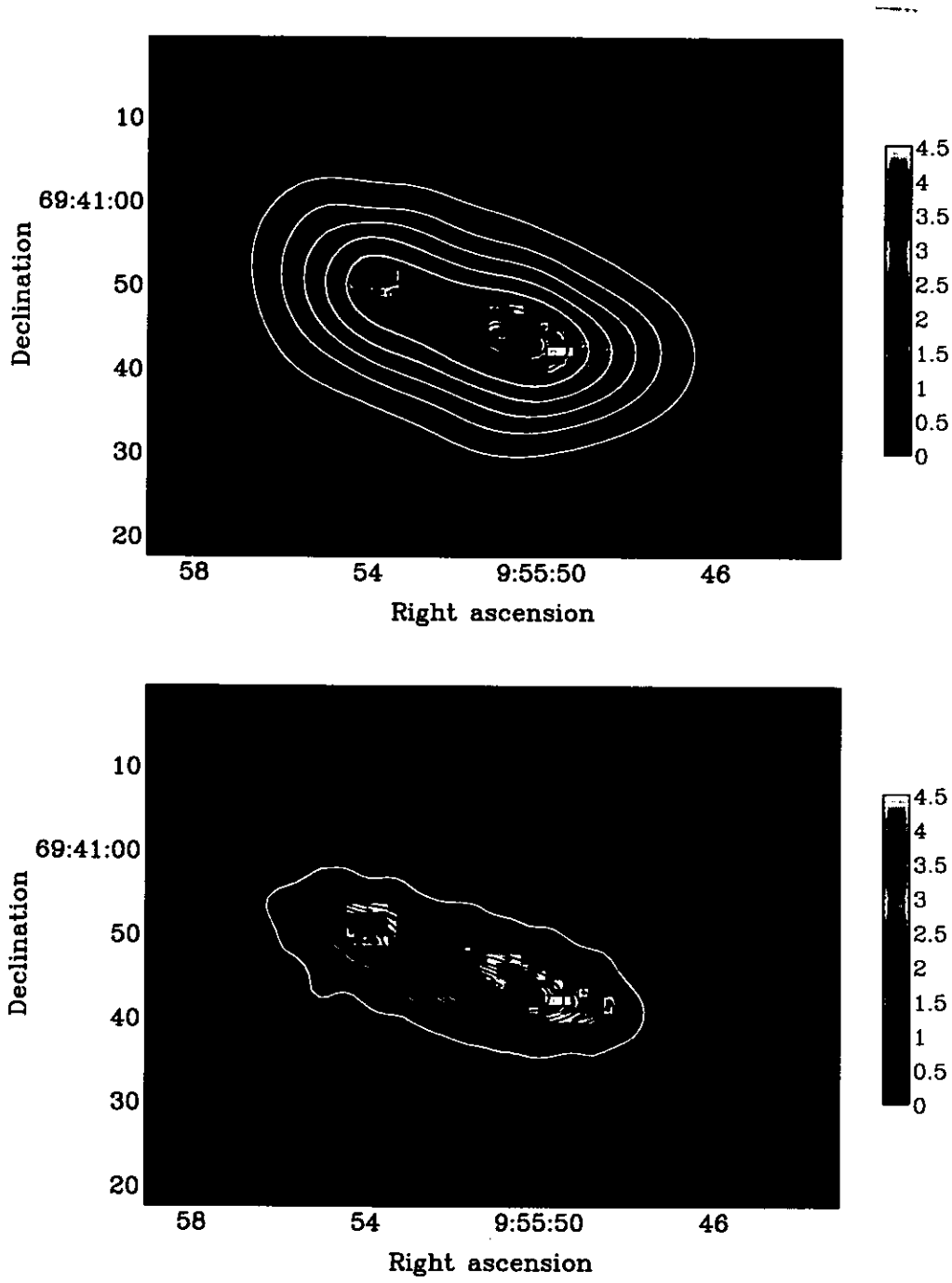

Figure 6.10: The MEM-reprocessed, deep-SCUBA-850 μm maps that were obtained with the 120″ chop throw are displayed in colour-scale. The MEM images have an enhanced resolution that show the best derived locations of the emission peaks given the signal-to-noise in the central parts of M 82. Original SCUBA contours at 850 (top panel) and 450 μm (bottom panel) are overlaid to cross-check the source of the MEM-resolution-enhanced features. The keys are colour-coded relative intensities, and the axis labels are J2000 coordinates.

that the SCUBA beams have Gaussian widths of 15″, 8″ and 6″.7 respectively at 850, 450 and 350 μm, as estimated from SCUBA point sources. The very diffuse emission in MEM images is smoothed-out and the high-level emission is emphasised to show the most probable details of the detection peaks in the central region of the M 82 disc at a resolution that has been improved by a factor of ~ 3.

The MEM-850 μm map of M 82 is presented in Figure 6.10 and compared with the original 850 and 450 μm contours that are overlaid to cross-check the source of all the MEM-produced features. The original 450 μm image has a higher resolution than the 850 μm map and therefore provides an observed example of the general morphology that is expected in the MEM-resolution-enhanced-850 μm map. Figure 6.10 shows that the morphology in the MEM-850 μm image is generally consistent with the submm emission peaks that are distributed along the spine of the galactic disc at a roughly 72° position angle, as shown by the original SCUBA contours. The single lobe of the original SCUBA-850 μm emission is now resolved into two peaks, as seen in the 450 and 350 μm maps. Also, the MEM process has reproduced the 850 μm western peak with a more elongated and brighter structure than that of the eastern peak, just as has been observed in SCUBA maps of higher resolution. However, the top panel in Figure 6.10 shows that the precise locations of the MEM-850 μm peaks are not well matched with those in the original maps. This is particularly true for the western peak that is reproduced at least 5″ farther west than the original 850 and 450 μm western peaks. A cross-check of the MEM-850 μm peaks with the original SCUBA images, as shown in Figure 6.10, shows that MEM peaks are systematically produced at the edges of all elongated, high-brightness emission in the original image, generally resulting in the locations of the peaks being moved farther away from their original positions.

That MEM deconvolves single peaks into two that are slightly shifted from the 'original' position, is not unreasonable, if the shift is not large in relation to the beamsize, for the following reason. If a very large smooth is applied to two resolved peaks – assume they are delta functions to drive the point home – then the smooth will result in a single peak that is located between the two resolved peak positions. It follows that as the peaks are smoothed more and more, the smoothed wings of the original peaks will contribute more and more in the area between versus outside the peaks, resulting in a systematic central shift. This will hold-up for equal and non-equal sources (that do not have to be delta). Therefore, observations of two (or more) peaks with a beam larger than their separation would result in an unresolved peak of the original two at a more central location than their true locations. By the corollary, it is therefore acceptable that MEM resolves and systematically shifts the single, unresolved peaks in two that are farther out.

Thus, it is also not surprising that the eastern peak seen in the MEM-850 μm and original 450 μm images in Figure 6.10 corresponds reasonably well, give-or-take an acceptable north-south pointing shift of $\sim 2''$, even though this peak is at the eastern-edge of the unresolved lobe in the original 850 μm image. However, the fact that the location of the western peak cannot be reproduced as well as that of the eastern suggests that not all the peaks that are produced by MEM reprocessing of M82 data are a reliable resolution-enhancement of the SCUBA images.

The above assertion is supported by a cross-check of MEM-reproduced–450 μm images with their original SCUBA contours, that are shown overlaid in Figure 6.11. The MEM colour-coded peaks are labelled 1 to 5, and the position of the 2.2μm peak or dynamic nucleus is marked by a black cross. The original double peaks (cf. MEM 1,2 and 3,4) seen on either side of the 2.2μm peak location in the SCUBA-450 and -350 μm

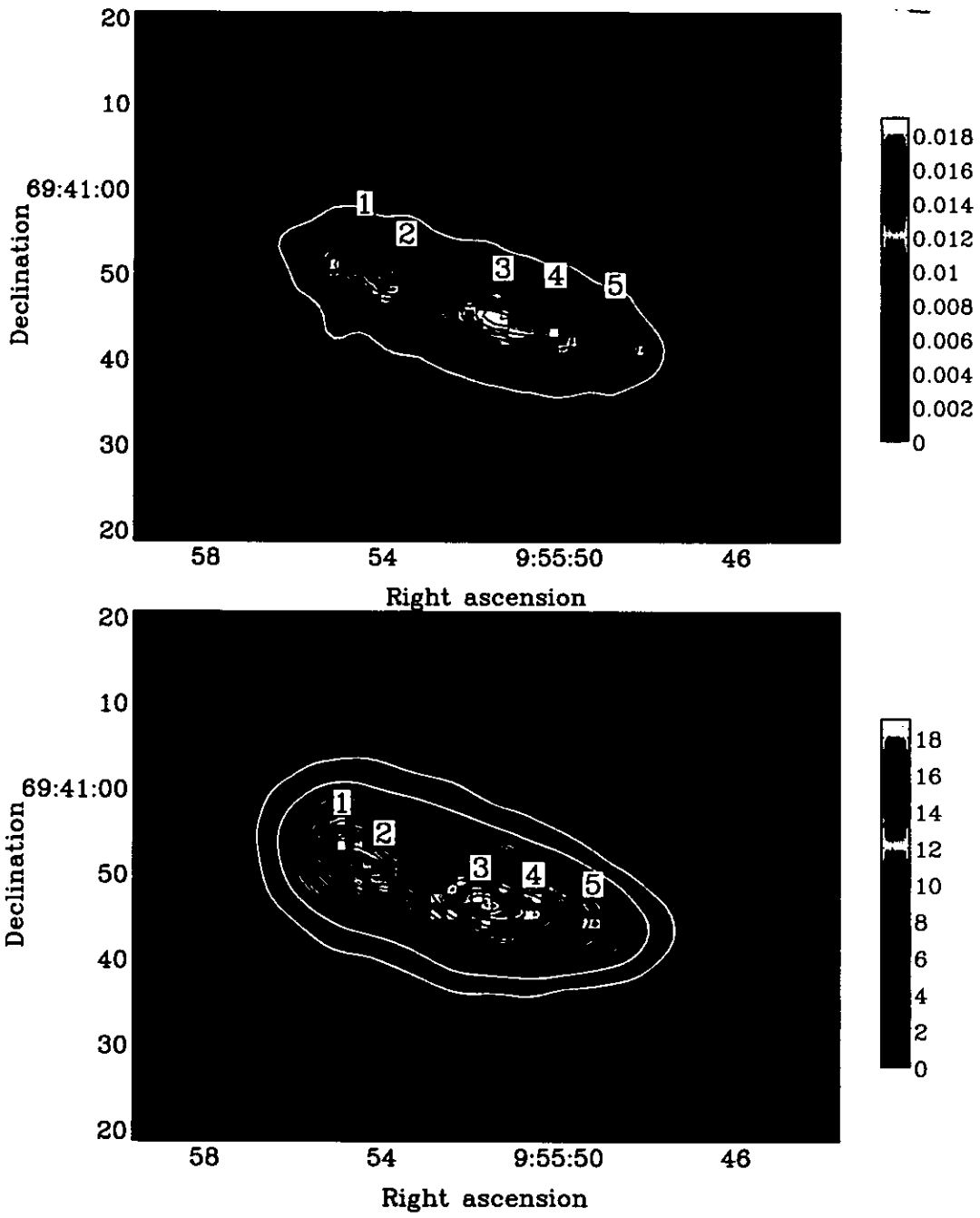

Figure 6.11: MEM-reprocessed, SCUBA-450 (top panel) and -350 μm (bottom panel) maps of M 82 that were obtained with the 120″ chop throw are displayed in colour-scale. The MEM images have an enhanced resolution that show the best derived locations of the emission peaks given the signal-to-noise ratio in the central parts of M 82. Original SCUBA contours are overlaid to cross-check the source of the resolution-enhanced features that are produced by the MEM procedure. The MEM peaks are labelled 1 to 5, and the position of the dynamic or 2.2 μm nucleus is marked by a black cross. The keys are colour-coded relative intensities, and the axis labels are J2000 coordinates.

contours are reproduced at roughly their original positions along the major axis of the nuclear disc. The elongated, brighter peak seen about 9″ west of the nucleus in the original images is now resolved into two peaks (i.e. MEM 3 & 4): one within $\sim 1''$ of the 2.2μm peak and the other (i.e. MEM 4) about 9″ west of nucleus. There is an additional peak (i.e. MEM 5) about 15″ west of the nucleus and the eastern peak is reproduced with an elongation of what seems to be two unresolved peaks (i.e. MEM 1 & 2) along the disc. As is evident in Figure 6.10, it is shown once again in Figure 6.11 that MEM systematically resolves all peaks with any elongated extension – however-slight – into two peaks (e.g. MEM 1 & 2) at the longward-edges of the structure. This often results in the locations of the peaks being moved farther away from their original positions, which, as explained earlier, can be reasonable if the shifts are not large in comparison to the beamsize.

A factor that may be affecting the precise reprocessing of peak locations may be that the assumption that the SCUBA beam is Gaussian (that is used in the MEM routines here) is not good enough for the deconvolution of the current M 82 images. As noted in Section 6.6.1 and shown in Figure 6.9 above, the SCUBA beam is not a perfect Gaussian. Other authors using separate MEM software as that used in this thesis have achieved what appears to be reasonable results in their reprocessing of M 82 data at other wavelengths (e.g. Dietz et al., 1989, in their 10 μm images). However, some of their MEM reprocessing, for example on the Ne II data by Achtermann & Lacy (1995), results merely in a smoother image of the original, rather than an improvement of resolution as undertaken in this thesis. This is consistent with the demonstrated evidence in this thesis that MEM reprocessing is reasonably true to the input data.

With the precise locations of the resolved peaks aside, MEM's systematic re-production

of unresolved peaks into two (or more) peaks shows that the deconvolution is biased to producing point sources, that are not a unique reproduction of the original structure. In other words, the MEM results of M 82 show that, given reasonable signal-to-noise ratio in the images, all mapped structures that are extended will be deconvolved into point sources, even if the structure is *truly* extended at the higher resolution seen in the MEM images. This makes the reprocessed results true to MEM and the data, but not to the reproduction of real (extended) structure.

The conclusion in this thesis is that, based on morphological comparisons of the original and MEM-deconvolved images, MEM reprocessing can be true to the data in the image but is not useful for uniquely enhancing the resolution of the SCUBA maps of the complex nuclear region in M 82. The MEM-reprocessed maps displayed in Figures 6.10 and 6.11 are therefore presented only to demonstrate the results of the MEM deconvolution of M 82 maps that were obtained with SCUBA and are not used in any further scientific analysis in this thesis. Further assessment of the use and implementation of MEM for the SCUBA data of M 82 may be considered in the future.

6.6.3 Does a 180″ Chop Throw Improve the Submm Image of M 82?

Figures 6.12 and 6.13 show maps of M 82 at 850, 750, 450 and 350 μm that, like the maps shown in Figures 6.3 and 6.4, were also obtained in jiggle mapping observing mode, but with an azimuthal chop throw of 180″ rather than 120″. The 180″ chop is not commonly used with SCUBA and was employed in *exploratory* observations designed to chop clear of low-level emission of previously unknown submm extent. These maps are not as deep or well calibrated as the images with the 120″ chop, that are displayed in Figures 6.3 and 6.4, and are *preliminarily* presented, only to cross-check features in submm maps and to

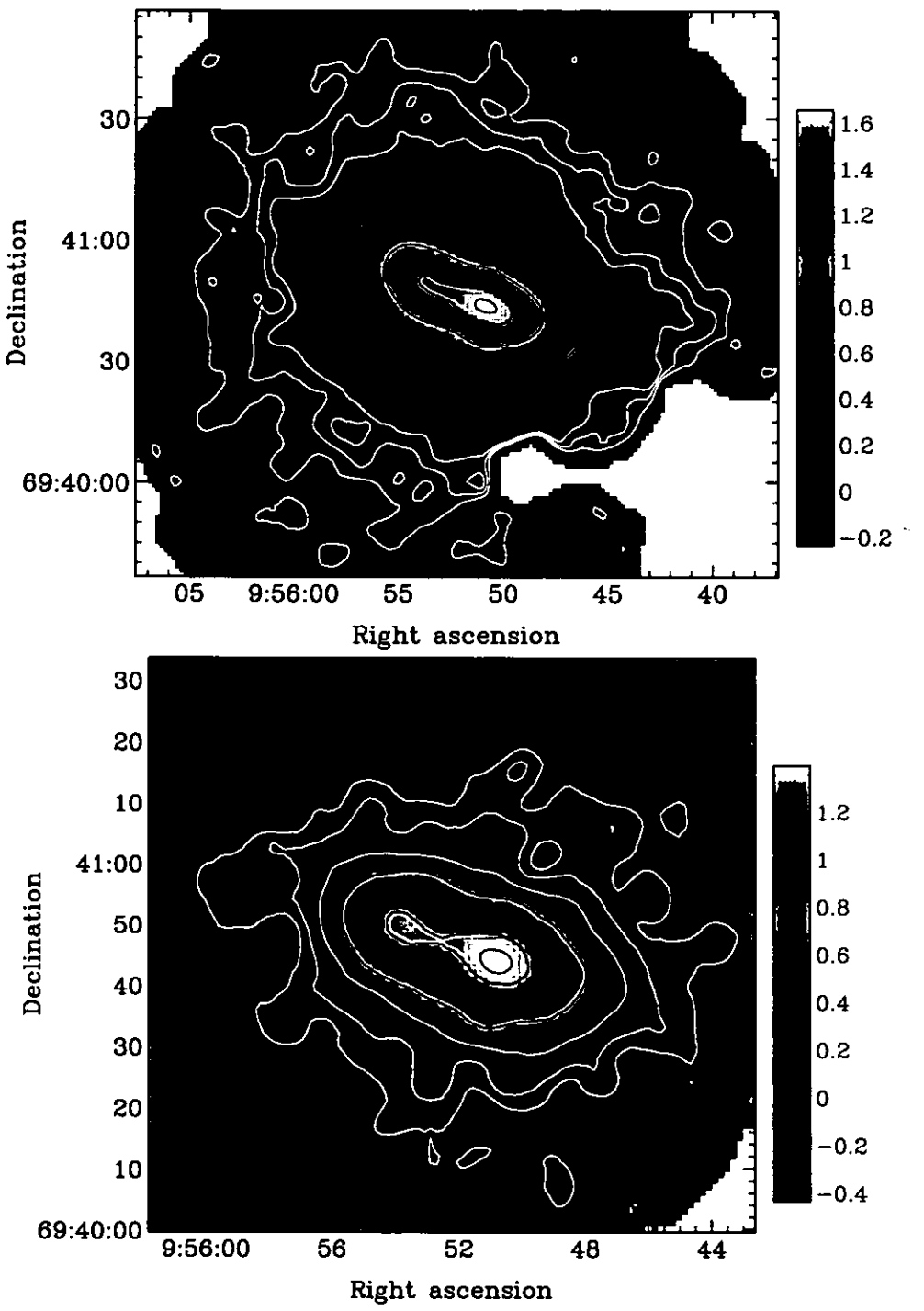

Figure 6.12: Maps of the 180″ chop throw, 850 (top panel) and 750 μm (bottom panel) continuum emission centred at the near-infrared nucleus of M 82. The contours on the respective maps are [64, 96, 128, 200, 300, 400, 600, 800, 1000, 1175, 1350, 1525, 1670] and [200, 275, 425, 700, 1000, 1300, 1450] mJy/beam; the rms uncertainty is about 32 and 100 mJy/beam. The key is colour-coded intensity in Jy/beam, and the X and Y axes are J2000 coordinates.

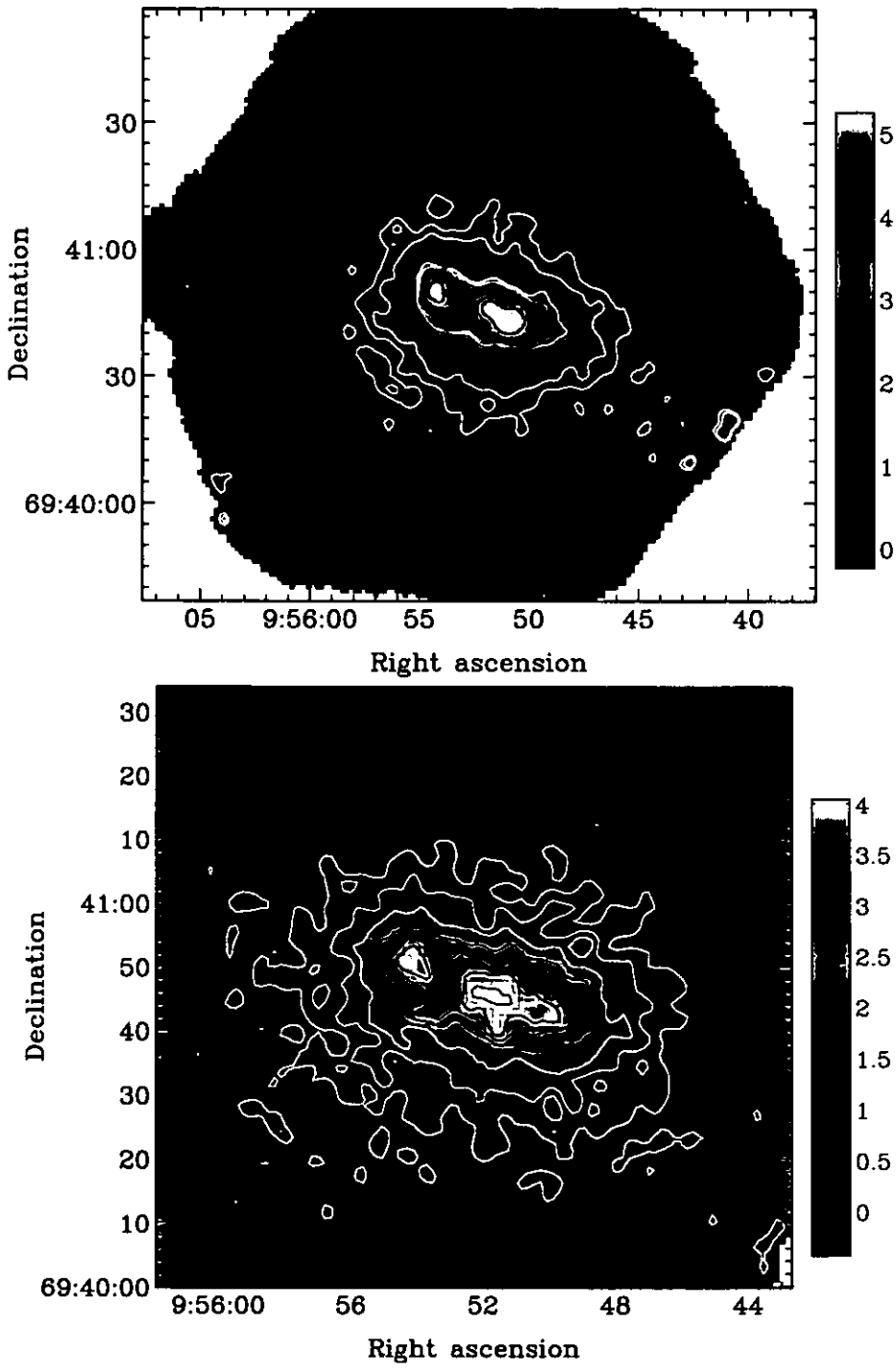

Figure 6.13: Maps with the 180″ chop throw, 450 (top panel) and 350 μm (bottom panel) continuum emission centred at the near-infrared nucleus of M 82. The contours on the respective maps are [950,1450, 2.100, 3.100, 3.800, 4.500, 5000] and [1250, 1750, 2250, 2900, 3400, 3800, 4100] mJy/beam; the rms uncertainty is at least 475 and 625 mJy/beam. The key is colour-coded intensity in Jy/beam, and the X and Y axes are J2000 coordinates.

determine if the 180″ chop throw improves the imaging of extended emission in M82.

The general morphology in these maps is indeed similar to the earlier 120″ chop throw maps (see Section 6.3), however the nuclear-disc peaks in the 450 and 350 μm maps in Figure 6.13 are less smooth, round or elliptical than those in the maps in Figures 6.3 and 6.4. The peak that is east of the nucleus is now more triangular and that in the west is not just elongated along the disc but now has remarkably more 'structure', especially in the 350 μm map. In the 450 μm map, this western peak is now pear-shaped, bulging with increasing major axis distance from the nucleus, and in the 350 μm map, it is resolved into two peaks that lie along the major axis of the disc. Of these resolved, western peaks in the 350 μm map, the peak closest to the nucleus is elongated along the disc-major axis, following the orientation of the original, but now the elongated emission is brightest at the position of the galactic nucleus and also has a spur in the south.

These new nuclear features in the 450 and 350 μm data of the 180″ chop throw have not been seen before in the submm continuum and that would be exciting if they were detected with strong confidence. Unfortunately, the reality of the features is questionable for at least the following simple reason. The features are not seen in the maps shown in Figures 6.3 and 6.4, and that is surprising because those maps are deeper and should therefore reveal all the *real* features displayed in Figures 6.12 and 6.13.

One explanation for the discrepancy comes from comparing the relative peak-to-baseline–flux ratios obtained from similar regions of the respective-wavelength 120″ and 180″ chop maps. The ratio in the 180″, compared to that in the 120″, chop maps, is lower and decreases with decreasing submm wavelength maps (i.e. the ratio decreases systematically from the 850 μm down to 350 μm maps). The reason is because, in comparable regions of the 120″ and 180″ chop maps, the baseline fluxes are similar, however

the peak fluxes in the 180″ chop maps are systematically lower. This indicates that peak fluxes in the 180″ chop maps are not conserved and the beams in these images are most probably distorted. It may be that the larger-180″ throw, that chops in azimuth while the image rotates during an observation, smears-out the peaks, trimming their fluxes and superficially enhancing their morphology.

Because the effect of altering the peak fluxes and morphology will increase respectively with decreasing beam-width and increasing resolution, and therefore with decreasing submm wavelengths, it will be strongest in the 350 μm images. In fact, engineering observations at the JCMT show that beam distortions in SCUBA maps will be worst at the shortest wavebands (e.g. Sandell, 1998). It is clear from the maps in Figure 6.13, that compared to those in Figures 6.4 and 6.4, the 350 μm images are indeed the most different between the 120″ and 180″ chop throw results. In the 450 and 350 μm images themselves, the peak west of the nucleus is more morphologically changed than the eastern peak, because the western one is elongated (cf. almost point-like eastern peak) and thus has more surface flux and structure that can be smeared-out by the 180″ throw.

On the basis that peak fluxes are not conserved in the current images with the 180″ chop throw, and that the 'new' features of M 82 in these maps are most probably artefacts created by distorted beams, the conclusion is that the 180″ chop throw maps shown in this thesis, particular at 350 and 450 μm are not an improvement on the other SCUBA images. Clearly, the current 180″ chop throw results raise interesting issues about peak flux and morphology conservation (or enhancement) with larger chops, particularly in short-wavelength SCUBA observations. This could be investigated further in beam-map observations of JCMT primary sources at large chop throws.

Finally, it is noted that in the 750μm image from the 180″ chop throw data set shown

in Figure 6.13, the single emission peak seen in the 850μm image (see Figure 6.12) is beginning to be resolved-out into the double peaks seen in the 450 and 350μm images (see Figures 6.12 and 6.13). This is expected, as the 750μm observations have a resolution that is intermediate between that of the 850 and 450μm.

6.7 Summary of Results and Future Work on M 82

SCUBA 350, 450, 750 and 850 μm imaging observations have been presented of the dust-laden, star-forming nuclear region and large-scale, low-level emission that is associated with the outflows in the halo of M 82. The displayed maps include co-added data that were mined from the SCUBA Data Archive, resulting in the deepest submm continuum maps of M 82. The 850 μm morphology has a single emission peak that is centred about 9″ west of the galactic nucleus, while the 450 and 350 μm maps have two emission peaks centred about 10″ and 6″ respectively east and west of the nucleus along the galactic disc, similar to previous continuum observations at mm, submm and mid-infrared wavelengths, as well as to CO line transitions and H_α observations of comparable resolution (see Section 6.3). Low-level emission is detected out to 1.5 kpc for the first time in the 850 μm continuum of this galaxy, i.e. at least $\sim$ 160 pc radius farther-out than other recent studies.

The deep maps were used in a detailed morphological study of the nuclear and large-scale detections, including a comparative analysis of submm to optical morphology (see Section 6.3.1). The overall, extended submm morphology of M 82 generally resembles the optical picture in that the nuclear emission has an apparently elliptical shape whose major axis is clearly aligned with that of the galactic disc at position angle $\sim$ 72°. However, the submm morphology is much smoother than the optical picture, and some prominent dust cloud and filamentary lanes that are seen in the optical are not obvious

in the submm continuum. One explanation for the submm versus optical correspondence (or lack of it) is that the optically-thin submm continuum represents total emission from the entire galactic columns of dust in the line of sight, while the optical morphology of dust, because the dust is typically seen *obscuring* stellar light, represents only the dust in certain spatial stratifications (usually the foreground) of the observed line-of-sight columns. A more quantitative spatial-correspondence and optical-depth analysis (and radiative modelling) of the submm versus optical images is clearly needed to make definite assertions about the origin of any of the features seen in the compared maps.

A comparative analysis was further conducted of submm to high-resolution CO (1-0) morphology (see Section 6.3.2). Resolved peaks in the CO maps could be associated with unresolved features in the submm maps. Assuming that the CO and dust grains were well-mixed, it was concluded that BIMA maps gave a reasonable indication of how dust emission might appear at higher resolution. This will be tested by future higher resolution observations of dust that will soon be possible with the commissioning of the Smithsonian Submillimeter Array (Moran, 1996) and the Space Infrared Telescope (e.g. Deutsch & Bicay, 2000)

The SCUBA maps were also used in the computation and investigation of the first submm spectral index distribution of the high-brightness, nuclear region of M 82 (see Section 6.4) and in the discussion of the origin and structure of submm maps (see Section 6.5). In particular, (a) the commonly assumed interpretation that the double emission peaks that were seen in the mm to infrared continuum are due to emission from the edges of an inclined, dusty-molecular torus was challenged (see Section 6.5.1), (b) an analytical review of CO results was undertaken to assess if CO emission might significantly contaminate the continuum observed in SCUBA filters (see Section 6.5.2), and (c) a mor-

phological comparison was conducted to check whether the localised outflows that were reported in radio and SiO maps respectively by Wills et al. (1999) and García-Burillo et al. (2001) could be seen in the SCUBA maps (see Section 6.5.3).

Evidence in this thesis in terms of clearly asymmetric nuclear-submm emission seen in almost all the presented intensity and spectral index distribution maps seems to disfavour the commonly assumed interpretation of a dusty torus in M 82. Arguments were presented to explanation the nuclear submm maps of M 82 in the context of emission from a rather complex distribution of dust concentrations that are in regions of different star-formation environments, as has been reported from various studies using data at other wavelengths (e.g. Achtermann & Lacy, 1995; Förster Schreiber, 2000; de Grijs, 2001).

It is not obvious if the CO contribution to the higher frequencies of SCUBA will be less than or higher than the 47% estimated to the SCUBA-850 μm band by Seaquist & Clark (2001). However, it is clear that the CO contamination to higher-frequency continuum may also be significant and warrants detailed investigation. Future work on this galaxy will attempt to acquire the data of the CO lines in the 450 and 350 μm bands and make a quantitative comparison of these data in order to determine the possible contributions of CO to the high-frequency-SCUBA data.

The overall submm low-level morphology has a general north-south asymmetry that is similar to the filamentary H_α winds and CO and X-ray outflows that have been detected in M 82 (e.g. Shopbell & Bland-Hawthorn, 1998). The submm spectral index distribution is also asymmetric with indices that increase predominately along the minor axis of the disc, similar to the radio spectral index gradient by Seaquist & Odegard (1991) and Wills et al. (1999) and consistent with the north-south asymmetric, large-scale X-ray and H_α

winds. Therefore, the current results support the simple interpretation (e.g. Leeuw et al., 1998; Alton et al., 1999) that the asymmetric, filamentary structures in the submm maps are a manifestation of corresponding outflows of dust grains from the galactic nucleus into the halo.

Preliminary analyses were conducted to investigate whether Maximum Entropy Method deconvolution can improve the SCUBA resolution of standard JCMT sources (see Section 6.6.1) and the deep submm maps of M 82 (see Section 6.6.2). It was demonstrated that MEM can produce reasonable, resolution-enhanced results for the SCUBA-450 μm maps of CRL 618 and Centaurus A. However, based on morphological comparisons of the original and MEM images, the conclusion in this thesis is that although MEM reprocessing can produce reasonable results, given the data in the submm images, it is not useful for uniquely enhancing the resolution of the SCUBA maps of M 82, particularly that of the complex nuclear structure in this galaxy. Therefore, MEM maps of M 82 were not used in any further scientific analysis in this thesis. Nevertheless, extended assessment of the use and implementation of MEM for the SCUBA data may be considered in the future.

Preliminary analyses were also conducted to investigate if observations with the 180″ chop throw could improve the detection of the submm continuum in M 82 (see Section 6.6.3), as the large throw was designed to chop clear of any unknown low-level emission. It appears that the larger chop throw smears-out peaks in the 350 and 450 μm continuum, trimming the high-level fluxes and creating artefacts in the morphology. On the basis that peak fluxes are not conserved in the current images with the 180″ chop throw, and that 'new' features of M 82 in these maps are most probably artefacts created by distorted beams, the conclusion in this thesis is that the 180″ chop throw maps, par-

ticularly at 350 and 450 μm are not an improvement on the other SCUBA images. The 180″ chop throw results clearly raise interesting issues about peak flux and morphology conservation with larger chops, particularly in short-wavelength SCUBA observations, and need to be investigated further in beam-map observations of JCMT primary sources.

It is re-emphasised that the results in this chapter are presented as work in progress, and therefore some the conclusions are rather *preliminary*.

Chapter 7

Summary of Thesis Results and Future Work

Millimetre and submm continuum observations of selected, nearby active galaxies have been undertaken using SCUBA on the JCMT. The properties, content and structure of cool to cold dust ($\sim$ 80 to 10 K) have been studied in Cygnus A, NGC 4374, M 82 and Centaurus A. The energy distribution of synchrotron electrons in Cygnus A and the cold dust outflows in M 82 have also been investigated. Summarised in Section 7.1 below are the thesis observational studies, results that were achieved and possible follow-on investigations (some already underway). Future SCUBA-polarimetry studies, that are related to the results in this thesis, are outlined in Section 7.1.1. A recently proposed post-thesis project, that was written in conjunction with an application for a postdoctoral fellowship, to exploit the high resolution and sensitivity of the soon to be commissioned *Space Infrared Telescope Facility* (*SIRTF*), is described in Section 7.2.

7.1 Outline of SCUBA Results and Follow-on Work

Millimetre and submm continuum observations of Cygnus A: The cool dust temperature in the galaxy was constrained between 37 and 85 K, corresponding to dust masses between $1.0 \times 10^8 M_\odot$ and $1.4 \times 10^6 M_\odot$ respectively (Robson et al., 1998). These results are consistent with very recent and better-constrained dust temperatures of 52 to 70 K and dust mass of $\sim 5 \times 10^6 M_\odot$ obtained using new *ISO* data at 60 through 180 μm (Haas et al., 1998; Leeuw & Robson, 1999), confirming that cool dust is responsible for the far-infrared (far-IR) to submm emission in Cygnus A, and perhaps other AGN of the same type. The lower dust mass limit of $\sim 10^6 M_\odot$ is comparable to the nuclear starburst galaxy M 82 and the upper limit to the extranuclear starburst galaxies Arp 220 and NGC 6240 as well as the Radio Quiet Quasars IZw 1, Mrk 1014 and Mrk 376. It is unclear whether the heating of the warm dust in Cygnus A is dominated by active star formation or the active galactic nucleus.

Detailed photometric observations of the two major hotspots (A & D) in Cygnus A showed that their spectral index extends smoothly to about 450μm (677 GHz), with no evidence of spectral steepening. The thesis shows that if the diffusion speed for the electrons responsible for this emission is about c, then a single particle acceleration mechanism can be responsible for the hotspot synchrotron emission. On the other hand, if the diffusion speed is significantly less than c, then multiple acceleration locations are probably required unless the magnetic field strength is significantly less than the equipartition value. Future observations using submm interferometers (e.g. the Submillimeter Array [SMA] on Mauna Kea) will narrow-down the parameter space in terms of the size of the emitting region.

Searching for diffusely distributed dust in the elliptical galaxy NGC 4374:

Following the suggestion that elliptical galaxies may contain diffusely distributed dust (Goudfrooij, 1994), a search for this was undertaken with submm imaging observations of the elliptical galaxy NGC 4374, using SCUBA (Leeuw et al., 2000). Low-level, diffusely distributed dust was not detected. However, due to the limiting sensitivity of SCUBA, the existence of this diffuse dust could not be ruled out. The 3σ upper limit on the $850\,\mu$m integrated flux within a region of about $2'$ diameter (just less than the SCUBA array) is 0.6 Jy, giving the flux density upper-limits on the undetected low, level diffuse dust and extended radio lobes. The detected emission at $850\,\mu$m is spatially unresolved (diameter $< 15''$), showing that the dust is confined to the central region of diameter < 1.5 kpc. Model fitting gives an angular extent of the dust to be $\sim 1''.5$ in diameter, which corresponds to a size-scale of only 0.15 kpc. If there is a co-mixing of the molecular gas and dust, this constrains the size of any molecular torus around the AGN core of NGC 4374 to around only 150 pc in diameter. Future high resolution observations using mm-submm interferometers (e.g. the SMA) and ground based mid-IR instruments (e.g. Michelle on UKIRT/GEMINI) should directly test these spatial-size constraints. Such observations were proposed for this thesis with the Owens Valley Radio Observatory but, unfortunately, the proposal was not approved. (A recent, successful proposal, that will be scheduled post this thesis, to use the GEMINI Telescope for a similar purpose is mentioned below.)

For the low-level emission, a strategy was devised to find better candidates for the follow-up programme. This has been proposed for observing time on the JCMT in collaboration with Dr. Anne Sansom of UCLan. Dr. Martin Haas, one of the collaborators in this project, is involved in a parallel far-IR emission project using *ISO* data. To pin-

down the non-thermal flux contribution to the submm-IR dust mission, complementary mm observations have been successfully proposed and are scheduled at the Nobeyama Radio Telescope in Japan. Searching and mapping the distribution of the diffuse dust is important, among other things, because the dust could affect metallicity (and thus age) determinations in elliptical galaxies. See Section 7.2 below for a detailed description of a recently proposed project to exploit the high resolution and sensitivity of the soon to be commissioned *SIRTF* in far-infrared observations of ellipticals.

Deep submm imaging of dust structures in NGC 5128 (Centaurus A): SCUBA imaging observations were obtained at 850 and 450μm covering the central 450″× 100″ ($\sim 8.0 \times 2.0$ kpc) of Centaurus A. The sensitive 850 and 450μm images include the first direct detection of emission from dust that is in the background or inner parts of NGC 5128 (Leeuw & Robson, 2000). The new images show that the submm continuum morphology and spectral index distribution of Centaurus A comprise four regions in the nuclear area and dust lane of the galaxy: non-thermal emission from the unresolved AGN core ($\alpha \approx 0$) and the inner-jet interacting with gas in the dust lane ($\alpha \approx 2$); and thermal emission from the *inner disc* of radii $\sim 90''$ ($2.5 \leq \alpha \leq 3.5$) and colder outer dust ($3.2 \leq \alpha \leq 4.2$), where $S_\nu \propto \nu^\alpha$ is computed between 450 and 850μm (Leeuw et al., 2002). Observing the submm jet in this case is interesting because the spectral index here is indicative of free-free continuum emission from interstellar gas that has been entrained and heated by the flow of relativistic particles from the nucleus (Brodie et al., 1983), and not a manifestation of the synchrotron relativistic radio jet itself. It is the first time this has been detected in the submm. The AGN core, which is clearly distinct from the extended emission, is most probably a low-luminosity blazar. The *inner disc* of radii 90″ has a high surface brightness and is reverse-S-shaped in the 850

and 450μm images. It coincides with the regions of intense 7 and 15μm continuum, dense molecular gas emission, and a high concentration of Paα sources indicative of active star formation. The IR and submm images appear to a large extent to reveal the same material, as predicted by a geometric warped disc model consisting of tilted rings (Quillen et al., 1993), a scenario that seems more plausible than that recently proposed by Mirabel et al. (1999) suggesting that the mid-IR emission is primarily from a bar, with a structure that is different from the extended warped disc alone.

Follow-up molecular line observations to constrain the dynamics of the Centaurus A *inner disc* are underway at the JCMT, in collaboration with Dr. Henry Matthews. Furthermore, *high* resolution mid-IR observations have been successfully proposed and will be scheduled to use T-RECS, the mid-IR imager on GEMINI-South telescope to observe the physical details of this structure and the nuclear components in Centaurus A. There are plans for similar *high* resolution mid-IR observations of other dust lane AGN, to better distinguish their morphology as a circumnuclear ring or bar, determine whether bars are a common feature of such galaxies and therefore whether accretion is sustained by funnelling in a bar or which of the other structures/mechanisms are more plausible in this regard. If the mid-IR emission is from a circumnuclear ring, determining its orientation might indicate the role the ring plays in nuclear activity in Centaurus A and similar objects. (Also see Section 7.2 below for a proposed complementary project in far-infrared observations that will exploit the high resolution and sensitivity of the soon to be commissioned *SIRTF*.)

Flat mm-to-submm spectra have been observed in the core of both Centaurus A and NGC 4374. If indeed the submm core spectra in these objects are flat as the observations indicate, the results would support the hypothesis that *flat* spectra are a characteristic

of low-luminosity blazars (Hawarden et al., 1993; Kellermann et al., 1997). In terms of the blazar/FR I unification scheme of AGN, a mis-aligned blazar (or BL Lac) object in the core is consistent with the FR I morphology that is seen in large-scale radio maps of NGC 4374 and Centaurus A. Submm observations of a larger sample of these objects are needed to provide a more definitive test that has implications on the blazar/FR I unification scheme of AGN.

Properties and Outflows of Cold Dust in M 82: Deep SCUBA 350, 450, 750 and 850 μm imaging observations have been presented of the dust-laden nuclear region and submm halo of M 82. The displayed maps include co-added data that were mined from the SCUBA Data Archive, resulting in detections of low-level emission out to 1.5 kpc for the first time in the 850 μm continuum of this galaxy, i.e. $\sim$ 160 pc radius farther-out than other recent studies (see Section 6.3).

The overall, extended submm morphology of M 82 generally resembles the optical picture; however, the submm morphology is much smoother than the optical, and some prominent dust cloud and filamentary lanes that are seen in the optical are not obvious in the submm continuum (see Section 6.3.1). One reason for this relative correspondence is that the optically-thin submm continuum represents total emission from the entire galactic columns of dust in the line of sight, while the optical morphology of dust, because the dust is typically seen *obscuring* stellar light, represents only the dust in certain spatial stratifications (usually the foreground) of the observed line-of-sight columns. The overall submm low-level morphology and nuclear spectral index distribution have a general north-south asymmetry that can be associated with filamentary H_α winds and CO and X-ray outflows that have been detected in M 82, confirming the simple interpretation (e.g. Leeuw et al., 1998; Alton et al., 1999) that the asymmetric, filamentary structures

in the submm maps were a manifestation of associated outflows of dust grains from the galactic nucleus into the halo.

A comparative analysis of submm to high-resolution CO (1-0) morphology showed that resolved peaks in the CO maps could be associated with unresolved features in the submm maps (see Section 6.3.2). Assuming that the CO and dust grains were well-mixed, it was concluded that BIMA maps gave a reasonable indication of how dust emission might appear at higher resolution. The submm morphology and spectral index distribution evidence in this thesis disfavour the commonly assumed interpretation that submm emission arises from a dusty torus in M 82 (see Sections 6.4 and 6.5). The more likely interpretation is that the emission arises from an east-west asymmetric distribution of dust concentrations that are in regions of different star-formation environments, as has been reported from various studies using data at other wavelengths. It is clear that the CO contamination to higher-frequency continuum may be as significant as the 47% estimated for the SCUBA-850 μm band by Seaquist & Clark (2001) and detailed investigations of the 450 and 350 μm observations are needed to establish their respective contaminations levels (see Section 6.5.2).

Preliminary analyses show that Maximum Entropy Method (MEM) deconvolution or observations with the 180″ chop throw respectively are not useful for uniquely enhancing the resolution of the SCUBA maps or improving the detection of the submm continuum in M 82 (see Section 6.6). Never the less, extended assessment of the use and implementation of MEM–re-processing and obtaining maps with the 180″ chop throw for SCUBA observations may be worthy of further investigation in the future. Targeted beam-map observations of JCMT primary sources with 180″ (and also 150″) chop throws would characterise SCUBA results at these large throws and help establish their general

usefulness.

Some interesting points have been raised about the origin and structure of the submm emission in M 82. A more quantitative spatial-correspondence and optical-depth analysis (and radiative modelling) of the submm versus optical images is needed to make definite assertions about the origin of any of the features seen in the compared maps. Future higher resolution observations of dust that will soon be possible with the commissioning of the Submillimeter Array (Moran, 1996) and the Space Infrared Telescope (e.g. Deutsch & Bicay, 2000) will provide data that will allow inferred structure at small-scales to be tested by direct observations. It is re-emphasised that the results of M 82 are presented as work in progress, and therefore some the conclusions are rather *preliminary.*

In summary, the thesis has used SCUBA in a submm continuum imaging study of four, nearby active galaxies, directly revealing the ringed, spiral structure of the optical dust-lane in the merger-remnant galaxy Centaurus A, placing upper-limits on diffuse dust in the elliptical galaxy NGC 4374, constraining the cold dust temperature and dust content in the double-lobed radio galaxy Cygnus A, and showing morphological and spectral index distribution evidence of nuclear-dust concentrations and outflows in the starburst galaxy M 82. The results have implications on hypotheses for interactions of star formation and nuclear activity with dust and thus the general role of the interstellar medium in galactic evolution.

7.1.1 Outline of Future Submm Polarimetry with SCUBA

The plans for future submm observations of the galaxies described above include polarimetry with SCUBA (some that are already underway or proposed for telescope time at the JCMT) to study the alignment of the emitting dust grains by galactic magnetic

fields. The average polarization position angle of the detected dust re-radiation is directly related to the average orientation of the magnetically-aligned grains; and can therefore be used to infer structure and common origin of the emitting grains. For example, imaging polarimetry of Centaurus A obtained with the SCUBA polarimeter will be used to investigate the relationship of the submm emission detected from the inner parts of the galaxy and the foreground grains seen in optical obscuration. Similar single-pixel polarimetry will be undertaken with SCUBA to investigate the relation any detected polarization position angles of the centrally concentrated submm continuum from the cores of Cygnus A and NGC 4374 have in relation to the orientations of the optical dust lanes in those galaxies. The percentage of polarization will be used to distinguish any non-thermal component of the detections, as the non-thermal mechanisms (e.g. synchrotron) are expected to have much higher (up to $\sim 30\%$) linear polarizations than re-radiation from aligned grains ($\lesssim 6\%$). From these polarimetry observations, the general role of the magnetic fields themselves on galactic evolution can be studied.

7.2 Plans for Future Observational Work with *SIRTF*

Properties of the Infrared Continuum in Local Elliptical and Active Galaxies – *Probing Merger Formation and Host-Nuclear Activity Interaction Hypotheses:* The currently popular evolution hypothesis of elliptical galaxies is that they form by mergers of gas-rich spirals (Schweizer 1998) that go through a dust-rich and far-infrared bright merging phase prior to relaxation to a normal elliptical. Mergers presumably happen to all types of galaxies, but evidence of these events should be more obvious in ellipticals because of the general paucity of the interstellar medium (ISM) and because the accretion of cold gas is thought to fuel the central dormant engine in these systems, causing them to

become active galaxies and radio sources (cf. Knapp 1989). Activity in the galactic.nuclei can then itself affect the ISM (e.g. Krolik 2001). Detections of the diffuse and compact emission from nearby elliptical and active galaxies at the unparalleled infrared sensitivity and spatial resolution that will be made possible by the commissioning of *SIRTF*[1] will permit direct comparisons with data of similar resolution at other wavelengths and thus allow the probing of galactic evolution and host-nuclear activity interaction hypotheses.

Cold Dust in Elliptical Galaxies – *Testing the Merger Formation Hypothesis:* [2] If it is true that elliptical galaxies form by mergers of gas-rich spirals, then some remnants of dust from the merger should be seen, at the very least, in young ellipticals with no hot ISM (Sansom, Hibbard and Schweizer 2000). The older ellipticals are expected to have little or no dust since the hot gas haloes in these galaxies destroy the dust by sputtering (Goudfrooij 1994). These predicted evolutionary trends can be tested by combining an observational programme of well determined dust mass estimates proposed here, available X-ray data (e.g. Sansom et al. in preparation) and relative age data from morphological fine structure (e.g. Schweizer & Seitzer 1992) and spectroscopic age indicators (e.g. Terlevich & Forbes 2001).

The *SIRTF* sensitivity is 100 times better and spatial resolution is at lease 3 times greater than any of the predecessor mid- to far-infrared instruments and therefore will allow unprecedented constraints on the existence and locations of cool to cold ($\sim$ 90 to 20 K) dust in ellipticals. The far-infrared *SIRTF* flux from dust is optically thin and

[1] *Space Infrared Telescope Facility* (*SIRTF*) is the final element in NASA's Great Observatories Program, and is an important scientific and technical cornerstone of the new Astronomical Search for Origins Program. The space-borne, cryogenically-cooled infrared observatory will be launch in July 2002.

[2] The proposed *SIRTF* programme of cold dust in elliptical galaxies is a mm-to-infrared–multiwave-observation programme that, if successful, is to be undertaken in association with proposed observations on the JCMT in collaboration with Sansom et al., a paralleled far-IR emission project using *ISO* data in collaboration with Haas et al., and complementary mm observations proposed at the Nobeyama Radio Telescope.

therefore can be detected much deeper in the source than emission at the shorter wavelengths, potentially revealing source structure not previously seen. Recent observational evidence from SCUBA detections of the optically thin dust emission from Centaurus A (see Figure 7.1a) shows a spiral feature in the optical dust lane and dust emission in the inner parts of galaxy that were revealed for the first time in this merger-remnant galaxy (Leeuw et al. 2002). *SIRTF* will match and in some cases achieve better resolution and sensitivity than the current submm studies, providing complementary fluxes in the infrared for spectral energy distribution studies. For the optically thin dust, the far-infrared *SIRTF* fluxes are directly proportional to the dust mass (for a given temperature and distance). By fitting the fluxes to the spectral energy distribution, the dust temperatures and hence dust masses can be determined.

Some dust has been detected in numerous elliptical galaxies. About 40% of ellipticals have dust lanes that are seen obscuring optical stellar light (Sadler & Gerhard 1985). A similar percentage of bright ellipticals produce copious infrared emission and has been detected by *IRAS* at 100 μm (Knapp et al. 1989), with the far-infrared colours $S_{60\,\mu m}/S_{100\,\mu m} \sim 1/3$ as expected from cool dust. However, the dust masses estimated from the *IRAS* fluxes are typically an order of magnitude higher than is detected in dust lanes via optical extinction (Goudfrooij 1994). The *IRAS excess* fluxes suggest the presence of cool, diffusely distributed dust that is not detected in the dust lanes (Goudfrooij 1994). By assuming lower dust temperature ($\sim$19 K) than was detected by *IRAS*, even larger dust masses can be inferred in ellipticals (Knapp et al. 1991).

ISO and SCUBA observations showed fairly convincing evidence for very cold ($\sim$15 K) dust in spiral galaxies (e.g. Haas et al. 1998; Dunne & Eales 2001), that increased the estimated dust masses in spirals by about a factor of three. For observations of ellipticals

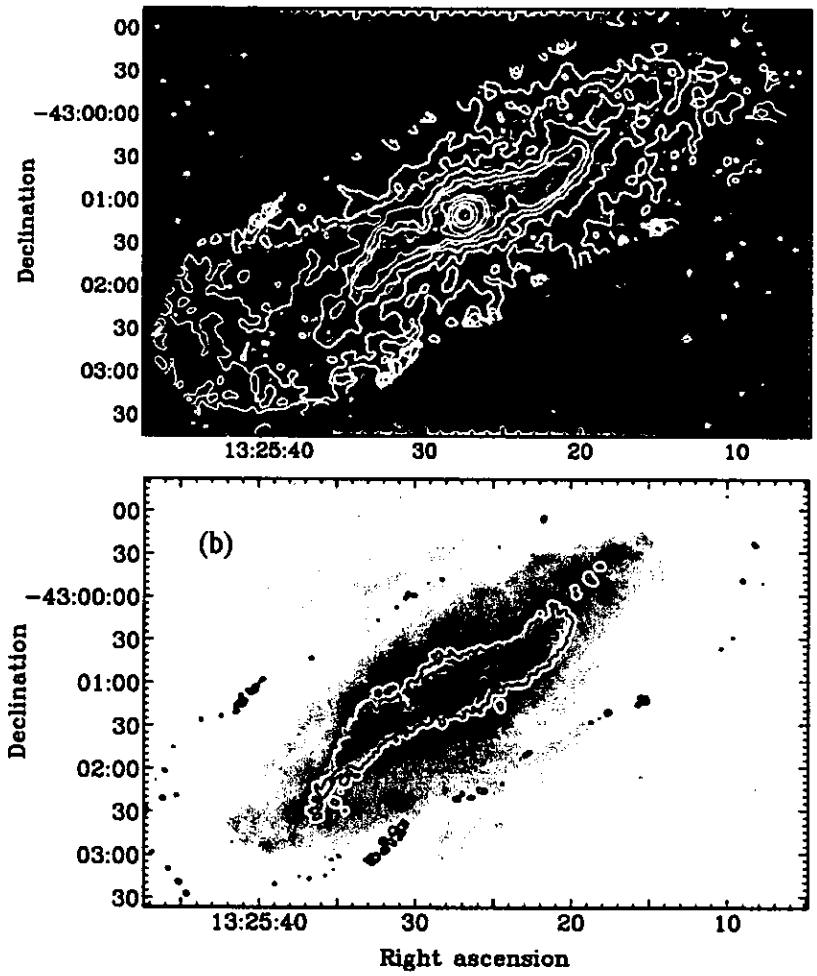

Figure 7.1: Contours of the 450μm image superposed on, from top to bottom, (a) an optical waveband image of Centaurus A, digitised from the *IIIaJ* emulsion photographic plates which are sensitive to emission between 395 and 540 nm wavelengths and (b) a 7μm ISOCAM negative image, courtesy of the Anglo-Australian Observatory and Mirabel et al. (1999) respectively (Leeuw et al., 2002, see Chapter 5).

the *ISO* sensitivities are limited and have produced only isolated but interesting detections of cold dust. The preliminary results from the *ISO* 200 μm observations, that need to be confirmed with sensitive far-infrared *SIRTF* and also submm SCUBA observations, suggest that ellipticals show a range of dust properties (e.g. Haas in preparation). Complementary mm and submm (e.g. with SCUBA) observations are important for sampling emission from any colder dust that emits longward of the infrared and for pinning down any non-thermal contribution to the infrared spectrum. By decomposing the radio to

infrared spectral energy distribution, any non-thermal contribution to the flux can be subtracted and dust temperatures (here including very cold dust) as well as the best constrained dust masses to date can be determined. The angular size of the SCUBA beams at 350 and 450 μm are very similar to those of *SIRTF* at 70 and 160 μm, therefore the submm and IR observations undertaken with these instruments will sample similar emission regions of most probably related mechanisms, making their complementary use not only essential but also technically very sensible! In addition to the SCUBA observations, other complementary submm observations can be proposed with new bolometer arrays at the Heinrich-Hertz Submillimeter Telescope in Arizona and Caltech Submillimeter Observatory in Hawaii.

Establishing the presence and properties of extended, cold dust is important for the understanding of the evolutionary state of ellipticals and the interstellar medium itself. It will be interesting to see if cold dust (< 25 K) also survives in the more hostile environment of ellipticals galaxies as well, perhaps providing reservoirs for star formation and nuclear activity? Constraining the total dust content and thus its extinction is also important for separating the effects of dust and those of increased heavy element abundance, or increased age of the stellar population, in ellipticals. An observational programme that investigates the dust in infrared and submm emission will allow a direct and independent estimation of the effects of dust on broadband colours of ellipticals, which is critical for accurate dust mass determinations expected from future broadband, large area optical surveys (e.g. from VISTA). Dust extinction can mimic the effects of increased heavy element abundance or increased age of the stellar population in ellipticals. For example the diffusely distributed dust found by Goudfrooij (1994) is enough to explain apparent age changes across some galaxies in his sample. Therefore future broadband, large area

surveys will benefit from accurately knowing the masses of dust present in galaxies.

Infrared Properties at Local Emitting Regions –*Probing Host–Nuclear Activity Interactions:* High resolution *SIRTF* studies of high luminous infrared ellipticals and active galaxies will determine the detailed infrared emission morphology in the central kpc scales of these galaxies. In particular, the studies of optical dust lanes that are common in these objects at these scales will determine, if the infrared emission exclusively follows the dust lane absorption of optical light and if it has any interesting structure. The far-infrared (and submm) dust re-radiation is optically thin and this can be exploited to expose galactic material in the inner parts and structure not seen in the optical and near-infrared bands. As shown in Figure 7.1b, recent *ISO* and SCUBA observations of Centaurus A by Mirabel et al. 1999 and Leeuw et al. 2002 respectively showed that the dust lane of the galaxy, which appears chaotic in optical maps, is actually a prominent, elongated spiral feature that may be a circumnuclear ring or bar and extends across the center of the galaxy out to a radius of ~ 1 kpc. This feature is associated with a concentration of blue stars indicative of high star-formation and its spiral structure may be the remnant of a merger event that lead to nuclear activity in Centaurus A. If the feature is a bar as suggested by Mirabel et al. 1999, it may funnel material into the active galactic nucleus. Remarkable spatial correspondence between images obtained at the mid-IR by Mirabel et al. 1999 and the submm demonstrate that infrared emission from structures such as this will be revealed by *SIRTF* observations of dust lanes at unprecedented spatial detail and sensitivity. Spectral index distribution analysis from infrared (and submm) flux ratios will constrain the emission mechanisms in these structures. Morphological comparisons with data at other wavelengths will reveal associations the dust structures

have with common tracers of other activities in the galaxies e.g. H I for star-formation, X-ray for nuclear activity and cooling flows, optical and near-infrared for stellar activity.

High resolution *SIRTF* studies of nuclear regions in elliptical and active galaxies will distinguish components and mechanisms responsible for the mid- to far-infrared emission. From both dust temperature fits and direct imaging spatial information, some recent far-infrared and submm observations (e.g. Leeuw, Sansom & Robson 2000; Rupen et al. 1997) of a few ellipticals have indicated some emission at the respective wavelengths is concentrated at the core of the galaxies, well within a few hundred parces. The emission is more concentrated than the stellar component, suggesting that the emitting material resulted from something other than mass-loss in late type stars. The thermal temperature fits are consistent with emission from the warm to cool ($\sim$ 250 to 50 K) outer regions of circumstellar tori. High resolution *SIRTF* observations at selected bands could confirm the existence of the tori in these objects; in that case, the ratio of fluxes at the different bands could be used to provide temperature information across the tori. Information about the incidence and inclinations of the tori in relation to nuclear activity would be used to access any physical role they play in the relevant activity. For example, are the tori commonly found perpendicular to active nuclei jets and if so do they direct the jets? The flux ratios in some sources may alternatively indicate that the infrared emission is the high frequency non-thermal component of the radio synchrotron or inverse-Compton emission from the active nuclei cores. In the case of non-thermal emission from both the nuclear cores and knots in the jets, the infrared fluxes will be important for constraining the high frequency spectral steeping due to synchrotron high energy loses (e.g. Carilli et al. 1999) and therefore give age estimates of the sources. It is noted that the studies by Leeuw, Sansom & Robson 2000 and Rupen et al. 1997 that detected centrally concentrated

emission in some ellipticals did not rule out low-level far-infrared and submm emission from cold, diffuse dust as proposed for sensitive *SIRTF* imaging above.

Source Selection: Experience from some infrared and submm studies (e.g. Leeuw, Sansom & Robson 2000; Knapp & Patten 1991; Haas in preparation) indicates some useful selection criteria for choosing targets of early-type galaxies in which to detect cool dust. The galaxies need to be relatively strong infrared sources (i.e. have *IRAS* detections at 100 or 60 μm and inferred dust masses of $> 10^5 M_\odot$), nearby ($\leq 40-200$ Mpc) in order to maximise expected low-level fluxes and to resolve emitting regions, and low radio emitters (to avoid confusion of sources of emission in the submm). For the proposed study the sample will include a few radio-loud objects to ensure useful detections for the host-nuclear activity interaction part of the investigation and representative selections across the elliptical classes. Consideration will also be made to choose galaxies with published complementary data that will be needed for useful spectral energy studies and morphological comparisons. These will include galaxies from the samples of Knapp & Patten 1991, Goudfrooij 1994, Bregman et al. 1998. In addition to observations of specifically selected targets for this programme, relevant data will be used from the *SIRTF* First Look and Legacy Science Programmes. It is anticipated that the results from the programme proposed here will reveal unprecedented detailed and sensitive infrared continuum from elliptical and active galaxies, providing unparalleled constraints on the properties of the emission that will allow the probing of the merger formation and host-nuclear activity hypotheses in the target galaxies as well as the nature of the emission itself.

Bibliography

Achtermann, J. M. & Lacy, J. H. 1995, ApJ, 439, 163

Alexander, D. M., Efstathiou, A., Hough, J. H., Aitken, D. K., Lutz, D., Roche, P. F., & Sturm, E. 1999, MNRAS, 310, 78

Alonso-Herrero, A., Rieke, M. J., Rieke, G. H., & Kelly, D. M. 2001, Ap&SS, 276, 1109

Alton, P. B., Davies, J. I., & Bianchi, S. 1999, A&A, 343, 51

Antonucci, R. R. J. & Miller, J. S. 1985, ApJ, 297, 621

Aumann, H. H., Fowler, J. W., & Melnyk, M. 1990, AJ, 99, 1674

Baade, W. & Minkowski, R. 1954, ApJ, 119, 215

Bailey, J., Sparks, W. B., Hough, J. H., & Axon, D. J. 1986, Nature, 322, 150

Barger, A. J., Cowie, L. L., Sanders, D. B., Fulton, E., Taniguchi, Y., Sato, Y., Kawara, K., & Okuda, H. 1998, Nature, 394, 248

Barthel, P. D. 1989, ApJ, 336, 606

Baum, S. A., Heckman, T. M., & van Breugel, W. 1992, ApJ, 389, 208

Bell, A. R. 1978, MNRAS, 182, 443

Blandford, R. D. & Rees, M. J. 1974, MNRAS, 169, 395

Block, D. L. & Sauvage, M. 2000, A&A, 353, 72

Bolton, J. G., Stanley, G. J., & Slee, O. B. 1949, Nature, 164, 101

Bower, G. A., Heckman, T. M., Wilson, A. S., & Richstone, D. O. 1997, ApJ, 483, L33

Bradford, C. M., Stacey, G. J., Nikola, T., Swain, M. R., Bolatto, A. D., Jackson, J. M., Savage, M. L., & Davidson, J. A. 1999, in American Astronomical Society Meeting, Vol. 195, 7304

Bridle, A. H. & Perley, R. A. 1984, ARA&A, 22, 319

Brodie, J., Koenigl, A., & Bowyer, S. 1983, ApJ, 273, 154

Brown, L. M. J., Robson, E. I., Gear, W. K., & Smith, M. G. 1989, ApJ, 340, 150

Bryant, J. J. & Hunstead, R. W. 1999, MNRAS, 308, 431

Canizares, C. R., Fabbiano, G., & Trinchieri, G. 1987, ApJ, 312, 503

Carilli, C. L. & Barthel, P. D. 1996, A&A Rev., 7, 1

Carilli, C. L. & Harris, D. E. 1996, Cygnus A – Study of a Radio Galaxy (Cambridge University Press)

Carilli, C. L., Kurk, J. D., van der Werf, P. P., Perley, R. A., & Miley, G. K. 1999, AJ, 118, 2581

Carilli, C. L., Perley, R., Harris, D. E., & Barthel, P. D. 1998, Physics of Plasmas, Volume 5, Issue 5, May 1998, pp.1981-1990, 5, 1981

Carilli, C. L., Perley, R. A., Dreher, J. W., & Leahy, J. P. 1991, ApJ, 383, 554

Charmandaris, V., Combes, F., & van der Hulst, J. M. 2000, A&A, 356, L1

Chevalier, R. A. & Clegg, A. W. 1985, Nature, 317, 44

Clarke, D. A., Burns, J. O., & Norman, M. L. 1992, ApJ, 395, 444

Cunningham, C. T., Ade, P. A. R., Robson, E. I., & Radostitz, J. V. 1984, MNRAS, 211, 543

de Grijs, R. 2001, Astronomy and Geophysics, 42, 12

Deutsch, M. & Bicay, M. D. 2000, Ap&SS, 273, 187

Devine, D. & Bally, J. 1999, ApJ, 510, 197

Dietz, R. D., Gehrz, R. D., Jones, T. J., Grasdalen, G. L., Smith, J., Gullixson, C., & Hackwell, J. A. 1989, AJ, 98, 1260

Dietz, R. D., Smith, J., Hackwell, J. A., Gehrz, R. D., & Grasdalen, G. L. 1986, AJ, 91, 758

Draine, B. T. 1990, in ASSL Vol. 161: The Interstellar Medium in Galaxies, 483–492

Draine, B. T. & Salpeter, E. E. 1979, ApJ, 231, 77

Duncan, W. D., Sandell, G., Robson, E. I., Ade, P. A. R., & Griffin, M. J. 1990, MNRAS, 243, 126

Duschl, W. J., Strittmatter, P. A., & Biermann, P. L. 2000, A&A, 357, 1123

Eales, S. A., Alexander, P., & Duncan, W. D. 1989, MNRAS, 240, 817

Eckart, A., Cameron, M., Rothermel, H., Wild, W., Zinnecker, H., Rydbeck, G., Olberg, M., & Wiklind, T. 1990, ApJ, 363, 451

Eckart, A., Wild, W., & Ageorges, N. 1999, ApJ, 516, 769

Edmunds, M. G. 2001, MNRAS, 328, 223

Edmunds, M. G. & Eales, S. A. 1998, MNRAS, 299, L29

Emerson, D. T. 1995, in ASP Conf. Ser. 75: Multi-Feed Systems for Radio Telescopes, 309

Emerson, J. P., Clegg, P. E., Gee, G., Griffin, M. J., Cunningham, C. T., Brown, L. M. J., Robson, E. I., & Longmore, A. J. 1984, Nature, 311, 237

Förster Schreiber, N. M. 2000, New Astronomy Review, 44, 263

Fanaroff, B. L. & Riley, J. M. 1974, MNRAS, 167, 31P

Fullmer, L. & Londsdale, C. J. 1989, Cataloged galaxies and quasars observed in the IRAS survey (Pasadena: Jet Propulsion Laboratory, Version 2)

García-Burillo, S., Martín-Pintado, J., Fuente, A., & Neri, R. 2001, ApJ, 563, L27

Gear, W. K. 1988, in Millimetre and Submillimetre Astronomy, 307–338

Gear, W. K., Robson, E. I., Ade, P. A. R., Smith, M. G., Clegg, P. E., Cunningham, C. T., Griffin, M. J., Nolt, I. G., & Radostitz, J. V. 1984, ApJ, 280, 102

Gear, W. K., Robson, E. I., Gee, G., & Nolt, I. G. 1985, MNRAS, 217, 281

Golombek, D., Miley, G. K., & Neugebauer, G. 1988, AJ, 95, 26

Goudfrooij, P. 1994, PhD thesis, Ph. D. thesis, University of Amsterdam, The Netherlands

Goudfrooij, P. & de Jong, T. 1995, A&A, 298, 784

Goudfrooij, P., Hansen, L., Jorgensen, H. E., & Norgaard-Nielsen, H. U. 1994, A&AS, 105, 341

Graham, J. A. 1979, ApJ, 232, 60

Greaves, J. S., Holland, W. S., Moriarty-Schieven, G., Jenness, T., Dent, W. R. F., Zuckerman, B., McCarthy, C., Webb, R. A., Butner, H. M., Gear, W. K., & Walker, H. J. 1998, ApJ, 506, L133

Griffin, M. J. & Orton, G. S. 1993, Icarus, 105, 537

Guesten, R., Serabyn, E., Kasemann, C., Schinckel, A., Schneider, G., Schulz, A., & Young, K. 1993, ApJ, 402, 537

Gull, S. F. & Skilling, J. 1983, in Indirect Imaging – Measurement and Processing for Indirect Imaging. Proceedings of an International Symposium held in Sydney, Australia, August 30-September 2, 1983. Editor, J.A. Roberts; Publisher, Cambridge University Press, Cambridge, England, 267

Haas, M., Chini, R., Meisenheimer, K., Stickel, M., Lemke, D., Klaas, U., & Kreysa, E. 1998, ApJ, 503, L109

Hajian, A. R. ., Phillips, J. A., & Terzian, Y. 1996, ApJ, 467, 341

Hajian, A. R., Phillips, J. A., & Terzian, Y. 1995, ApJ, 446, 244

Hargrave, P. J. & Ryle, M. 1974, MNRAS, 166, 305

Hawarden, T. G., Sandell, G., Matthews, H. E., Friberg, P., Watt, G. D., & Smith, P. A. 1993, MNRAS, 260, 844

Hildebrand, R. H. 1983, QJRAS, 24, 267

Ho, L. C., Filippenko, A. V., & Sargent, W. L. W. 1996, in ASP Conf. Ser. 91: IAU Colloq. 157: Barred Galaxies, 188

Holland, W. S., Greaves, J. S., Zuckerman, B., Webb, R. A., McCarthy, C., Coulson, I. M., Walther, D. M., Dent, W. R. F., Gear, W. K., & Robson, I. 1998, Nature, 392, 788

Holland, W. S., Robson, E. I., Gear, W. K., Cunningham, C. R., Lightfoot, J. F., Jenness, T., Ivison, R. J., Stevens, J. A., Ade, P. A. R., Griffin, M. J., Duncan, W. D., Murphy, J. A., & Naylor, D. A. 1999, MNRAS, 303, 659

Hughes, D. H., Dunlop, J. S., & Rawlings, S. 1997, MNRAS, 289, 766

Hughes, D. H., Gear, W. K., & Robson, E. I. 1994, MNRAS, 270, 641

Hughes, D. H., Robson, E. I., Dunlop, J. S., & Gear, W. K. 1993, MNRAS, 263, 607

Hughes, D. H., Robson, E. I., & Gear, W. K. 1990, MNRAS, 244, 759

Hughes, D. H., Serjeant, S., Dunlop, J., Rowan-Robinson, M., Blain, A., Mann, R. G., Ivison, R., Peacock, J., Efstathiou, A., Gear, W., Oliver, S., Lawrence, A., Longair, M., Goldschmidt, P., & Jenness, T. 1998, Nature, 394, 241

Hui, X., Ford, H. C., Ciardullo, R., & Jacoby, G. H. 1993, ApJ, 414, 463

Israel, F. P. 1998, A&A Rev., 8, 237

Israel, F. P., van der Werf, P. P., & Tilanus, R. P. J. 1999, A&A, 344, L83

Jenkins, C. J., Pooley, G. G., & Riley, J. M. 1977, MmRAS, 84, 61

Jenness, T., Lightfoot, J. F., & Holland, W. S. 1998, Proc. SPIE, 3357, 548

Johnstone, D. & Bally, J. 1999, ApJ, 510, L49

Joy, M., Harvey, P. M., Tollestrup, E. V., Sellgren, K., McGregor, P. J., & Hyland, A. R. 1991, ApJ, 366, 82

Kellermann, K. I., Zensus, J. A., & Cohen, M. H. 1997, ApJ, 475, L93

Klaas, U., Haas, M., Heinrichsen, I., & Schulz, B. 1997, A&A, 325, L21

Knapp, G. R., Bies, W. E., & van Gorkom, J. H. 1990, AJ, 99, 476

Knapp, G. R. & Patten, B. M. 1991, AJ, 101, 1609

Kraft, R. P., Forman, W., Jones, C., Kenter, A. T., Murray, S. S., Aldcroft, T. L., Elvis, M. S., Evans, I. N., Fabbiano, G., Isobe, T., Jerius, D., Karovska, M., Kim, D., Prestwich, A. H., Primini, F. A., Schwartz, D. A., Schreier, E. J., & Vikhlinin, A. A. 2000, ApJ, 531, L9

Krichbaum, T. P., Alef, W., Witzel, A., Zensus, J. A., Booth, R. S., Greve, A., & Rogers, A. E. E. 1998, A&A, 329, 873

Kronberg, P. P., Biermann, P., & Schwab, F. R. 1985, ApJ, 291, 693

Kuno, N. & Matsuo, H. 1997, PASJ, 49, 265

Laing, R. A. & Bridle, A. H. 1987, MNRAS, 228, 557

Leeuw, L. L., Hawarden, T. G., Matthews, H. E., Robson, E. I., & Eckart, A. 2002, ApJ, 565, 131

Leeuw, L. L., Hughes, D. H., & Robson, E. I. 1998, in IAU Symposium, Vol. 192, E22

Leeuw, L. L. & Robson, E. I. 1999, in IAU Symp. 194: Activity in Galaxies and Related Phenomena, Vol. 194, 179

Leeuw, L. L. & Robson, E. I. 2000, in Imaging at Radio through Submillimeter Wavelengths. Edited by Jeff Mangum. Publisher: The Astronomical Society of the Pacific, Conference Series, 2000. The conference was held June 6-8, 1999, in Tucson, Arizona., E40

Leeuw, L. L., Sansom, A. E., & Robson, E. I. 2000, MNRAS, 311, 683

Linfield, R. 1985, ApJ, 295, 463

Longair, M. S. 1997, High energy astrophysics. Vol.2: Stars, the galaxy and the interstellar medium (Cambridge: Cambridge University Press, 2nd edition, 1st reprint)

Low, F. J., Young, E., Beintema, D. A., Gautier, T. N., Beichman, C. A., Aumann, H. H., Gillett, F. C., Neugebauer, G., Boggess, N., & Emerson, J. P. 1984, ApJ, 278, L19

Lynds, C. R. & Sandage, A. R. 1963, ApJ, 137, 1005

Malin, D. F., Quinn, P. J., & Graham, J. A. 1983, ApJ, 272, L5

Marconi, A., Schreier, E. J., Koekemoer, A., Capetti, A., Axon, D., Macchetto, D., & Caon, N. 2000, ApJ, 528, 276

Martin-Pintado, J., Gaume, R. A., Johnston, K. J., & Bachiller, R. 1995, ApJ, 446, 687

Masson, C. R. 1994, in ASP Conf. Ser. 59: IAU Colloq. 140: Astronomy with Millimeter and Submillimeter Wave Interferometry, 87

Mirabel, I. F., Laurent, O., Sanders, D. B., Sauvage, M., Tagger, M., Charmandaris, V., Vigroux, L., Gallais, P., Cesarsky, C., & Block, D. L. 1999, A&A, 341, 667

Moran, J. M. 1996, in American Astronomical Society Meeting, Vol. 188, 4605

Muxlow, T. W. B., Pedlar, A., Wilkinson, P. N., Axon, D. J., Sanders, E. M., & de Bruyn, A. G. 1994, MNRAS, 266, 455

Nakai, N., Hayashi, M., Handa, T., Sofue, Y., Hasegawa, T., & Sasaki, M. 1987, PASJ, 39, 685

Neininger, N., Guelin, M., Klein, U., Garcia-Burillo, S., & Wielebinski, R. 1998, A&A, 339, 737

Nicholson, R. A., Bland-Hawthorn, J., & Taylor, K. 1992, ApJ, 387, 503

Orton, G. S. 1986, Science, 231, 836

Pacholczyk, A. G. 1970, Radio astrophysics. Nonthermal processes in galactic and extragalactic sources (San Francisco: Freeman)

Perley, R. A., Dreher, J. W., & Cowan, J. J. 1984, ApJ, 285, L35

Petitpas, G. R. & Wilson, C. D. 2000, ApJ, 538, L117

Pierce-Price, D., Richer, J. S., Greaves, J. S., Holland, W. S., Jenness, T., Lasenby, A. N., White, G. J., Matthews, H. E., Ward-Thompson, D., Dent, W. R. F., Zylka, R., Mezger, P., Hasegawa, T., Oka, T., Omont, A., & Gilmore, G. 2000, ApJ, 545, L121

Quillen, A. C., de Zeeuw, P. T., Phinney, E. S., & Phillips, T. G. 1992, ApJ, 391, 121

Quillen, A. C., Graham, J. R., & Frogel, J. A. 1993, ApJ, 412, 550

Rieke, G. H. & Lebofsky, M. J. 1981, ApJ, 250, 87

Roberts, M. S., Hogg, D. E., Bregman, J. N., Forman, W. R., & Jones, C. 1991, ApJS, 75, 751

Robson, E. I. 1996, Active Galactic Nuclei (New York, NY: Wiley, Chichester: Praxis Publishing)

Robson, E. I. 2001, in IAU Colloq. 184: AGN Surveys, E27

Robson, E. I., Leeuw, L. L., Stevens, J. A., & Holland, W. S. 1998, MNRAS, 301, 935

Robson, E. I., Litchfield, S. J., Gear, W. K., Hughes, D. H., Sandell, G., Courvoisier, T. J. ., Paltani, S., Valtaoja, E., Terasranta, H., Tornikoski, M., Steppe, H., & Wright, M. C. H. 1993, MNRAS, 262, 249

Rowan-Robinson, M. 1992, MNRAS, 258, 787

Salter, C. J., Chini, R., Haslam, C. G. T., Junor, W., Kreysa, E., Mezger, P. G., Spencer, R. E., Wink, J. E., & Zylka, R. 1989, A&A, 220, 42

Sandell, G. . 1994, MNRAS, 271, 75

Sandell, G. 1998, JAC WEB pages, 271, 75

Sanders, D. B., Phinney, E. S., Neugebauer, G., Soifer, B. T., & Matthews, K. 1989, ApJ, 347, 29

Schiminovich, D., van Gorkom, J. H., van der Hulst, J. M., & Kasow, S. 1994, ApJ, 423, L101

Schreier, E. J., Capetti, A. ., Macchetto, F., Sparks, W. B., & Ford, H. J. 1996, ApJ, 459, 535

Schreier, E. J., Capetti, A., Macchetto, F., Sparks, W. B., & Ford, H. J. 1998, STScI Electronic Press Release STScI-PRC98-14, 459, 535

Seaquist, E. R. & Clark, J. 2001, ApJ, 552, 133

Seaquist, E. R. & Odegard, N. 1991, ApJ, 369, 320

Shen, J. & Lo, K. Y. 1995, ApJ, 445, L99

Shopbell, P. L. & Bland-Hawthorn, J. 1998, ApJ, 493, 129

Smail, I., Ivison, R. J., & Blain, A. W. 1997, ApJ, 490, L5

Sparks, W. B., Wall, J. V., Thorne, D. J., Jorden, P. R., van Breda, I. G., Rudd, P. J., & Jorgensen, H. E. 1985, MNRAS, 217, 87

Stevens, J. A. & Robson, E. I. 1994, MNRAS, 270, L75

Stockton, A., Ridgway, S. E., & Lilly, S. J. 1994, AJ, 108, 414

Tammann, G. A. & Sandage, A. 1968, ApJ, 151, 825

Telesco, C. M., Joy, M., Dietz, K., Decher, R., & Campins, H. 1991, ApJ, 369, 135

Thuma, G., Neininger, N., Klein, U., & Wielebinski, R. 2000, A&A, 358, 65

Tingay, S. J., Jauncey, D. L., Reynolds, J. E., Tzioumis, A. K., King, E. A., Preston, R. A., Jones, D. L., Murphy, D. W., Meier, D. L., van Ommen, T. D., McCulloch, P. M., Ellingsen, S. P., Costa, M. E., Edwards, P. G., Lovell, J. E. J., Nicolson, G. D., Quick, J. F. H., Kemball, A. J., Migenes, V., Harbison, P., Jones, P. A., White, G. L., Gough, R. G., Ferris, R. H., Sinclair, M. W., & Clay, R. W. 1998, AJ, 115, 960

Tubbs, A. D. 1980, ApJ, 241, 969

Unger, S. J., Clegg, P. E., Stacey, G. J., Cox, P., Fischer, J., Greenhouse, M., Lord, S. D., Luhman, M. L., Satyapal, S., Smith, H. A., Spinoglio, L., & Wolfire, M. 2000, A&A, 355, 885

van Gorkom, J. H., van der Hulst, J. M., Haschick, A. D., & Tubbs, A. D. 1990, AJ, 99, 1781

Walter, F., Weiss, A., & Scoville, N. 2001, in American Astronomical Society Meeting, Vol. 199, 4904

Ward, M. J., Blanco, P. R., Wilson, A. S., & Nishida, M. 1991, ApJ, 382, 115

Watson, M. G., Stanger, V., & Griffiths, R. E. 1984, ApJ, 286, 144

Wills, K. A., Redman, M. P., Muxlow, T. W. B., & Pedlar, A. 1999, MNRAS, 309, 395

Worthey, G. 1994, ApJS, 95, 107

Wright, E. L. 1976, ApJ, 210, 250

Wright, M. & Birkinshaw, M. 1984, ApJ, 281, 135

Wrobel, J. M. 1991, AJ, 101, 127